

A METHOD TO PREDICT PILE RESPONSE UNDER VEHICULAR LOADING
FOR INTEGRAL ABUTMENT BRIDGES

by

Mike Arsenault

Submitted in partial fulfilment of the requirements
for the degree of Master of Applied Science

at

Dalhousie University
Halifax, Nova Scotia
January 2017

© Copyright by Mike Arsenault, 2017

Table of Contents

List of Tables.....	vii
List of Figures.....	viii
Abstract.....	x
List of Abbreviations and Symbols Used	xi
Acknowledgements	xv
Chapter 1 - Introduction	1
Chapter 2 - Literature Review	4
2.1 Mechanics of an IAB.....	4
2.1.1 Mass	4
2.1.2 Stiffness	5
2.1.3 Damping.....	5
2.2 Evolution of IAB Construction and Design.....	7
2.2.1 IAB Construction Evolution.....	7
2.2.2 IAB Design Evolution.....	10
2.2.2.1 Winkler Methodology.....	10
2.2.2.2 P-Y Method	12
2.2.2.3 Elasticity Theory.....	14
2.2.2.4 Finite Element Analysis	22
2.3 Current Canadian Practices	23

2.3.1	FEM-Winkler Method.....	23
2.3.2	Canadian Highway Bridge Design Code	24
2.3.3	IAB Design Considerations	26
2.4	Recent Studies and Ongoing Research	27
2.5	Scoudouc Bridge	34
2.5.1	General Arrangement.....	34
2.5.2	Site Geology.....	37
2.5.3	Design Approach.....	38
2.5.4	Construction.....	39
Chapter 3	- Field Tests	41
3.1	Preliminary Pile Tests	41
3.2	Scoudouc Bridge Pile Push Tests.....	43
3.2.1	Test Setup	43
3.2.2	Test Results	47
3.3	Scoudouc Bridge Live Load Test	54
3.3.1	Test Setup	54
3.3.2	Test Results	58
Chapter 4	- Soil - Structure Interaction Models	62
4.1	Elastic Continuum Methods	62

4.1.1	Broms Static Equilibrium Solution	62
4.1.2	Hetyenyi Differential Equation	62
4.1.3	Poulos and Hull Linear Elastic Solution	63
4.2	Equivalent Cantilever Methods	64
4.2.1	Abendroth and Greimann Equivalent Cantilever Solution	64
4.2.2	2D Pile Modelled as Equivalent Cantilever	65
4.2.3	2D Bridge Modelled with Equivalent Cantilever Piles	66
4.3	Soil Spring Methods	71
4.3.1	2D Pile Modelled with Discrete Linear Soil Springs	71
4.3.2	2D Bridge Modelled with Discrete Linear Soil Springs	74
4.3.3	3D Bridge Modelled with Discrete Linear Soil Springs	77
Chapter 5 - Comparison of Results from Linear-Elastic Methods ..		82
5.1	Single Pile Analyses	82
5.2	Bridge Analyses.....	88
Chapter 6 - Refinement of Solutions and Models Due to Soil Non-		
Linearity.....		91
6.1	Poulos and Davis Soil Non-Linearity Factors	91
6.2	Non-Linear Composite Backfill Springs	94

6.2.1	Carvajal’s Method	95
6.2.2	Terzaghi’s Method #1	98
6.2.3	Terzaghi’s Method #2	98
6.2.4	Comparison of Means to Find Effective Backfill Stiffness	99
6.3	Inference of Non-Linear Soil-Pile Spring Stiffness	105
6.3.1	Creation of Single Pile Linear FEM-Winkler Models	105
6.3.2	Establishment of P-Y Curves for Pile P5N.....	107
6.3.3	Definition of Non-Linear Soil Springs	107
6.4	Calibration of Bridge Model with Non-Linear Soil Springs	111
Chapter 7 - Discussion	116
7.1	Conceptual IAB Design.....	116
7.2	Lateral Pile Load Test.....	118
7.3	Development of P-Y Curves.....	121
Chapter 8 – Conclusions and Recommendations	124
8.1	Conclusions.....	124
8.2	Recommendations.....	127
References	129

APPENDIX A - SCOUDOUK BRIDGE BOREHOLE LOGS.....	133
APPENDIX B - PARTIAL DIFFERENTIATION SOLUTIONS FOR BEAM ON ELASTIC SUBGRADE	137
APPENDIX C - PICADILLY PILE TEST DATA.....	145
APPENDIX D - SCOUDOUK PILE TEST DATA	152
APPENDIX E - SCOUDOUK BRIDGE LIVE LOAD TEST DATA.....	154
APPENDIX F - BROMS COMPUTATIONAL SOLUTION	156
APPENDIX G - POULOS AND HULL COMPUTATIONAL SOLUTION	159
APPENDIX H - ABENDROTH AND GREIMANN CANTILEVER SOLUTION ..	165
APPENDIX I - DEVELOPMENT OF NON-LINEAR SOIL SPRINGS.....	170
APPENDIX J - STRAIN GAUGE CALIBRATION SHEETS.....	182

List of Tables

Table 3.1	Results of Scoudouc Lateral Load Tests.....	52
Table 4.1	Variation of Soil Stiffness for Pile P5N at a Head Deflection of 54mm.....	73
Table 5.1	Summary of Results from Individual Pile Elastic Solutions and Models.....	82
Table 5.2	Comparison of Pile and Deck Response for the Linear Bridge Analyses....	88
Table 6.1	Compression Foam Specifications.....	94
Table 6.2	Values of C for Different Abutment Types of IABs	97
Table 6.3	Upper Non-Linear Backfill Soil Spring Definition – North Abutment.....	101
Table 6.4	Middle Non-Linear Backfill Soil Spring Definition – North Abutment.....	101
Table 6.5	Lower Non-Linear Backfill Soil Spring Definition – North Abutment.....	102
Table 6.6	Upper Non-Linear Backfill Soil Spring Definition – South Abutment.....	103
Table 6.7	Middle Non-Linear Backfill Soil Spring Definition – South Abutment.....	103
Table 6.8	Lower Non-Linear Backfill Soil Spring Definition – South Abutment.....	104
Table 6.9	Soil Stiffness Variation for FEM-Winkler Single Pile Models.....	105
Table 6.10	Response of P5N During Lateral Load Test and Single Pile Linear Modelling.....	106
Table 6.11	Variation of Stiffness with Deflection for Spring at Node 27.....	109
Table 6.12	Comparison of Single Pile Responses.....	110
Table 6.13	Summary of Results from Bridge Models with Linear and Non-Linear Soil Springs.....	114

List of Figures

Figure 2.1	Beam on Inelastic Springs and Typical P-Y Curves for Cohesionless Soil...	13
Figure 2.2	Diagram of $k_h(x)$ and Effective Modulus of Horizontal Subgrade Reaction.	20
Figure 2.3	Equivalent Cantilever Lengths for Free-Head Piles in a Uniform Soil	22
Figure 2.4	Partial Elevation of Scoudouc Bridge	35
Figure 2.5	Cross-Section of Scoudouc Bridge	36
Figure 2.6	Abutment Configuration of the Scoudouc Bridge	37
Figure 3.1	Response to Static Push Test of Pile T-3024 in the West Direction	42
Figure 3.2	Response to Static Push Test of Pile T-3024 in the East Direction.....	42
Figure 3.3	Location of piles P5N and P10N.....	44
Figure 3.4	Photo of Test Configuration for Static Push Test of Pile P5N.....	45
Figure 3.5	Plan View of Test Configuration for Static Push Test of Pile P5N.....	46
Figure 3.6	Elevation View of Test Configuration for Static Push Test of Pile P5N	46
Figure 3.7	Response to Static Push Test of Pile P5N.....	47
Figure 3.8	Response to Static Push Test of Pile P10N.....	48
Figure 3.9	Crack Forming Along the Perimeter of Steel Sleeve of Pile P10N.....	49
Figure 3.10	Response to Static Push Test of Pile P5S.....	50
Figure 3.11	Response to Static Push Test of Pile P10S	51
Figure 3.12	Schematic of Idealized Live Load Test Vehicle.....	55
Figure 3.13	Photo of Scoudouc Live Load Test Configuration	55
Figure 3.14	Data Logger Indicating Strains on Pile P5N	57
Figure 3.15	Strain Gauges and Wireless Thermometer Installed on Pile P5N.....	57
Figure 3.16	Truck Position and Direction at Maximum Deck Deflection.....	59
Figure 3.17	Measured Deck Deflections due to Truck Load.....	60
Figure 4.1	Variation of k_h Along Pile P5N	64
Figure 4.2	2D Pile Modelled as Equivalent Cantilever.....	66
Figure 4.3	Idealized STAAD 2D Frame Bridge Model (Single Girder).....	68
Figure 4.4	Truck Position and Direction for Maximum Pile Axial Force.....	69
Figure 4.5	Truck Position and Direction for Maximum Pile Bending Moment.....	70
Figure 4.6	Results for 2D Pile Modelled with Discrete Linear Soil Springs.....	73
Figure 4.7	2D Frame with Linear Soil Springs.....	76
Figure 4.8	3D Bridge Modelled with Discrete Linear Soil Springs.....	79
Figure 4.9	Modelled Deck Maximum Deflection Curve.....	80
Figure 4.10	Maximum Modelled Live Load Stress in Pile P5N (MPa).....	81
Figure 5.1	Comparison of Modelled and Field-Measured Head Deflections.....	87
Figure 5.2	Measured and Modelled Bridge Deck Deflection due to Vehicular Loading	90
Figure 6.1	Yield-Displacement factor, F_{ρ} , for Free Head Pile in Soil with Uniform E_s .	93
Figure 6.2	Yield-Rotation factor, F_{ϕ} , for Free Head Pile in Soil with Uniform E_s	93

Figure 6.3	Positioning of North Abutment Backfill Springs (South Abutment Similar)	95
Figure 6.4	Comparison of Carvajal and Modified Terzaghi Backfill Spring Constants	100
Figure 6.5	Upper Non-Linear Backfill Soil Spring Definition – North Abutment	101
Figure 6.6	Middle Non-Linear Backfill Soil Spring Definition – North Abutment	102
Figure 6.7	Lower Non-Linear Backfill Soil Spring Definition – North Abutment	102
Figure 6.8	Upper Non-Linear Backfill Soil Spring Definition – South Abutment	103
Figure 6.9	Middle Non-Linear Backfill Soil Spring Definition – South Abutment	104
Figure 6.10	Lower Non-Linear Backfill Soil Spring Definition – South Abutment	104
Figure 6.11	P-Y Curve for Top Spring at Node 27	108
Figure 6.12	Graphic Representation of Non-Linear Soil Spring for Node 27	109
Figure 6.13	3D Bridge Model with Non-Linear Soil Springs	113
Figure 6.14	Maximum Modelled Live Load Stress in Pile P5N (MPa)	113
Figure 7.1	Production Pile Lateral Load Test Set-Up	120

Abstract

The objective of this work is to develop a design method for Integral Abutment Bridges (IABs), such that more accurate predictions of pile response to vehicular loading can be made. This paper presents the results of field tests performed on piles which support an IAB. These results led to a recommended IAB design procedure which includes an in-situ lateral pile load test, the development of P-Y curves, and the establishment of non-linear soil spring constants for modelling IABs.

A brief look at the soil-structure interaction (SSI) and mechanics of IABs, as well as a literature review of the evolution of the IAB design process, are included. Early works including the Winkler and elastic continuum theories lead to the establishment of solutions, which provide displacement and stress values used for design purposes. However, the advent of the home computer made Finite Element Modelling (FEM) a more viable and accurate approach to solving “beam on elastic subgrade” problems. A hybrid approach, combining FEM and Winkler theories (FEM-Winkler), has since become standard practice for designers of IABs throughout Canada. An example of such is presented herein.

The coefficient of horizontal subgrade reaction, k_h , from which are derived the stiffnesses of discrete soil springs used in the hybrid FEM-Winkler design process, is a variable that is difficult to estimate. Therefore, some structural and geotechnical engineers recommend conducting tests to better assess the actual lateral soil spring stiffnesses. Many of these tests, including those described in the American Society for Testing and Materials (ASTM) Standard D3966, are designed to be conducted on expensive mock-up pile assemblies with similar characteristics to those planned for the production piles. An alternate and more economical approach, consisting of an in-situ lateral pile test conducted on a production pile, was conducted. A live load test to measure bridge deck deflection and pile strain was also performed, and both tests are presented herein.

Based on the results of the in-situ lateral pile test, structural models were created with the structural software STAAD.Pro, and assumed values of linear lateral soil spring stiffnesses were used to match the pile head deflection and strain measured in the field. Initial estimates of spring stiffness were based on values of the variation of modulus of horizontal subgrade reaction (n_h) that were recommended in the Canadian Highway Bridge Design Code (CHBDC) CAN CSA S6-14, and the Canadian Foundation Engineering Manual (CFEM, 1992) for each of three (3) soil strata. These soil spring stiffnesses were found to be accurate at high soil strain, but much too flexible at low strain, which indicated soil non-linearity. Therefore, non-linear reaction-deflection (P-Y) curves were developed from the linear soil spring models, by noting the soil reaction at each discrete soil spring location, based on modelled soil/pile deflection. Non-linear soil springs were defined from the tangential stiffness of the P-Y curves, and these were used to refine a three-dimensional FEM-Winkler bridge model. A comparison of the model incorporating non-linear soil springs with the model incorporating linear soil springs demonstrated that each had a similar response to vehicular loading. Further to this, the predicted pile stresses and deck deflections from both bridge models agreed with values measured during the vehicular live-load bridge test.

List of Abbreviations and Symbols Used

2D	Two Dimensional
3D	Three Dimensional
AASHTO	American Association of State Highway and Transportation Officials
ASTM	American Society for Testing and Materials
C	Constant to calculate K_{abut}
CHBDC	Canadian Highway Bridge Design Code
CPT	Cone Penetration Test
CSP	Corrugated Steel Pipe
c_u	Undrained Shear Strength of Soil
d	Pile Diameter (Poulos and Hull, 1989)
D	Pile Diameter (Hetenyi, 1946)
D_1	Constant to Calculate the First Order Elastic End Moment
e	Length of Unsupported Pile (distance from pile head to groundline)
E	Modulus of Elasticity of Pile (Abendroth and Greimann, 1987)
E_{50}	Soil Modulus of Elasticity at 50% Stress Level
E_p	Modulus of Elasticity of Pile (Poulos and Hull, 1989)
E_s	Secant Modulus of Elasticity of Soil (Poulos and Hull, 1989)
E_{se}	Effective Secant Modulus of Elasticity of Soil
E_{smax}	Maximum Secant Modulus of Elasticity of Soil
FEM	Finite Element Modelling
FEM-Winkler	Finite Element Modelling-Winkler
f_y	Pile Yield Stress
F_ϕ	Rotation Yield factor
F_ρ	Deflection Yield Factor
G_{mob}	Mobilized Shear Modulus
H	Applied lateral Head Load
HP	H-Pile
H_u	Ultimate Pile Head Load
I	Moment of Inertia of Pile (Abendroth and Greimann, 1987)
IAB	Integral Abutment Bridge
I_p	Moment of Inertia of Pile
I	Moment of Inertia of Pile
I_k	Second Moment of $k_h(x)$ Curve
K	Factor to Calculate Pile Head Moment (Poulos and Hull, 1989)

k	Spring Constant
k	Linear Variation of E_s with Depth (Reese et al., 1974)
k_1	Constant for Spring#1
k_2	Constant for Spring#2
K_{abut}	Equivalent Abutment Spring Constant
K_e	Effective Factor to Calculate Pile Head Moment (Poulos and Hull, 1989)
k_e	Effective Horizontal Modulus of Subgrade Reaction (Abendroth and Greimann, 1987)
k_E	Effective Horizontal Modulus of Subgrade Reaction (Duncan et al., 1980)
k_{eq}	Equivalent Spring Constant
k_h	Modulus of Horizontal Subgrade Reaction
k_{he}	Effective Modulus of Horizontal Subgrade Reaction
k_{hmax}	Maximum Modulus of Horizontal Subgrade Reaction
kN	Kilonewton
K_p	Rankine Passive Earth Pressure Coefficient
kPa	Kilopascal
K_R	Variable Relating Pile Stiffness to Soil Stiffness
L	Length of Beam
L	Length of Embedded Pile (Poulos and Hull, 1989)
L_c	Critical Length of Pile
l_e	Equivalent Cantilever Length of Pile to Groundline (Abendroth and Greimann, 1987)
L_e	Effective Pile Length
L_e	Equivalent Cantilever Length of Pile
$l_{eM_{pinned}}$	Embedded pile length for pinned head moment
$l_{eM_{fixed}}$	Embedded pile length for fixed head moment
$l_{eV_{fixed}}$	Embedded pile length for fixed head shear
$l_{eV_{pinned}}$	Embedded pile length for pinned head shear
$L_{M_{fixed}}$	Pile length for fixed head moment
$L_{M_{pinned}}$	Pile length for pinned head moment
L_o	Length of Pile in Bending
L_u	Unsupported Length of Pile
l_u	Unsupported Length of Pile
$L_{V_{fixed}}$	Pile length for fixed head shear
$L_{V_{pinned}}$	Pile length for pinned head shear

M	First-Order Elastic End Moment (Abendroth and Greimann, 1987)
M	Applied head moment (Poulos and Hull, 1989)
MI	Second moment of inertia of $k_h(x)$ about L_o
M_{elas}	Maximum elastic pile moment
M_{fixed}	Maximum fixed head pile moment
M_{pinned}	Maximum pinned head pile moment
M_{plas}	Maximum plastic pile moment
M_y	Pile Yield Moment
m	Linear Variation of E_s with Depth (Poulos and Hull, 1989)
m_e	Effective Linear Variation of E_s with Depth
NBDTI	New Brunswick Department of Transportation and Infrastructure
n_h	Linear Variation of E_s with Depth (Terzaghi, 1955)
n_{hi}	Linear Variation of E_s with Depth for Soil Layer i
P	Lateral Soil Reaction Force per Unit Length of Pile (P-Y curve)
P	Lateral Pile Head Load
PDA	Pile Driving Analyzer
P_u	Ultimate Lateral Soil Pressure
Q	Axial Load on Pile
R^2	Coefficient of Determination
S	Pile Section Modulus
SSB	Simply Supported Bridge
SSI	Soil Structure Interaction
V_{fixed}	Maximum fixed head pile shear
V_{pinned}	Maximum pinned head pile shear
w	Width of Abutment Wall
X	Depth Along Length of Pile
x_1	Depth Below Abutment
Y	Lateral Deflection of Pile
Δ	Pile Displacement at Point of Lateral Load Application
Δ_{elas}	Elastic Deflection Difference from Ground to Pile Head
Δ_{plas}	Plastic Deflection Difference from Ground to Pile Head
γ	Unit weight of soil
ν	Poisson's Ratio
σ'_v	Effective Vertical Soil Stress
ϕ'	Effective Soil Angle of Friction
$\rho_{elas\ ground}$	Elastic Pile deflection at groundline

$\rho_{\text{elas head}}$	Elastic pile deflection at head
$\rho_{\text{plas ground}}$	Plastic pile deflection at ground
$\rho_{\text{plas head}}$	Plastic pile deflection at head
ϕ_{elas}	Elastic Pile rotation at groundline
ϕ_{plas}	Plastic Pile rotation at groundline

Acknowledgements

I wish to extend gratitude to my family, notably my wife Lynn, mother Paulette and “mémère” Marguerite, for having patience with me during my extended study period and providing the support required to accomplish this personal goal.

The support that I received from my stepson Josh, who helped with some of the illustrations and transcribing of formulas, is greatly appreciated. To my dear stepdaughter Shelby, I say thank-you for allowing me to commandeer the kitchen table during the many evenings and late nights needed to finish my work.

I want to thank Jessica Fredericks, Alex Smith and cousin Marc Landry for their assistance in the field, and the New Brunswick Department of Transportation and Infrastructure (NB DTI) for subsidizing the testing of the Scoudouc bridge.

The assistance that I received from my colleagues Monica Jaillet and Tom Clark, for formatting and CAD work respectively, is highly valued.

I wish to thank all of my colleagues on the Safe Clean Drinking Water Project for having patience with me during the writing of my thesis. A special thank-you goes to Chris Connolly and Jianmin Zhang, who left their families behind and assumed my responsibilities during my periods of absence, thus allowing me to complete this personal task.

Finally, my thesis committee, comprised of Dr. Jane Thorburn, Dr. Hany El Nagggar and Dr. Robert Bauer, provided much insight and guidance during the writing of this thesis. Their contribution is greatly appreciated.

Chapter 1 - Introduction

The objective of this work is to gain a better understanding of IAB pile behaviour, and to develop a standard procedure for design. A method was established to conduct a simple in-situ field test to measure the stiffness of the soil-pile system of a production pile in a IAB abutment. The author illustrates how this information can be used to develop P-Y curves and define non-linear soil springs to be used in a hybrid Finite Element Modelling and Winkler (FEM-Winkler) process to observe pile stresses under different vehicular loading conditions.

Soil-Structure Interaction (SSI) is a key consideration for the design of an IABs, and is often inaccurately represented due to the inherent variability of soil conditions and behaviour. It is for this reason that more and more bridge design engineers are recommending that lateral pile load tests be performed to better assess how the pile/soil system will behave. IABs engage the surrounding soil through abutment displacements caused primarily by thermal expansion/contraction, vehicular loading, wind loading and inertial forces caused by seismic activity. Rotational and translational rigidity at the interface of the girders and abutment diaphragm, as well as at the interface of the abutment diaphragm and pile heads, cause the structure to act as a frame. The soil surrounding the piles and abutment diaphragm provide vertical and lateral support to minimize displacements and offer structural stability, while also providing the flexibility necessary to allow movements to occur. The stiffness of the soil surrounding the structure, which is often represented by the modulus of horizontal subgrade reaction (k_h), is a key variable in predicting the behavior of the IABs.

Chapter 2, Literature Review, includes an overview of the mechanics and behaviour of IABs, and how the design process has evolved from early spring theory to full three-dimensional (3D) FEM occasionally used today. This chapter also talks about the general Scoudouc Bridge configuration, including site geology which led to a unique “manufactured” abutment design to achieve pile fixity. Chapter 3, Field Tests, describes the various tests that were performed, including the individual static pile load tests, as well as the bridge live load tests. This chapter details the methodology and apparatus used during testing, as well as summarizes the results. Chapter 4, Soil-Structure Interaction Models, shows the various models which are typically used for design purposes, and how each incorporates the value of k_h . These include the computational models of Broms (1964a), Poulos and Hull (1989) and Abendroth and Greimann (1987), as well as two-dimensional (2D) and 3D structural software models. In order of complexity, the structural software models are i) 2D Equivalent Cantilever of Single Pile, ii) 2D Equivalent Cantilever of IAB, iii) FEM-Winkler of Single Pile, iv) 2D FEM-Winkler of IAB, and v) 3D FEM-Winkler of IAB. Chapter 5, Comparison of Results from Linear-Elastic Methods, describes the preliminary pile lateral load tests that were conducted at the Picadilly Mine, as well as the pile lateral load tests that were conducted at the Scoudouc Bridge site. A live load test was also performed on the Scoudouc Bridge. In Chapter 6, Refinement of Solutions and Models Due to Soil Non-Linearity, factors are applied to the Poulos and Hull solution to account for the non-linear behaviour of soil, non-linear soil spring stiffnesses are calculated to represent the coupled effect of the backfill soil and the compression foam, and non-linear soil-pile springs are developed. The 3D bridge model is calibrated with the non-linear soil springs. In Chapter 7,

Discussion, the author discusses a method of field-measuring the soil-pile stiffness, and defining the non-linear soil spring stiffness for use in the FEM-Winkler modelling of an IAB. Chapter 8 contains the Conclusions and the Recommendations.

Chapter 2 - Literature Review

2.1 Mechanics of an IAB

Integral Abutment Bridges have a fixed connection with their foundation piles, as opposed to simply supported bridges (SSBs), which are typically only restrained against vertical and lateral translation. IABs rely on the flexibility of the soil/pile system to allow translation and rotation of the abutments due to thermal, wind, seismic and vehicular loads, while at the same time depending on the soil-pile system stiffness for vertical and lateral support. IABs differ from SSBs in behaviour due to the engagement of abutment elements, thus changing the overall structural mass, stiffness and damping.

2.1.1 Mass

The mass which contributes to the behaviour of IABs comes from the bridge superstructure, substructure and surrounding soil. The superstructure typically consists of an asphalt overlay, concrete deck, concrete parapets, concrete or steel girders, and concrete or steel intermediate diaphragms. The substructure typically consists of a concrete end diaphragm, concrete wingwalls, and steel piles. The soil mass which participates in the function of IABs cannot be determined with a high degree of accuracy because the soil influence field is not well known. Logic would suggest that greater structural movements would mobilize a greater soil field, with all other things equal. By the same thought process, one can easily understand that a firmer soil would engage a larger soil field than would a soft soil, as the greater shear strength would transfer elemental displacements.

2.1.2 Stiffness

The sum of the individual stiffness constants of the superstructure and substructure is far less than the complete system. This is because the frame provides both rotational and translational restraint at the superstructure/diaphragm interface, and at the diaphragm/pile interface. Structural continuity is provided by embedding the superstructure and piles deep enough into a large and rigid abutment diaphragm to ensure moment transfer from each element. A very small angle of rotation occurs within the diaphragm, as often evidenced by the diagonal cracking from the girders' bottom flanges, but it is common design practice to assume complete rotational rigidity. The soil contributes to the overall bridge stiffness by applying a compressive force to those components exposed to soil. This force is a function of the coefficient of horizontal subgrade reaction (k_h), which is defined as the pressure required to move the soil one unit measurement of distance. It is often assumed that the horizontal subgrade reaction increases linearly with depth in cohesionless soils, and is constant with depth in cohesive soils. The gradient at which it varies in cohesionless soils is a function of the effective density of the soil. The coefficient of horizontal subgrade reaction is directly proportional to the undrained shear strength in cohesive soils.

2.1.3 Damping

The overall bridge system damping is a combination of damping attributes from the various components and materials that make-up the bridge, and how they interact with one another. The materials that comprise the Scoudouc bridge are steel, concrete and soil.

Steel has a relatively well defined material damping coefficient, and the limited number of steel connections in the bridge means that slip damping is negligible. So, the damping caused by the steel component of the bridge can be estimated with fair accuracy.

Concrete damping is more complex than steel damping because of the spatial and time variation of concrete attributes such as modulus of elasticity, section modulus and creep.

Cracking of concrete due to tensile stresses exceeding the modulus of rupture leads to increased damping through interfacial friction. Soil damping is much more complicated and difficult to determine analytically because it depends on the initial state of the soil medium, and the extent to which the soil field is engaged.

The materials making-up the superstructure and substructure bridge components have characteristics that are very well known; thus, it is easy for one to predict their behaviour when acting independently of the surrounding soil. However, this is not the case with IABs. These rely on the interaction of the soil and sub-structure; therefore, their predictability is only as good as the least known component, namely the soil. The behaviour of soil is not easily predicted because of the many variables that affect its performance.

Since the behaviour of IABs depends so heavily on the interaction of the soil and structure, it is important to accurately estimate the soil-structure system's parameters as accurately as possible when designing IABs.

2.2 Evolution of IAB Construction and Design

2.2.1 IAB Construction Evolution

Integral Abutment Bridges had been constructed for decades by builders who did not fully understand the basic mechanics of these structures, and hence made conservative assumptions to ensure the structure remained safe throughout its operational life. The idea that girder and abutment rotation caused by vehicular loading transferred a bending moment to the supporting piles due to a fixed connection was not part of the design process. They constructed this configuration of bridge because it was a simple and cost effective concept to simply connect the beams to the abutments, and with short-span bridges, this configuration saw much success. Failures due to overstressed beams were rare because of the modest thermal expansion and contraction, and the idea of having to provide rotational and translational freedom at each abutment was not part of the thought process.

By the early 1900's, as bridge spans were extended, beam and abutment failure due to overstressing became more frequent and attention was paid to detailing bearings and expansion joints that allowed the bridge to move "freely" with thermal expansion and contraction. This remained a common design feature for medium span bridges, until the 1980's when structural and geotechnical engineers began investigating configurations that permitted the construction of longer IABs. The increased popularity of personal computers and development of structural analysis tools, including Finite Element Analysis, allowed the designers to better simulate IAB behaviour and gain a more accurate understanding of soil/structure interaction. Within the transportation industry, there was a growing concern and realization that the long-term maintenance costs

associated with expansion joints were adding significantly to operating budgets. Jointless bridges such as IABs rapidly became attractive alternatives to simply supported bridges, and engineers began studying these more intently.

Bridge design engineers, owners, builders and operators continue to favour the design and construction of IABs because of the lower capital construction costs and long-term maintenance costs. In addition to these cost savings, benefits of IABs include longer spans for bridges with pedestrian sidewalks, less susceptibility to catastrophic damage due to high-level dynamic excitation, smoother approach transitions, and higher aesthetic value.

The increased popularity of IABs resulted in the development of standards for lateral load tests, such as The American Society for Testing and Materials standard D3966/D3966M-07 (2013) *Standard Test Methods for Deep Foundations Under Lateral Load*, to guide engineers in measuring the soil-structure characteristics that are required to design structures that rely on lateral pile behaviour. This standard provides a very detailed approach to test methods that are applied to simulated site conditions, to measure the lateral deflection and load of a vertical or inclined deep foundation when subjected to lateral loading. The methods apply to all deep foundations, regardless of their method of installation, and may be used for testing single piles or pile groups. Plans, specifications, provisions, or combinations thereof prepared by a qualified engineer may provide additional requirements and procedures as needed to satisfy the objectives of a particular test program. The standard covers eight test procedures, of which seven are optional. These are Standard Loading (mandatory when ASTM D3966 is specified), Excess Loading, Cyclic Loading, Surge Loading, Reverse Loading, Reciprocal Loading,

Specified Lateral Movement, and Combined Loading. The Standard Loading Test consists of the application and removal of a total lateral test load equal to 200% of the proposed lateral design load of the pile or pile group. The percentage load varies from 0 to 200% in increments of 25%, then the removal of load in increments of 50% at time intervals that vary between 10 and 60 minutes. The Excess Loading Test increases the loading of the Standard Test to 250% of the proposed lateral design load. The Cyclic Loading Test goes through four (4) incremental cycles of lateral load application and removal. The Surge Loading Test involves a cycle of application and removal up to 200%, followed by an additional, abrupt application of the full 200% of the proposed design load, then a removal cycle. The Reverse Loading Test involves the application of lateral test loads in either the push mode followed by pull, or vice versa. The Reciprocal Loading Test involves the application and removal of each specified lateral load level first in one direction, and then in the opposite direction for the number of specified cycles. Lastly, the Specified Lateral Movement Test entails applying the lateral test loads in accordance with the Standard, Excess, Cyclic and Surge Load Tests until the gross lateral movement of the test pile or group is as specified, and then remove the test load in four equal decrements, allowing 10 minutes between decrements.

Test preparation for each of these tests involves creating an independent test configuration with similar conditions to those that production piles will be exposed to, providing a clear distance of 5 pile diameters or a minimum of 2.5m between the test pile(s) and reaction piles to ensure reaction loads do not affect the results. The standard lists many ways of providing the necessary reaction for jacking of the test pile head in

free and fixed conditions, including battered reaction piles, plumb reaction piles with embedded cap, timber deadman, and massive weights.

Only once the soil-pile system parameters are determined, or estimated, can the detailed design of the IAB begin. The most common approaches to IAB design today are the Winkler Methodology, Elastic Theory, the P-Y Method, and Finite Element Analysis.

2.2.2 IAB Design Evolution

2.2.2.1 *Winkler Methodology*

In 1867, Winkler developed a model for a beam on elastic subgrade (Coduto, 2001). The model consisted of a series of closely-spaced springs which are independent from one another, and each having a spring constant value of k as a function solely of the displacement at that point. Vesic (1961) thought that one should not use independent springs as each location is influenced by the adjacent reaction caused by a load being applied to a continuous beam. However, he confirmed that this fact leads to negligible errors in most “beam-on-elastic-subgrade” problems.

The Winkler Method is the most traditional form of analysis for calculating pile head deflections and bending moments, and is still the most commonly used analytical tool for designers of IABs today. The general theory was used for predicting a single pile response, based on the work done by Hetenyi (1946) for an elastic beam supported on an elastic medium. It is represented by the following well known formula:

$$E_p I_p \frac{d^4 y}{dx^4} + Q \frac{d^2 y}{dx^2} + E_s y = 0 \quad (\text{Equation 2.1})$$

Where:

E_p =Modulus of Elasticity of Pile (N/mm^2)

I_p =Moment of Inertia of Pile (mm^4)

Q =Axial Load on Pile (N)

E_s =Secant Modulus of Elasticity of Soil= $-p/y=k_h D$ (N/mm^2)

y =Lateral Deflection of Pile (mm)

x =Depth Along Length of Pile (mm)

p =Lateral Soil Reaction Force per Unit Length of Pile (N/mm)

k_h =Modulus of Horizontal Subgrade Reaction (N/mm^3)

D =Pile Diameter (mm)

Winkler's work on soil elasticity theory was extended by Davisson and Robinson (1965), who established an idealized cantilever model representing the soil-pile system to a point of fixity (typically where lateral deflection is less than 5% of maximum deflection at ground line). This model could then be used by structural engineers to estimate the moment and shear in the pile. The disadvantage of this approach is that the pile is assumed to be unsupported above the point of fixity, which is not representative of the real system, and will provide inaccurate moment and shear distribution.

The limitations of the classic "beam-on-elastic-foundation" to represent only linear soil behaviour was also recognized by McClelland and Focht (1956), who used finite difference methods to solve the "elastic beam-on-inelastic-medium" using non-linear soil response. Later work by Reese et al. (1974) refined the construction of curves which represented the relationship of soil reaction and lateral displacement at discrete locations

along the length of an embedded pile for use in the design of laterally loaded piles. These curves are commonly known as P-Y curves, and this has become the P-Y method of predicting the response of embedded piles to lateral loading.

2.2.2.2 *P-Y Method*

The P-Y Method is a semi-empirical extension of the Winkler approach, where non-linear soil spring stiffnesses are back-calculated from in-situ lateral pile load tests. The soil reaction is measured at incremental locations along the embedded pile, and plotted against the deflection at that point. The result is a graph that displays a set of non-linear curves (see Figure 2.1), one for every depth of embedment. Though more reflective of general soil behaviour, the development of accurate, site-specific P-Y curves requires very involved and costly lateral pile load testing at the proposed structure location. As an alternative to this, engineers often use P-Y curves that have been established on other sites, but these must be used with caution as they may not reflect the actual site conditions. P-Y curves can also be generated by correlating CPT or pressure meter data, but these must also be used cautiously.

Figure 2.1 shows each curve associated with a soil spring, and having elastic linearity up to point “k”, where the curve becomes a parabolic up to point “m”, then resumes linearity at a lower stiffness up to point “u”, at which point the soil become perfectly plastic. The value of k in the figure is a parameter based on relative density, and is equivalent to n_h , which was introduced and defined earlier in this thesis.

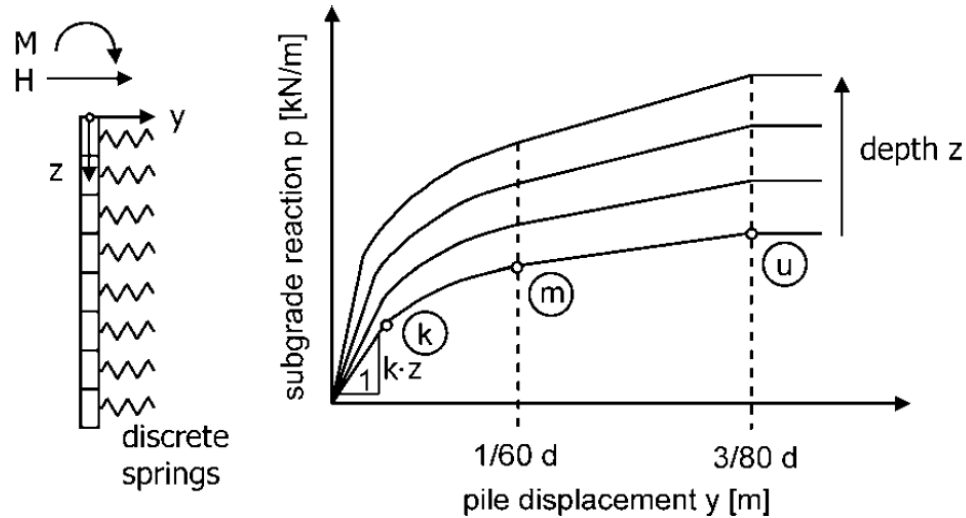


Figure 2.1 Beam on Inelastic Springs and Typical P-Y Curves for Cohesionless Soil.
(Reese et al., 1974)

The essence of the P-Y method is that the Hetenyi (1946) equation, shown in Equation 2.1, is solved using numerical techniques (finite difference), which is described in detail by Reese (1977). The P-Y curves describe the lateral pile movement obtained by applying a specified load increment, and represent the discrete behaviour of the soil at one depth. The underlying principle of this theory is an assumption that this behaviour is independent of soil behaviour at other depths. When studying the governing equation, one can see that the P-Y curve is necessary to describe displacements for a given lateral force and/or applied bending moment. However, the stress generated in the pile is also related to the structural properties of the pile and the loading conditions. Therefore, iteration is used to solve the governing equation by using finite difference techniques and defining boundary conditions. The non-linear shape of the P-Y curves allow for the characterization of non-linear soil behaviour in the upper portion of the pile in which

lateral deflections are much larger, and linear soil behaviour in the lower portion of the pile where displacements are smaller.

Both static and cyclic pile tests can be performed to develop P-Y curves. The measured soil resistance, and calculated soil modulus, will differ when comparing test results from clays and sands. Typically, one will observe a reduction in “apparent” soil resistance and stiffness for a limited maximum pile head deflection in cohesive soils because the greater soil plasticity creates a void between the pile and soil in the upper portion of the pile. The word “apparent” implies an observed reduction in soil stiffness, when in fact the soil itself becomes denser and stiffer during the first cycle, but then has less contact with the pile in future cycles. In cohesionless soils, the interfacial gap between the pile and soil on the trailing side is filled with collapsing aggregate, which is then compacted on the return cycle of the pile. This repetitive action results in denser and stiffer soil resisting the pile movement, providing the ultimate strength of the soil is not reached. When the ultimate strength of the soil is reached, the soil exhibits a marked reduction in stiffness at its yield point, and this represents the transition from elastic to inelastic soil behaviour.

2.2.2.3 Elasticity Theory

According to Timoshenko and Goodier (1951), “all structural materials possess to a certain extent the property of elasticity: if external forces, producing deformation of a structure, do not exceed a certain limit, the deformation disappears with the removal of the forces”. Because soils are known to behave linearly at low strain and non-linearly at higher levels of strain, one must be careful when applying elastic theory to problems of SSI, such as the design of IABs. Where approximate deflection and rotation predictions

are sufficient, such as during the conceptual design phase, linear theories may be adequate providing that the appropriate values of soil modulus of elasticity and modulus of horizontal subgrade reaction are used, and soil displacement is expected to be small.

Two classic papers from Broms (1964a, b) form the basis for most idealized models to predict the lateral load carrying capacity of piles. It is based on the static equilibrium of the pile and soil system, with the limiting factor being the ultimate soil strength. To simplify the analysis, Broms classified soils into one of two categories: cohesive or cohesionless.

In cohesive soils, he assumed no resistance from the soil surface to 1.5 times the diameter of the pile, then assigned an ultimate lateral soil pressure of $P_u=9c_u$ at any point along the embedded pile. The c_u variable represents the undrained shear strength of the soil.

Another assumption is that the pile movements will be large enough to mobilize this soil reaction.

In cohesionless soils, Broms determined that the ultimate lateral soil pressure is as follows:

$$P_u=3K_p\sigma'_v \quad (\text{Equation 2.2})$$

where the Rankine passive earth pressure coefficient is as follows:

$$K_p= \tan^2(45^\circ+\phi'/2) \quad (\text{Equation 2.3})$$

The σ'_v and ϕ' variables represent the effective vertical soil stress (kPa) and effective angle of friction (degrees), respectively.

The estimation of the lateral capacity of a single pile requires the designer to consider i) failure due to yielding of the soil along the entire length of the pile (short pile failure), and ii) failure due to yielding of the pile section at maximum moment (long pile failure).

Solutions based on elastic continuum and boundary element analysis, have been published by many, including Poulos and Davis (1980) and Poulos and Hull (1989) for soils with constant soil modulus with depth (cohesive soils) and linearly increasing with depth (cohesionless soils). Formulas for the ground line deflection, ground line rotation and maximum pile moment were provided for free and fixed head conditions, and for rigid (short) and flexible (long) piles. An equation for fixed head pile moment is also presented in their work.

The variable L_c is introduced in Poulos and Hull's work as representing the critical length of pile, which is used to verify whether a pile acts as a short or long pile. If the total length of pile, L , exceeds or equals the critical value L_c , then it is considered to be a long pile. If the length of the pile, L , is less than one third of L_c , then it is considered to be a short pile. If the length of the pile L falls between these two values, then it is considered to be a pile exhibiting characteristics of both types, and linear interpolation is required between solutions. The variable L_c is represented in the following formula, for a free head pile in cohesionless soil:

$$L_c = 1.81d(E_p/md)^{0.2} \quad (\text{Equation 2.4})$$

Where

$$m = \text{Linear Variation of } E_s \text{ with Depth (N/mm}^3\text{)}$$

d =Pile Diameter (mm)

E_p =Modulus of Elasticity of Pile (N/mm²)

E_s =Secant Modulus of Elasticity of Soil (N/mm²)

Variations of the L_c formula are presented in Poulos and Hull (1989) for different soil types. The biggest drawback to this method is the inability to represent non-linear soil springs. To provide more realistic values of pile moment, translation and rotation, Poulos and Davis (1980) and Budhir and Davies (1987,1988) present a convenient non-linear approach where yield factors are applied to the results of the linear elastic equations to account for soil yielding. These factors are primarily a function of the magnitude of applied load, the pile flexibility relative to that of the soil, and the distribution of soil stiffness.

Greimann et al. (1982) extended the Poulos and Hull, work and helped develop the American Association of State Highway and Transportation Officials' (AASHTO's) specification on beam column design, which involved idealizing the soil-pile system as a static equivalent cantilever. Abendroth and Greimann (1987) further advanced this work, and developed a procedure to address the following three AASHTO Specification design criteria: i) Capacity of the pile as a structural member, ii) Capacity of the pile to transfer the load to the ground, and iii) Capacity of the ground to support the load.

Abendroth and Greimann's procedure is a conventional elastic design approach, which neglects the reserve strength associated with plastic hinge formations; therefore, redistribution of internal forces is not permitted to occur for ultimate strength. This is a

conventional elastic design procedure which establishes idealized equivalent cantilevers that are used to calculate stresses developed in the pile.

Abendroth and Greimman introduce a variation of Poulos and Hull's critical length variable L_c , and it is defined as the depth below which displacements and bending moments at the pile head have little effect. Piles longer than L_c act as infinitely long piles. It is defined as follows for all soil types:

$$L_c = 4(EI/k_h)^{0.25} \quad \text{(Equation 2.4)}$$

Where

E =Modulus of Elasticity of Pile (N/mm^2)

I =Moment of Inertia of Pile (mm^4)

k_h =Modulus of Subgrade Reaction of Soil (N/mm^3)

The lateral displacement at the pile head induces a first-order elastic end moment M , represented by the following formula:

$$M = D_1 EI \Delta / L_e^2 \quad \text{(Equation 2.5)}$$

Where

D_1 =Variable to Account for Pile Head Boundary Condition

E =Modulus of Elasticity of Pile (N/mm^2)

I =Moment of Inertia of Pile (mm^4)

Δ =Pile Displacement at Point of Lateral Load Application (mm)

L_e =Equivalent Cantilever Length of Pile (mm)

The variable D_1 is equal to 3 or 6 for pinned or fixed head conditions, respectively. These values are consistent with common beam equations for cantilever beams with pinned or fixed head conditions, respectively.

A method of calculating an effective horizontal coefficient of subgrade reaction k_e for a pile which penetrates soil strata of varying stiffness is presented in Abendroth and Greimman's (1987) work, and is expressed as follows:

$$k_e = 3/L_o^3 \int_0^{L_o} \{k_h(x)(L_o - x_1)^2\} dx \quad (\text{Equation 2.6})$$

Where

L_o =Length of Pile in Bending= $L_c/2$ (mm)

x_1 =Depth Below Abutment (mm)

$k_h(x)$ =Modulus of Horizontal Subgrade Reaction at Depth x (N/mm³)

This integral expression is simply the result of equating the second moment of inertia of the areas of a $k_h(x)$ diagram and a k_e diagram taken about a line at depth L_o , and solving for k_e . This depth represents the active length of the pile in bending, and equals one quarter of the deflected wave shape including contra-flexure, or $L_c/2$. A simplified

example of Equation 2.6 is depicted in Figure 2.2, where the equations for I_k and I_{k_e} would be equated and solved for k_e . The values of k_1 and k_2 represent the modulus of horizontal subgrade reaction at the top and bottom of the soil horizon for which k_e is being calculated. The variable d represents the depth of the soil horizon, the variable a represents the distance from the depth at L_o to the bottom of the soil horizon, and the variable c represents the distance from the depth at L_o to the geometric centre of the area bound by d and k_e .

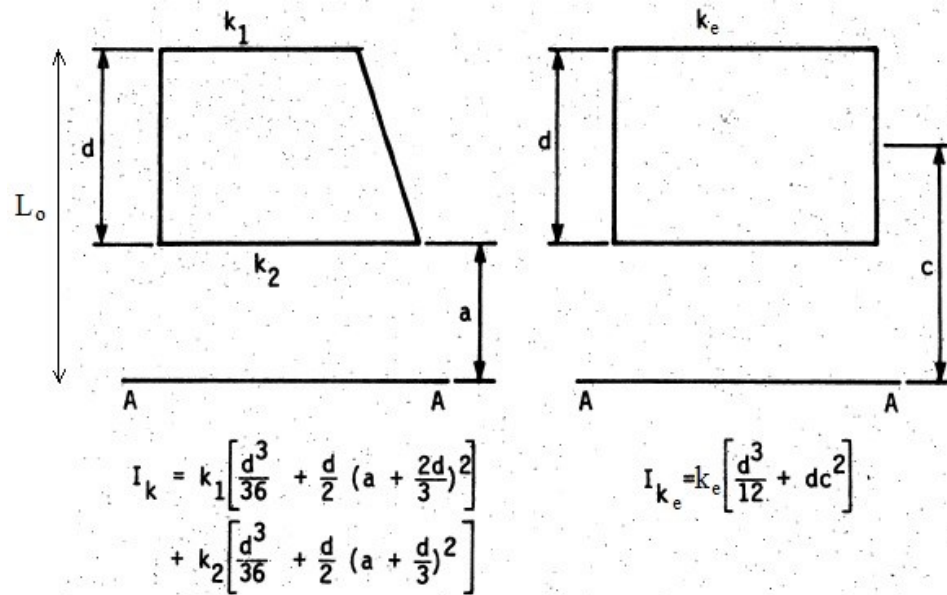


Figure 2.2 Diagram of $k_h(x)$ and Effective Modulus of Horizontal Subgrade Reaction. (Abendroth and Greimman, 1987)

An iterative procedure is need to solve for k_e , because L_o is a function of k_e . This procedure is outlined as follows:

Step 1: Assume an initial value for the equivalent-horizontal stiffness k_e of the layered soil.

Step 2: Evaluate the active length, L_o , of the pile in bending, which is assumed to be equal to one-quarter of the deflected-wave shape for the pile or about one-half of the length L_c , by applying the expression

$$L_o = 2(EI/k_h)^{0.25} \quad (\text{Equation 2.7})$$

Step 3: Calculate the second moment, I_k , of the $k_h(x)$ curve about a reference line at a depth of L_o .

Step 4: Calculate the second moment, I_{k_e} , of the k_e curve about a reference line at a depth of L_o .

Step 5: Equate I_k and I_{k_e} , and solve for k_e to obtain a new estimate for the equivalent, horizontal stiffness, k_e , of the soil.

Step 6: Return to Step 2 and repeat Steps 2, 3, and 4 until convergence is obtained for the stiffness k_e .

After the length L_c is established, Figure. 2.3 is used to find L_e for a pile behavior that is associated with the respective equivalent cantilever. If soils with varying modulus of elasticity are present, then the above-noted procedure must be followed to convert the horizontal subgrade modulus to an equivalent uniform value before using Figure 2.2 to find L_e . The variables in Figure 2.3 are defined as follows:

l_u =Unsupported Length of Pile, Above the Groundline (mm)

l_e =Effective Cantilever Length (mm)

l_c =Critical Pile Length (mm)

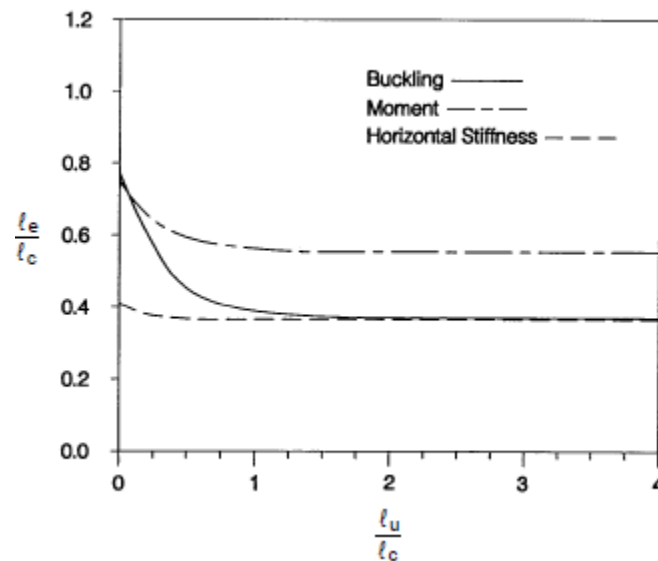


Figure 2.3 Equivalent Cantilever Lengths for Free-Head Piles in a Uniform Soil. (Abendroth and Greimann, 1987).

2.2.2.4 Finite Element Analysis

Structural analysis has historically taken the form of deriving differential equations which relate the variables through basic physical principles such as static equilibrium, conservation of energy, and Newton's laws of motion. However, once formulated, solving the resulting mathematical models manually is often impossible, especially when the resulting models are non-linear partial differential equations such as those describing soil/structure interaction. Finite Element Modelling is a discretization technique whose basic concept is the subdivision of the mathematical model into disjointed (non-

overlapping) components of simple geometry called finite elements. The response of each element is expressed in terms of a finite number of degrees of freedom characterized as the value of an unknown function at a set of nodal points. The response of the mathematical model is approximated by the response of the discrete model obtained by assembling all elements. Unlike finite difference models, finite elements do not overlap in space, but have continuity at their respective boundaries.

2.3 Current Canadian Practices

2.3.1 FEM-Winkler Method

Finite Element Modelling of IABs has gained popularity in the past decade; however, it is generally only fully utilized on large, complex bridge structures. For these configurations, such as long span, super-elevated, or heavily skewed bridges supported on stratified soil, three-dimensional FEM is required to accurately represent the behaviour and interaction of all components. The soil in this case is represented as a continuum of elements with boundary conditions that more accurately represent soil behaviour. This is a time consuming and expensive exercise that should be limited to the most challenging projects. As a simplified compromise, the superstructure and substructure are commonly modelled with beam and plate elements having well established and understood boundary conditions; but, the soil medium which encapsulates the structural abutment components is often represented as a series of discrete soil springs. So, the analysis is essentially a hybrid approach, combining the Finite Element and the Winkler methodologies. Further to this, it is common to represent the superstructure/diaphragm/pile frame in simple two

dimensional space, with each component being idealized to have the equivalent mass, stiffness and damping (when dynamic analysis is required) characteristics of the actual assembly. Simplified linear elastic cantilever models and formulae are still used in practice to validate detailed computer modelling, and to provide an estimate of pile behaviour during the conceptual design stage.

2.3.2 Canadian Highway Bridge Design Code

The CHBDC CAN CSA S6-14 (Revised in 2016) governs bridge design in Canada, and has some sections that have content pertaining specifically to the design of IABs:

Section 4.6.4 Soil-Foundation-Structure Interaction is contained in the Seismic Design section of the CHBDC; however, its Commentary contains useful information on how bridges should be modelled to simulate the structure's response to earthquake loading. The principles discussed and methods recommended lend themselves to the design and analysis of IABs. The main difference is that in a seismic event, the soil engages the bridge structure, while the bridge engages the soil when observing typical IAB performance due to thermal, vehicular or wind loading. A section within the commentary notes that analyses can be coupled, where the soil, foundation and structure are modelled together; or they can be uncoupled, where they incorporate a simplified soil-foundation-structure system such as a Winkler spring computational model, also known as compliance springs. It states that "compliance springs are dependent on the location-specific soil stratigraphy and properties, and hence vary along the bridge". An idealized

schematic of a soil-pile-structure model with discrete soil springs is presented, and values of backfill stiffness for various abutment types are recommended.

Section 5.5.7 Rigid Frame and Integral Abutment Types is contained in the Structural Analysis section of the CHBDC. The Commentary for this section emphasizes the importance of considering the effects of structural continuity and stresses induced in the various components due to frame action. It also warns that the analysis must consider the phases of construction, as load conditions and resisting mechanisms will differ from those of a completed IAB. Also contained in the Commentary is the fact that girders are typically designed to resist full positive moment as if they were simply supported, even if the magnitude of maximum positive moment will be less considering moment transfer at the abutments.

Section 6.17 Integral and Semi-Integral Abutments is contained in the Geotechnical section of the CHBDC, and provides guidance on the design of IAB abutments. It states that “the structural analysis of each pile should be carried out using a plausible methodology such as i) Equivalent Cantilever Method – where the pile is considered to act as a column with a fixed base at some distance below the ground surface, and with some degree of fixity occurring at the junction between the pile/abutment connection; or ii) Frame/Spring Analysis – application of a structural frame analysis program that takes into account the soil-pile interaction by modelling with a series of springs placed along the length of the piles.” This section also discusses the need for the top of the pile to be encased in a soft medium to promote flexibility. The Commentary goes on to state that elastic pile behaviour is commonly assumed for short bridges, but inelastic behaviour can be designed for if the piles have adequate ductility.

Section 7.8 Reinforced Concrete Buried Structures is contained in the Buried Structures section of the CHBDC. It describes the soils to be used for backfill of concrete structures, and cross-references a table in section 7.6 which lists the values of secant soil modulus to be used for each soil type, at various degrees of compaction. Section 7.6.2.3 of the Commentary describes the typical stress-strain relationship in soil, namely that it is non-linear and inelastic, taking on the form of a hyperbola.

Based on laboratory and field experience (Duncan et al. 1980; Byrne et al, 1987) recommend values of k_E (k_h) and m (n_h). They state that the values of E_s published in Table 7.5 of the CHBDC are reasonably conservative for all aspects of buried structure design.

2.3.3 IAB Design Considerations

The variation of soil stiffness in cohesive soils due to plastic strain hardening or degradation (Matlock, 1970); and densification of cohesionless soils (Gle and Woods, 1984) caused by cyclic action affects the behaviour of IABs over time, and should be accounted for in the design process. This consideration has led to designers specifying that certain foundation conditions be created to ensure IAB movement would not be overly restrained over time, and that a reduction in soil support create structural instability. These manufactured abutment configurations are those where natural soil conditions are replaced with a combination of manufactured aggregate and synthetic materials, all of which have parameters that are well understood. For instance, the designer may recommend that bedrock excavation and ensuing engineered backfilling be

performed prior to pile driving to ensure that pile fixity can be achieved. Designers often specify piles be oriented in weak-axis bending to facilitate abutment translation and rotation. Another common recommendation is that the top portion of each pile be encased in a loose medium such as pea gravel or pellets of polystyrene to promote flexibility. The latter has been implemented on several bridges owned by Alberta Transportation, including the Bear Creek and House River bridges on Highway 63. The pellets provide a minimal, uniform lateral pressure on the top portion of the piles, and ensure the stiffness within this zone remains relatively constant over time, and through variable climatic conditions. Another proposal to reduce friction and to limit bearing pressure on the underside of the pile cap is to install two horizontal layers of rigid insulation (which also serve as a form to prevent the infiltration of plastic concrete into the pile encasements). It also provides extra insulative protection against frost bridging into the pile encasement zone. As a last example, a layer of semi-rigid closed-cell compression foam may be specified to be placed on the backside of the abutment wall to ensure the passive resistance of the backfill soil does not overly restrain abutment rotation and translation. It also insulates the backfill from cold-bridging through the abutment face, thus reducing frost penetration into the backfill zone. All the measures described above, except weak axis pile bending, were specified and implemented on the Scoudouc bridge.

2.4 Recent Studies and Ongoing Research

Recent work by El Naggari et al. (2016) has focused on the Hardened Soil Model used to describe the behaviour of soil during the loading-unloading cycles which are characteristic of IABs. The Mohr-Coulomb soil model is one that many engineers have

historically used to describe soil-pile interaction; however, it is limited because it represents the soil as being elastic-perfectly plastic. The hardened soil model exemplifies the non-linear, hysteretic stress-strain relationship that is indicative of soil-structure systems that are subjected to cyclic loading. Using this theory, they predicted the stresses in the soil mass behind an instrumented IAB in New Brunswick, and forecast the earth pressures on the IAB's abutment wall. Their predictions were then compared to field measurements taken on the subject IAB. The hardened soil model results, when compared to the field measurements which were taken over a three-year period, agreed within a maximum error of 11.5%. This variance is substantially lower than the maximum 34% error when the Mohr Coulomb theory was used. Their work shows that the Hardening Soil Model can effectively simulate the non-linearity and hysteresis of soil behaviour when subjected to cyclic loading and unloading.

The bridge whose behaviour was modelled in the work described above, was the subject of a field study, during which Huntley and Valsangkar (2013) instrumented and studied the abutment movements and resulting abutment wall stresses over a three-year period. Field data from pressure cells, tilt meters and deformation meters installed behind the abutments of a 76m, two span, pile supported IAB showed that the application of typical Coulomb and Rankine theoretical passive earth pressure triangular distribution along the abutment wall was conservative. Though the recorded pressures near the top of the wall reached the passive pressure values, those at the centre and bottom of the abutment wall were much less. This is somewhat surprising as the primary mode of abutment movement for this specific bridge was found to be translation and not rotation. Broms and Ingelson (1971) considered IAB abutment rotation and developed a method by which the passive

earth pressure was limited to the top 1/3 of the abutment wall, then transitioned linearly to the active earth pressure at the base of the wall. Huntley and Valsangkar's measured wall pressures at mid and lower pressure cells were even less than estimates using Broms and Ingelson's method. The average pressure variation over the entire study period ranged from 50.1 to 58.6kPa for the east abutment, and 39.0 to 96.9kPa for the west abutment. The trend of abutment wall stress variation followed the diurnal and seasonal changes in ambient temperature, as expected; however, no ratcheting trend was observed, as some researchers such as Brena et al. (2007) had identified in earlier studies of IAB's. Huntley and Valsangkar (2014) expanded their study of the subject IAB to focus on pile bending and axial stresses caused by thermal expansion and contraction. Piles at each abutment had been fitted with strain gauges at 750mm, 1500mm and 2250mm down from the pile heads, and the recorded strains were converted to stress, and finally bending moment. The measured moments were compared to those of Winkler based models found in the Canadian Foundation Engineering Manual, and agreed with the predictions within reasonable accuracy when published values of n_h were used. The bottom strain gauge readings were opposite in sign from those above, which indicated that the point of curvature inflection was between the middle and bottom gauges. The Winkler models predicted a lower point of inflection; however, both the models and measurements showed that the piles in the weak-axis orientation were behaving as long piles with representative contra-flexure. The measured maximum stresses in the piles due to bending caused by thermal expansion and contraction ranged from 17% to 28% of the pile's yield stress of 300MPa. In addition to bending stresses, they measured axial stress variations in the piles due to thermal expansion and contraction of the bridge. They

observed that the piles were subjected to additional compressive forces during bridge contraction, and tensile forces when the bridge expanded. It is believed that during contraction, the soil pressure on the abutment wall approaches the active state, and the downward movement of the active soil wedge combined with the friction on the back of the wall result in a vertical force vector acting downward. Conversely, when the bridge expands, the soil pressure approaches the passive state, and the abutment wall pushes the passive soil wedge upward along the shallower critical shear plane, thus pulling on the piles. It is noteworthy to mention that the abutment wall friction tends to reduce the wall movement in this case; however, once the friction force is overcome, the wall will slide along the soil interface.

A study was conducted by Huang (2011) to define modified P-Y curves to be used to predict the behaviour of a laterally loaded pile in a soft clay that had been structurally improved. The top portion of the surrounding soil had been mixed with cementing agents to increase its stiffness to reduce the lateral pile deflection when subjected to lateral loading. Lateral deflections were reduced up to 480% in small-scale load tests, and up to 79% in full-scale load tests. This is consistent with the philosophies of Davisson and Gill (1963), who concluded that the near surface horizontal subgrade modulus was the controlling factor for pile response, and that soil investigations and characterizations should be focused on this zone. Huang supported the use of Winkler methodology as a versatile and practical approach; however, he had determined that the traditional method could not be used due to the non-homogeneity of the soil (improved soil radially surrounded by un-improved soil). Therefore, he presents a method of modifying P-Y curves that are typically developed by following procedures such as those published by Matlock (1970)

for the response of piles in soft clay, or Reese and Welch (1975) for the response of piles in stiff clay. Huang's method involved coupling two non-linear soil springs in series to represent the stiff improved clay and soft un-improved clay, and adjusting the stiffness to reflect the soil deflection attenuation at the front of the pile. The modified P-Y curves predicted the pile response accurately when compared to actual field measurements.

Kim et al. (2015) investigated six (6) methods of analyzing a 128m 3-span IAB for stresses induced by thermal movements. These included 1) Free Expansion, 2) Empirical Approximate, 3) 2D Static Analysis, 4) 2D Time History, 5) 3D Static Analysis, and 6) 3D Time History. The Free Expansion technique is recommended by AASHTO, and simply requires as inputs the girder coefficient of thermal expansion and length of bridge. It assumes that the pile heads will deflect by half of the thermal throw of the bridge girders, and it neglects the resistance of backfill. The pile is idealized as a free-standing cantilever with a fixed head, and length equal to that estimated by Abendroth and Greimann (1987). This method is crude, and should only be used for preliminary estimates of pile head deflection, shear and moment. The Empirical Approximate method was developed by Kim and Laman (2010a) after conducting parametric studies of 243 IAB's that incorporated a 2D, non-linear, time history analysis for a 75-year bridge life. Only five input variables are required, namely 1) the bridge thermal expansion coefficient, 2) the bridge length, 3) the backfill height, 4) the soil-pile stiffness, and 5) the backfill stiffness. This method does not consider time dependent concrete effects such as shrinkage or creep. The 2D Static Analysis idealizes the superstructure and substructure as a frame with representative elemental characteristics such as mass and stiffness. The backfill soil is represented as a classic Rankine triangular distribution of passive soil

pressure, and the soil surrounding the piles is represented by discrete non-linear springs defined by P-Y curves. The 2D Time History method is similarly modelled, except with hysteresis loops to represent the loading and unloading of the soil as the variations in thermal movements are continuously generated by a sinusoidal function. The unrecoverable deformation characteristics of the modelled soil must also be included to accurately mimic the system's cyclic behaviour over the 75-year life expectancy of the bridge. An elasto-plastic P-Y curve proposed by Taciroglu et al. (2003), which can incorporate the elasto-plastic behaviour by generating an unloading branch using classical plasticity theory, was implemented in the abutment-backfill and soil-pile interaction models. The 2D models provide reasonable results; however, they do not allow the assessment of individual components as the system is idealized as an "average". The 3D Static Analysis and 3D Time History models can re-distribute stresses across the deck or diaphragms; therefore, these more closely represent the actual mechanics of IAB's. The 3D Time History model produced the most accurate results when compared to the field measurements of IAB bridge responses. These methods were validated based on, and calibrated to, results obtained from a 7-year field measurements collection program at four IABs with lengths of 19 to 128m.

Abendroth and Greimann (2005) conducted field tests on two prestressed concrete girder IAB's over a period of two years, with a focus on thermally induced stresses. They found, among other things, that the stress in at least one abutment pile exceeded the yield stress, and that the girder-abutment and abutment-pile connections behaved as rigid joints. The experimental data was used to calibrate and refine FEM's of the bridges. Two analysis methods are presented to predict the member-end forces for the piles and girders and the

soil pressures and soil-frictional forces that act on an integral abutment, when an integral-abutment bridge is subjected to gravity and thermal loadings. The first analysis method involves the use of two-dimensional, frame models of an integral-abutment bridge. The second analysis method does not require the use of a structural model for the entire bridge. This analysis method considers that the member-end forces for the abutment piles are based on the maximum resistance for each pile, and that the maximum soil pressures and the corresponding soil-frictional forces are based on full-passive-soil resistance. Both analysis methods include the effect of soil settlement from the bottom of the abutment-pile cap and the application of equivalent-cantilever lengths for the abutment piles. These equivalent cantilever lengths were calculated by using the method developed by Abendroth and Greimann (1987). Abendroth and Greimann (2005) also state that maximum IAB bridge length may be limited by the pile ductility limit state. To maximize the ductility capacity for an abutment pile, the upper portion of the pile length should be in a pre-bored hole that is filled with a material which has very low stiffness, such as a bentonite slurry, and the pile should be oriented in weak-axis bending. One of their recommendations is that further experimental studies be conducted on long-span, steel girder IAB's to obtain a better overall understanding of the behaviour of IAB's.

A study was conducted by Cook and Abendroth (2010) during which a 94m, 3-span, steel girder IAB was instrumented and surveyed for movements due to thermal forces. The H-Piles were oriented in weak-axis bending, and the abutment configuration was unique in that the bottom portion of the steel H-piles were cast in concrete shafts, instead of being driven in soil, and the top 5.8m were backfilled with gravel. This was done to eliminate excessive vibration during pile installation. Another item to note is the fact that an error

was committed during construction, and HP10x87 piles instead of HP12x84 piles were installed at the north abutment. Greater movement was measured at the north abutment (0.84 in.) compared to the south abutment (0.56 in.), and this was partly attributable to the lower soil-pile system stiffness at the north abutment. Another contributing factor was that the north abutment was narrower than the south abutment; therefore, the resistance due to the granular backfill was less. The author also notes that the maximum overall change in bridge length is 2.50 in.; therefore, one must assume that the spans are simply supported, and expansion joints between spans accommodate the difference between the 2.50 in. and 1.44 in. A simple equivalent cantilever computational model by Abendroth and Greimann (2005) (which is the same model that Greimann introduced in 1987) was used to estimate the pile bending moments, and these compared well with the moment values that were calculated with measured pile strains. The measured strains 450mm above the shafts and 450mm below the abutments were similar in magnitude; however, they had opposite signs, which is indicative of pile contra-flexure. This is also consistent with the Abendroth and Greimann cantilever model of fixed-head condition.

2.5 Scoudouc Bridge

2.5.1 General Arrangement

The Scoudouc bridge is a fully integral abutment, 133m continuous three-span, steel plate girder bridge with a composite concrete deck designed to carry Scoudouc Industrial Drive traffic over Route 15 near Moncton, New Brunswick. One half of the symmetrical elevation of the bridge is depicted in Figure 2.4.

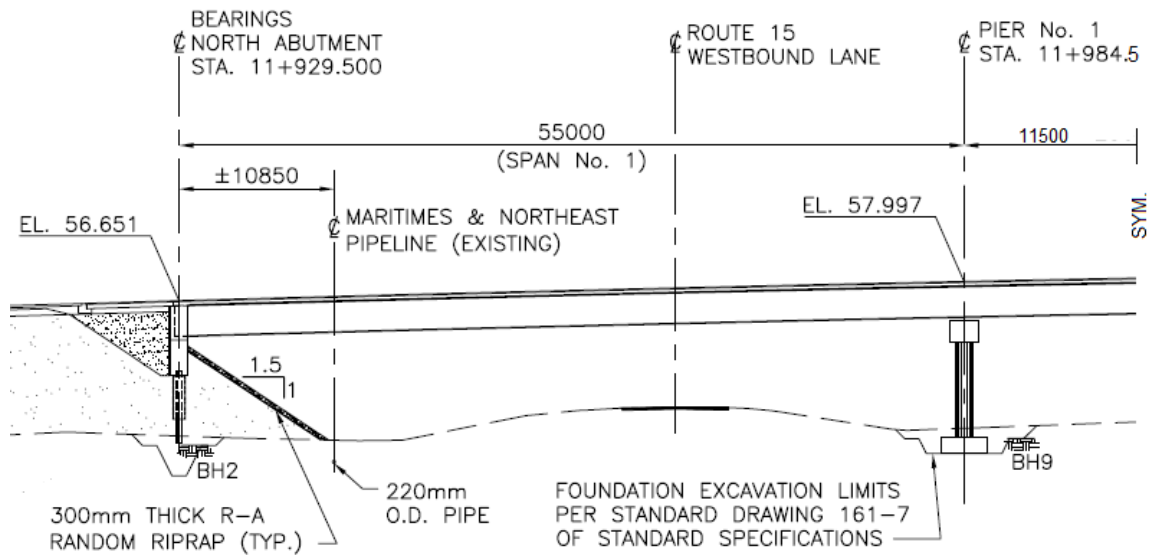


Figure 2.4 Partial Elevation of Scoudoc Bridge. (NBDTI, 2009)

The design life of the bridge is 75 years. The concrete abutments are founded on steel H-piles, while both concrete piers' footings bear on sandstone bedrock. The overpass crosses Route 15 at a right angle, so there is no skew nor super-elevation to the bridge. The bridge deck has a 1.9% slope, and 3.0% crown. A cross-section of the bridge is shown in Figure 2.5.

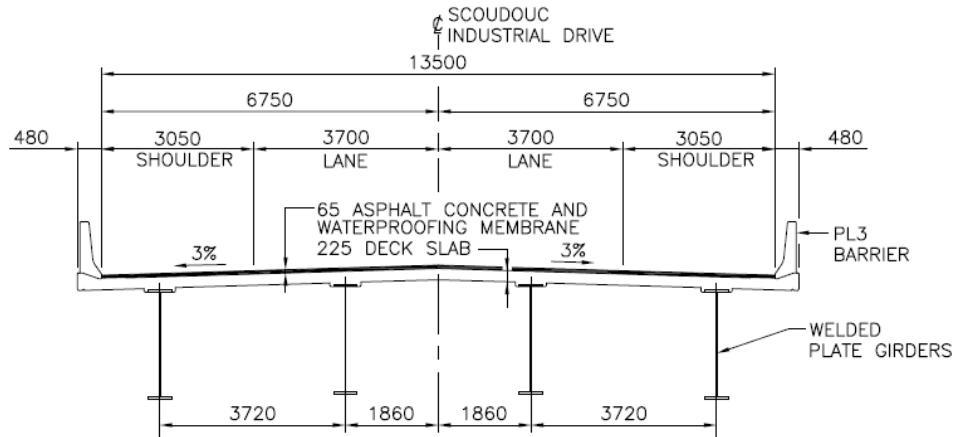


Figure 2.5 Cross-Section of Scoudouc Bridge. (NBDTI, 2009)

The bridge is owned and operated by the New Brunswick Department of Transportation and Infrastructure (NBDTI). The structural design was conducted by Roy Consultants of Bathurst, New Brunswick, with the support of the Engineering Department of NBDTI.

At the time of writing, the Scoudouc bridge was the longest fully integral abutment bridge in New Brunswick.

The abutment configuration is shown in Figure 2.6.

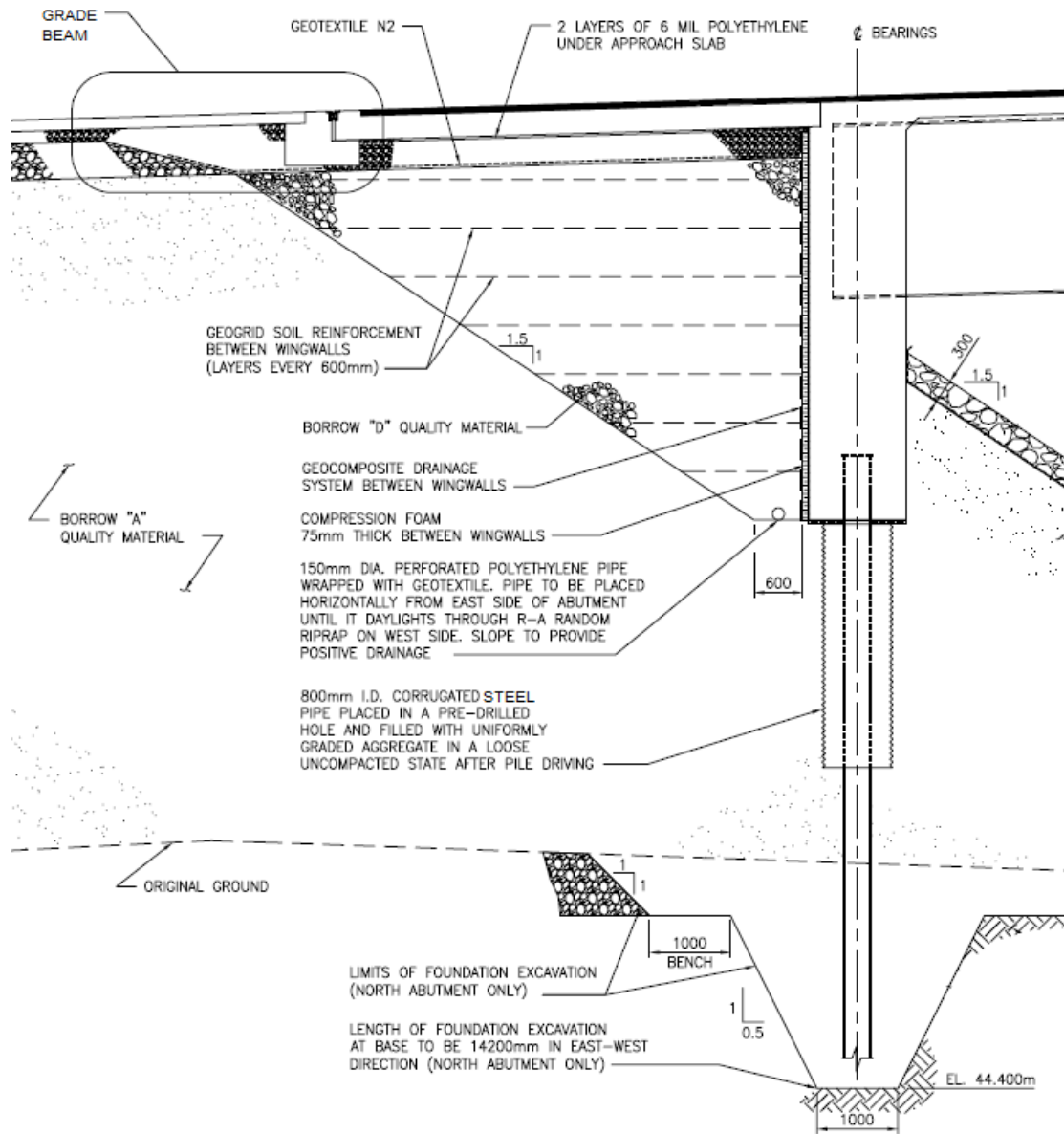


Figure 2.6 Abutment Configuration of the Scoudoc Bridge. (NBDTI, 2009)

2.5.2 Site Geology

The site is generally well-drained with rolling topography, with no indication of a water table in any of the ten (10) test boreholes. The top layer of silty or gravelly sand varies in thickness from 1m to 2m. The sand overlays a layer of brown sandstone which varies in

thickness from 2m to 6m. A grey, bedded sandstone underlies the brown sandstone, and is present at the bottom of all boreholes. The shallowest borehole was advanced to 6m from the natural ground surface, while the deepest was terminated at 9m depth.

The Standard Penetration Test (SPT) values in the sand ranged from a low of 8, to a high of greater than 50 at the brown sandstone interface. The Rock Quality Designation (RQD) within the brown sandstone varied from a low of 0, to a high of 34, while that in the underlying grey sandstone varied from a low of 0 to a high of 43.

The Scoudouc bridge borehole logs, along with a key map of their locations, can be found in Appendix A.

2.5.3 Design Approach

The bridge pile foundation was designed by Roy Consultants of Bathurst, New Brunswick, to the Canadian Highway Bridge Design Code CAN CSA S6-06 using a hybrid FEM and Winkler approach. A model of the superstructure and substructure was created, and soil springs were added to the piles and diaphragm to simulate SSI. Due to the large anticipated thermal movements at the abutments, the piles were oriented in strong-axis bending to avoid yielding. Due to the shallow sandstone bedrock, it was decided to recommend bedrock excavation to a depth of 9m below the bottom of the diaphragm, such that pile fixity could be achieved. The pile tips bear on sound sandstone bedrock (see Figure 2.6). The soil-pile system was designed to be flexible in the upper 3m by encasing the piles in 800mm diameter corrugated steel pipes and infilling with “uniformly graded aggregate in a loose un-compacted state after pile driving”. (The

contractor installed 8mm pea gravel in the sleeves). The 2m thick layer immediately below the sleeves is Type A Engineered Granular Fill compacted to 95% Standard Proctor Dry Density, while the lower portion of the piles are embedded in Type B Engineered Granular Fill compacted to 95% Standard Proctor Dry Density. It is assumed that these soil types are consistent with the Canadian Highway Bridge Design Code CAN CSA S6-14 Soil Groups I and II, respectively, as described in Table 7.4 *Soil Classifications*. The abutment backwall and wingwalls are backfilled with Borrow D material, which consists of 75mm-minus gravel compacted to 95% Standard Proctor Dry Density, with geogrid placed at every 600mm lift. A closed-cell compression foam in a single 75mm layer was specified to be installed on the inside face of the abutment diaphragm and wingwalls to reduce the effects of passive soil pressure and friction during translation and rotation of the abutment wall. To reduce the bearing pressure on the bottom of the abutment diaphragm, and to reduce frictional forces at the soil-abutment interface, the designer specified that two layers of 50mm extruded polystyrene rigid insulation be installed.

2.5.4 Construction

The construction sequence for the lower portion of each abutment diaphragm began with the foundation excavation, including the overburden and the bedrock, to approximately 8m below the abutment diaphragm. A well graded granular backfill was used to backfill each excavation to 3m below the abutment diaphragm, and corrugated steel pipes were stood plumb at each pile location, and braced on top of the fill. Backfilling operations resumed around the corrugated steel pipes, up to the top of the pipes. A pile was driven

concentrically within each pipe, to refusal, and then was cut-off 0.8m above the top of the pipe (approximately at the bottom of the diaphragm). Uniformly graded 8mm pea gravel was placed in pipes, and a steel pile cap was welded to the top of each pile. Two layers of rigid insulation were placed on the backfill, to cover the diaphragm footprint, with only the H-piles protruding. The lower abutment diaphragm back form was erected, and steel reinforcing bars were installed around the piles and the abutment diaphragm. The lower abutment diaphragm side forms and front form were installed, and the steel reinforcing bars were secured. Finally, the lower abutment diaphragm, including temporary seats, was poured.

Chapter 3 - Field Tests

3.1 Preliminary Pile Tests

A preliminary test was conducted at the Picadilly Potash Mine in Sussex, New Brunswick, on a pile (T-3024) that had been driven to support a salt shed. A Pile Driving Analyzer was used to measure the strain in an HP 360x132 pile that was subjected to a lateral head load. A hand-operated hydraulic jack was anchored to the back of an excavator bucket to conduct a static push test in the weak-axis direction. Head deflection measurements were taken with a transit and graduated ruler.

The piles were driven into a silty sand soil, and unlike the piles at the Scoudouc bridge, they were not encased in a steel sleeve filled with uniform, loose aggregate. The results of the west lateral load test on pile T-3024 demonstrated that the soil-pile system's head stiffness had an initial linear response of 32100kN/m over the first 1 mm of deflection, then lost stiffness but remained linear ($R^2=0.96$) at an average of 7686kN/m up to 17mm of head deflection. The results of the east lateral load test on pile T-3024 demonstrated that the soil-pile system's head stiffness had an initial linear response of 22900kN/m over the first 1 mm of deflection, then lost stiffness but remained linear ($R^2=0.99$) at an average of 8321kN/m up to 19mm of head deflection. Figures 3.1 and 3.2 show the results of the static push test of pile T-3024 in the West and East directions, respectively.

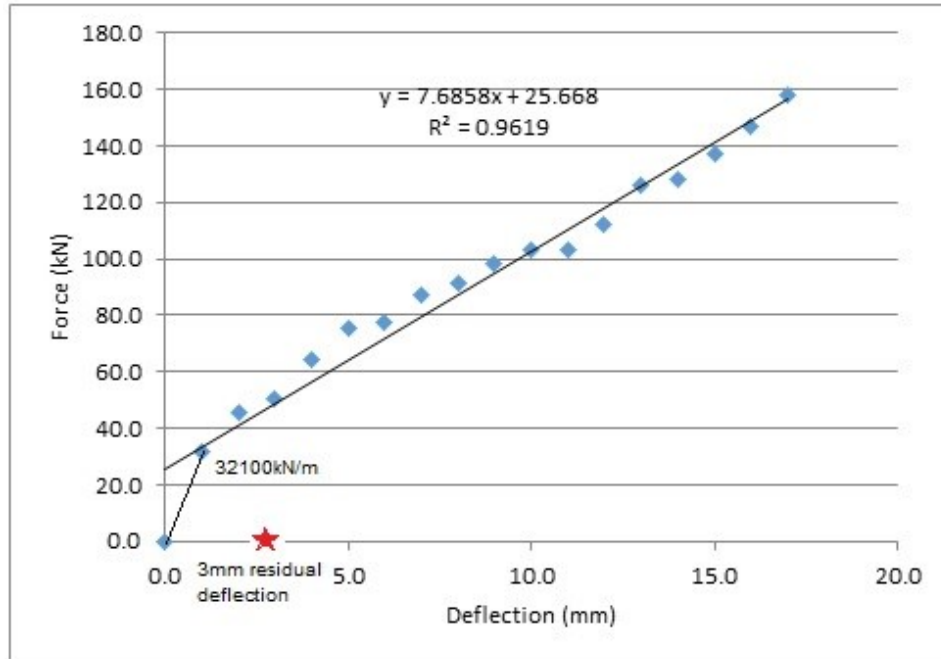


Figure 3.1 Response to Static Push Test of Pile T-3024 in the West Direction.

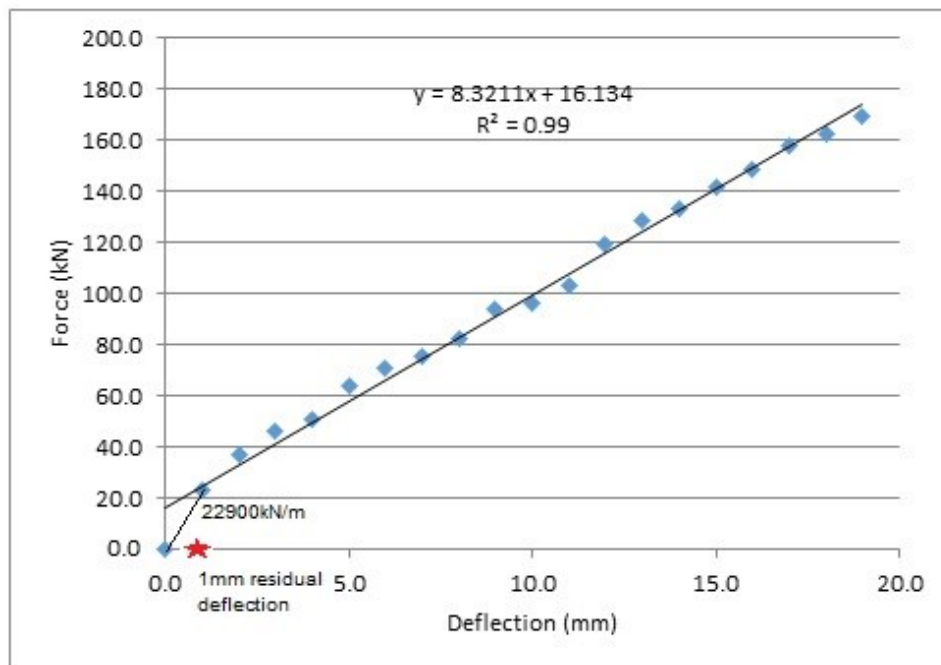


Figure 3.2 Response to Static Push Test of Pile T-3024 in the East Direction.

Each lateral load test graph exhibits a marked increase in stiffness at 1mm of head deflection. This may be due to the densification of soil as the lateral soil pressure increased from an at-rest condition to a passive condition, up to an ultimate soil pressure at its yield point. The pile response beyond this yield point is less stiff and linear.

The push test in the West direction ended with a residual head deflection of 3mm upon unloading, and the push test in the East direction ended with a residual head deflection of 1mm upon unloading. The residual deflection may be caused by the infill of soil on the back-side of the pile as it is pushed forward, preventing the pile from returning to its initial position. This pile was driven into a silty sand; therefore, it is assumed to have some cohesion (borehole data was only available information, and is included in Appendix C). This may explain why the residual strain after the first test (3mm) was greater than that after the second test (1mm), which marked the completion of the first full cycle. Also, soil friction along the sides of the pile may be resisting the sum of the elastic rebound of the pile and the active soil pressure as the pile moves away from the yielded soil as the load is released. The results from these preliminary tests are tabulated in Appendix C.

3.2 Scoudouc Bridge Pile Push Tests

3.2.1 Test Setup

Lateral pile push tests were conducted on four (4) piles at the Scoudouc bridge to measure the soil-pile system stiffness. These are pile P5N, P10N, P5S and P10S. Figure

3.3 shows the location of the P5N and P10N piles at the north abutment. Piles P5S and P10S are mirror reflections of these, located at the south abutment.

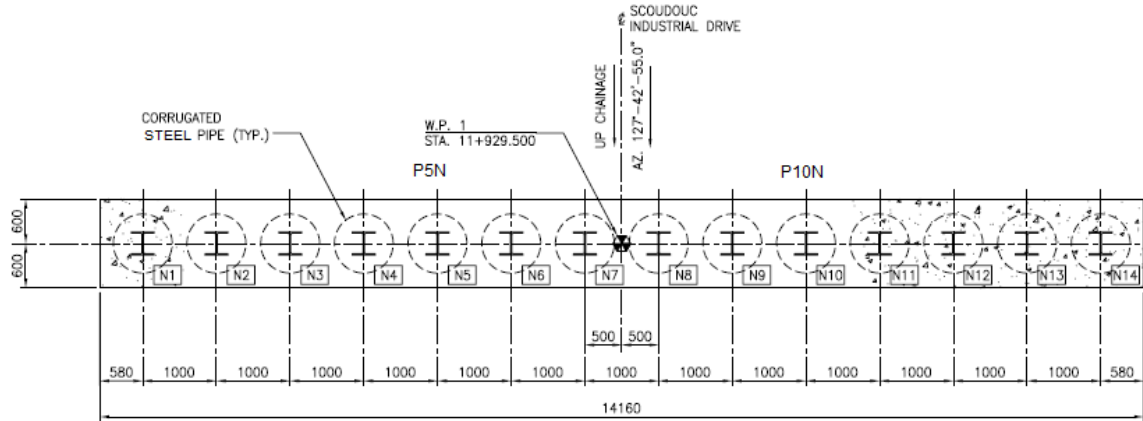


Figure 3.3 Location of piles P5N and P10N. (NBDTI, 2009)

A PAX Pile Driving Analyzer, in-line pressure gauge, and survey transit were used to measure the lateral response of an HP310x132 pile that had a lateral load imparted on its head in the strong-axis direction. As mill certificates or material test records were unavailable, the moment of inertia in strong axis bending, I_x , was assumed to be $293.0 \times 10^6 \text{ mm}^4$, and Young's modulus of elasticity, E , was assumed to be $205 \times 10^6 \text{ kPa}$. These values were obtained from the STAAD.Pro database, which includes typical imperial steel mill values, and were converted to metric.

The adjacent HP310x132 piles were used as reaction piles, and an HP310x132 beam provided the jack support at 0.45m below the top of the pile. The piles were separated horizontally by 1m. Two hand-operated hydraulic jacks were positioned between the jacking beam and adjacent reaction piles to push the pile, and a transit was used to

measure pile head deflection. A strain gauge connected to a PAX Pile Driving Analyzer measured the extreme fibre bending strain at approximately 1m below the pile head. The jack was pressurized until the first head deflection increment of 2mm was reached, and the pressure gauge and strain gauge readings were recorded. This process continued until a free head deflection resulting in a pile bending stress equaling approximately half of the yield stress was reached. The maximum lateral head load was estimated by using Brom's solution, which uses Rankine's passive soil pressure coefficient in combination with beam theory to limit the head load.

A photo showing the general test configuration, as well as schematic plan and elevation views with dimensions and components of the test apparatus are shown in Figures 3.4, 3.5, and 3.6 respectively.



Figure 3.4 Photo of Test Configuration for Static Push Test of Pile P5N.

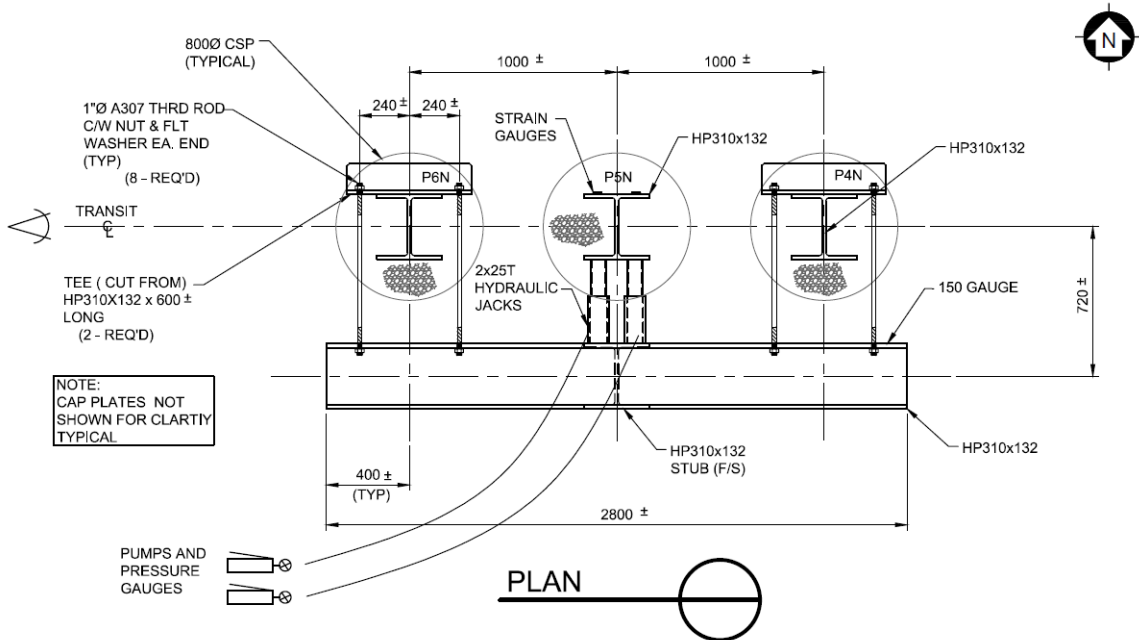


Figure 3.5 Plan View of Test Configuration for Static Push Test of Pile P5N.

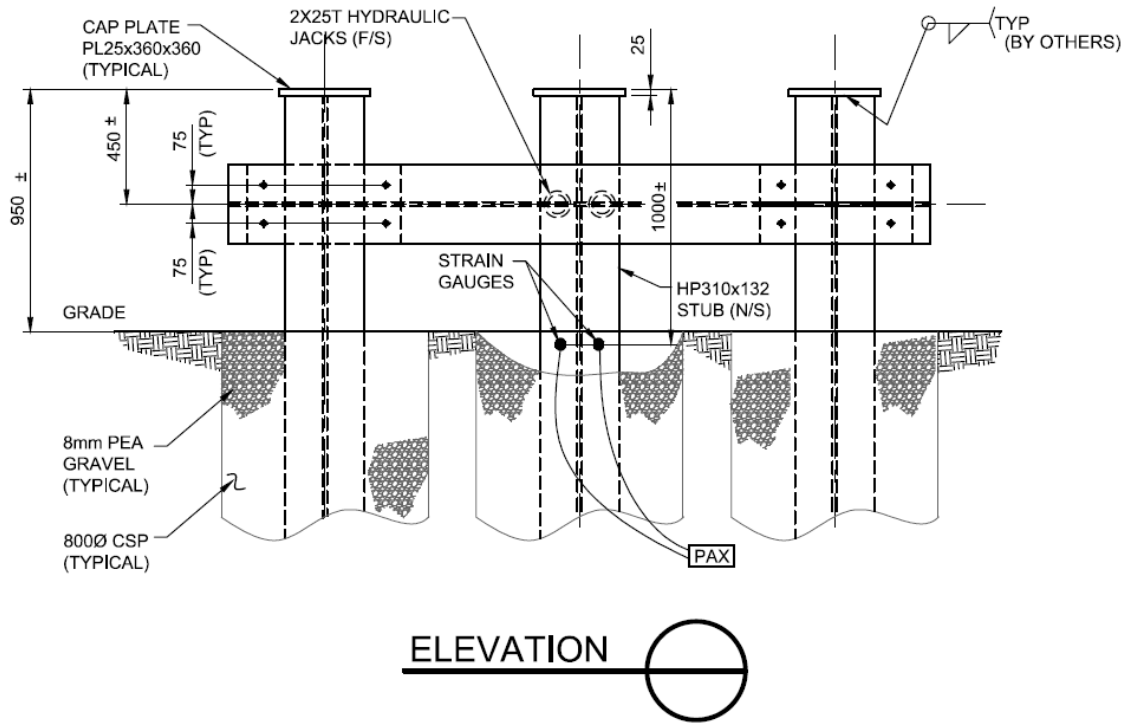


Figure 3.6 Elevation View of Test Configuration for Static Push Test of Pile P5N.

3.2.2 Test Results

The P5N pile head was pushed incrementally over a range of 54mm, at 2mm increments. The values of pile strain and head load were measured at each increment, and duly recorded.

The results of the static push test on P5N are displayed in tabular form in Appendix D, and graphically in Figure 3.7.

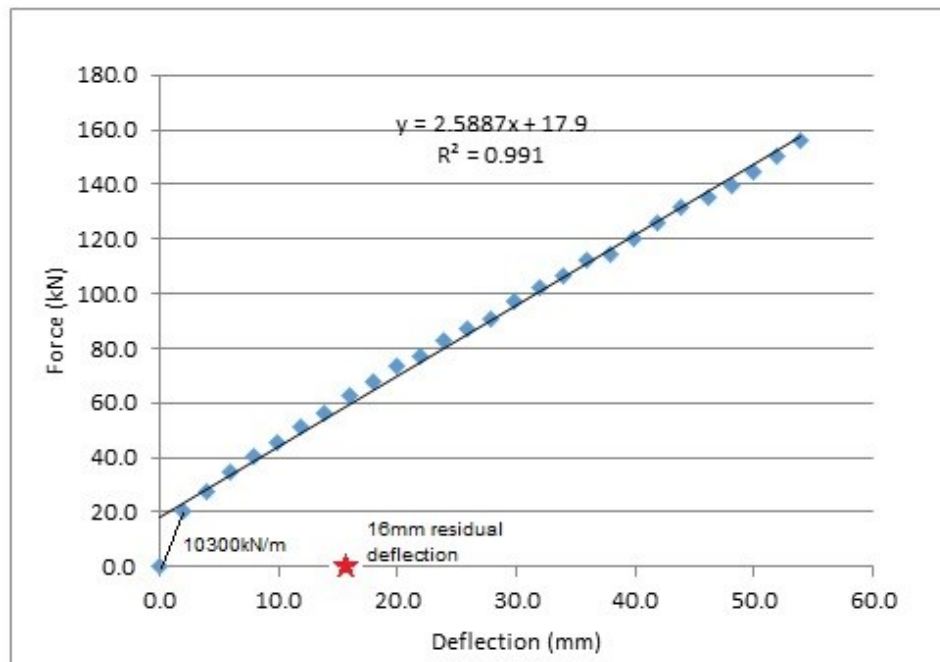


Figure 3.7 Response to Static Push Test of Pile P5N.

The results of the lateral load test on pile P5N demonstrated that the soil-pile system's head stiffness had an initial linear response of 10300kN/m over the first 2 mm of

deflection, then lost stiffness but remained linear ($R^2=0.99$) at an average of 2589kN/m up to 54mm of head deflection. The pile head had a residual head deflection of 16mm upon unloading. The measured bending stress (MPa) in the pile, 1m below the pile head and 0.55m below the point of load application, was 4.3, 10.7, 18.3, 25.3, 32.1, 39.1 and 41.9 for head deflections (mm) of 2, 10, 20, 30, 40, 50, and 54 respectively.

Pile P10N had a lateral test performed on it; however, a heavy rain and flash freeze event occurred in the days leading up to the test, and this created a frozen, and very stiff layer of pea gravel at the top of the Corrugated Steel Pipe (CSP) sleeve. A graph of the measured head deflection caused by an increasing lateral head load is shown in Figure 3.8.

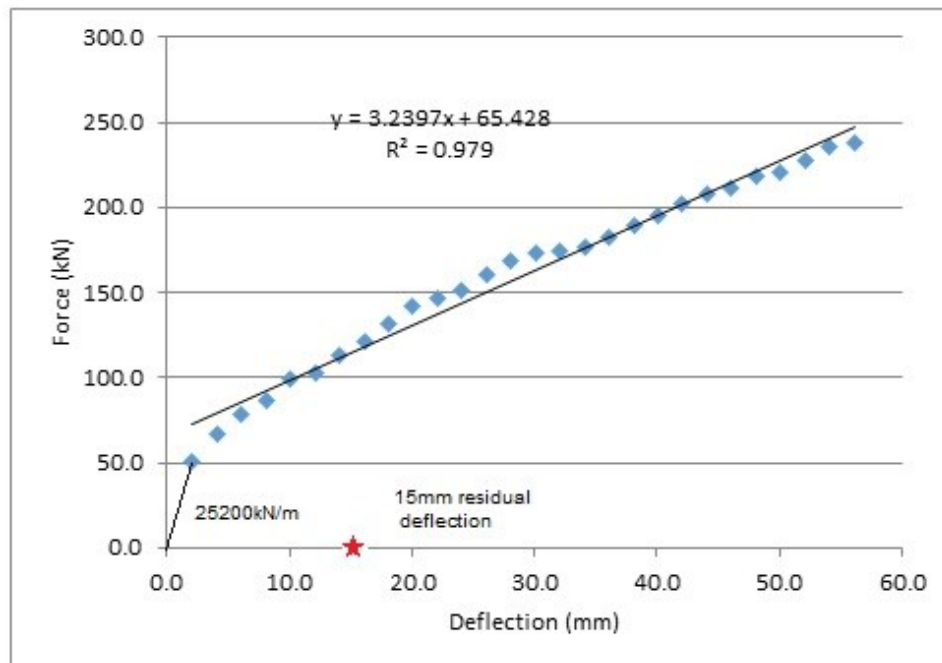


Figure 3.8 Response to Static Push Test of Pile P10N.

The results of the lateral load test on pile P10N demonstrated that the soil-pile system's head stiffness had an initial linear response of 25200kN/m over the first 2 mm of deflection, then lost stiffness but remained linear ($R^2=0.98$) at an average of 3240kN/m up to 56mm of head deflection. The pile had a residual head deflection of 15mm upon unloading.

A photo of a crack forming around the steel sleeve encasing pile P10N during the lateral load test is presented in Figure 3.9.

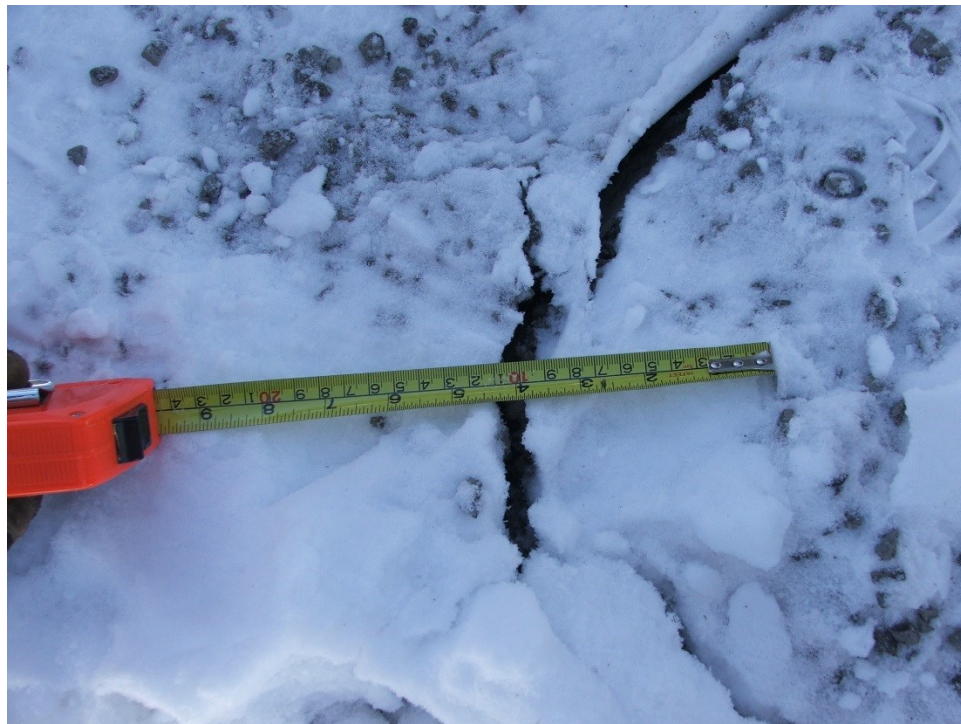


Figure 3.9 Crack Forming Along the Perimeter of Steel Sleeve of Pile P10N.

Piles P5S and P10S had lateral load tests performed; however, the electronic files containing the strain measurements were lost before a copy could be created. Graphs of the measured head deflection caused by an increasing lateral head load are shown in Figures 3.10 and 3.11, respectively.

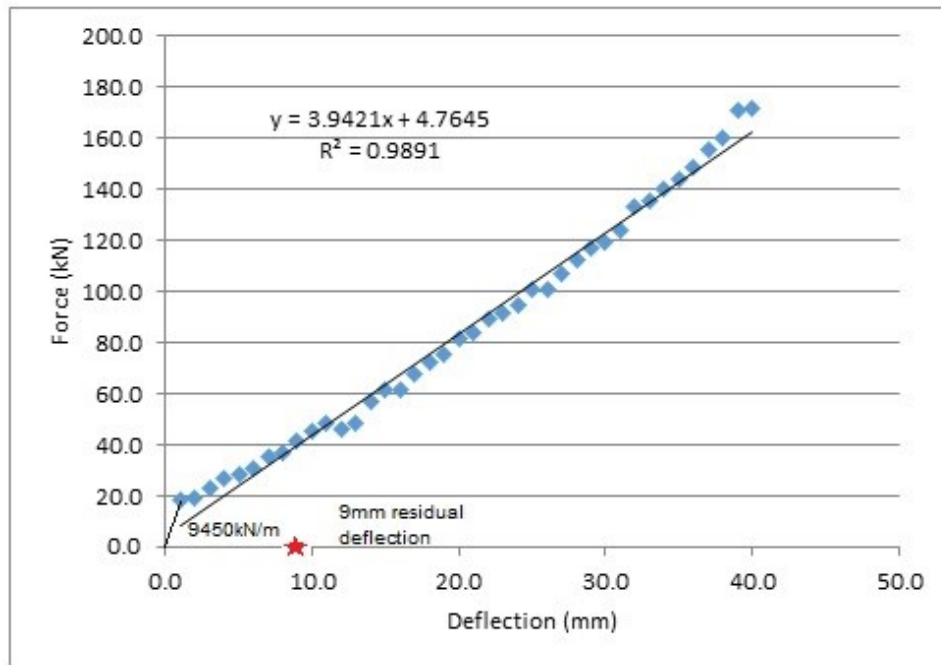


Figure 3.10 Response to Static Push Test of Pile P5S.

The results of the lateral load test on pile P5S demonstrated that the soil-pile system's head stiffness had an initial linear response of 9450kN/m over the first 2 mm of deflection, then lost stiffness but remained linear ($R^2=0.99$) at an average of 3942kN/m up to 40mm of head deflection. The pile had a residual head deflection of 9mm upon unloading.

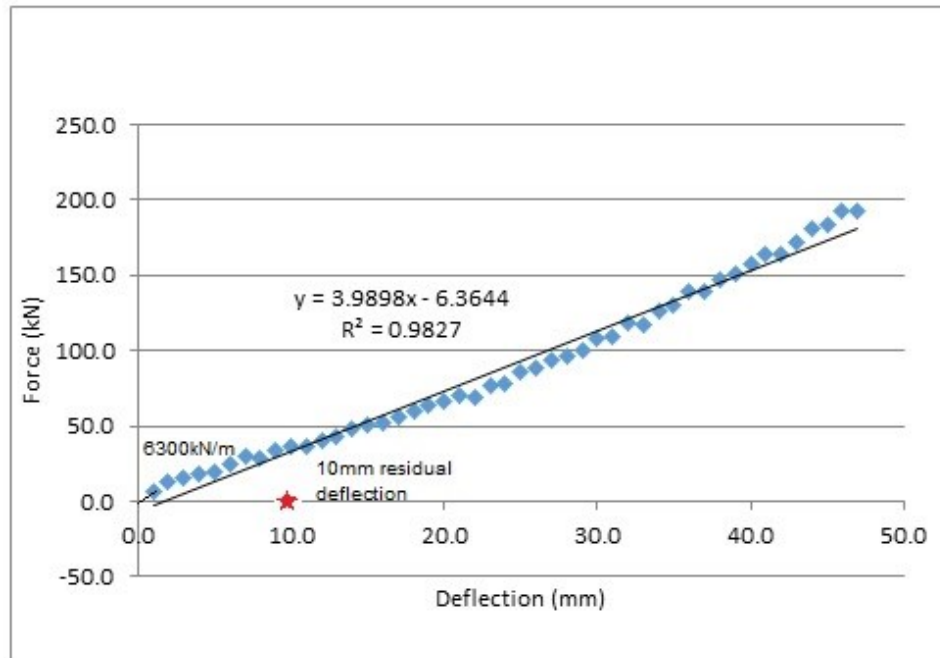


Figure 3.11 Response to Static Push Test of Pile P10S.

The results of the lateral load test on pile P10S demonstrated that the soil-pile system's head stiffness had an initial linear response of 6300kN/m over the first 2 mm of deflection, then lost stiffness but remained linear ($R^2=0.98$) at an average of 3990kN/m up to 47mm of head deflection. The pile had a residual head deflection of 10mm upon unloading.

Due to the loss of strain data for piles P5S and P10S, and the frozen pea gravel infill at pile P10N, the field test results for pile P5N will be assumed to be representative of all piles, and will be used to perform the various analyses in this paper. It is also the reason why pile P5N was chosen to be instrumented for the live load test.

Table 3.1 displays the results from the Scoudouc lateral pile tests, for comparison.

Table 3.1 Results of Scoudouc Lateral Load Tests.

Pile	Initial Stiffness (kN/m)	Subsequent Stiffness (kN/m)	Maximum Deflection (mm)	Residual Deflection (mm)	% of Maximum Deflection
5N	10300	2589	54	16	30
10N	25200	3240	56	15	27
5S	9450	3942	40	9	23
10S	6300	3990	47	10	21

The values of initial stiffness were greater at the north abutment than they were at the south abutment; however, the subsequent stiffnesses beyond a head deflection of 2mm were greater at the south abutment. The highest value of initial stiffness was 25200kN/m, observed at P10N, which had a frozen top layer of pea gravel 0.35m deep. The lowest initial stiffness was 6300kN/m, observed at P10S. Once the soil-pile systems were mobilized beyond 2mm of head deflection, the range of stiffnesses decreased, and a low value of 2589kN/m was observed at P5N, while a high value of 3990kN/m was observed at P10S. The variation in initial stiffness could be due to gradation, moisture and temperature differences in the pea gravel infill upon application of the load, as well as differences in the state of aggregate interlock within the infill matrix upon load application. The differences in the subsequent stiffnesses may be attributable to the variation in gradation and density of the soils underlying the pipe sleeves.

When comparing the values of residual deflection from the Picadilly tests and Scoudouc tests, one notices that the residual deflections observed during the former (2mm average) were much smaller than those of the latter (12.5mm average). This may be attributable to the difference in cohesion of both soils. The Picadilly soil is a silty sand with a small

fraction of clay and silt particles (no gradation results available); therefore, it most certainly has some cohesion to prevent the soil from falling into the void left by the pile advancement. On the contrary, the soil at Scoudouc is a very clean, uniform gravel that has no clay or silt fraction. This soil is susceptible to collapse when the confining stress is removed, such as on the backside of the moving pile.

All subsequent stiffness values beyond a 2mm head deflection exhibit linear behaviour. Considering the soil contributes to the stiffness of the soil-pile system (as evidenced by the residual deflections noted earlier), and that soil usually exhibits non-linear behaviour at high strains, this is somewhat surprising. One thought is that the soil particles are constantly re-arranging themselves with the advancement of the pile within the steel sleeve, and that the normal and shear contact stresses increase linearly during the process. There may exist a “flow” of particles from the front of the pile to the CSP interface, then split to follow the inside perimeter of the CSP sleeve, to finally rest at the backside of the pile once the push is completed. This hypothetical phenomenon is beyond the scope of this work, and should be investigated further in an independent study. Also, it was assumed that the interaction between the reaction piles and test pile is insignificant, and has a negligible influence on the test results as they are encased in a sleeve which is filled with a loose medium. This should be studied further to confirm whether or not this degree of isolation is adequate, or if the pile group effect should be considered and a factor applied to the results.

Pile P5N was chosen to be instrumented, and represents all piles in modelling, because the south abutment was constructed before funding could be secured, which eliminated piles P5S and P10S (strain data was also lost). Also, pile P10N and the pea gravel infill

had frozen; therefore, it would not be representative of typical pile behaviour. Two strain gauges were installed at 1.0m below the pile head, on opposite faces of the pile (see Figure 3.15) such that axial and bending strains could be differentiated.

3.3 Scoudouc Bridge Live Load Test

3.3.1 Test Setup

A live load test was conducted on the north half of the bridge to measure deck deflection and incremental pile strain under vehicular loading. It was decided to conduct a live load test on only half of the bridge as it is symmetrical about the middle of its centre span, and the north half was chosen because only pile P5N, located at the north abutment, was instrumented. A fully-loaded end-dump gravel truck having a mass of 41460kg incrementally moved along the centerline of the bridge, while deck deflection and pile strain were measured. This test truck configuration was chosen because gravel hauling activities were being carried out near the site, and this was the heaviest truck configuration that was available. Though a formal analysis had not been conducted prior to the live load test, it was thought that the truck was heavy enough to deflect the deck to measure with the level and rod, and distribute stresses to the instrumented P5N pile. A schematic of the idealized live load test vehicle and photo of the test configuration are shown in Figures 3.12 and 3.13, respectively.

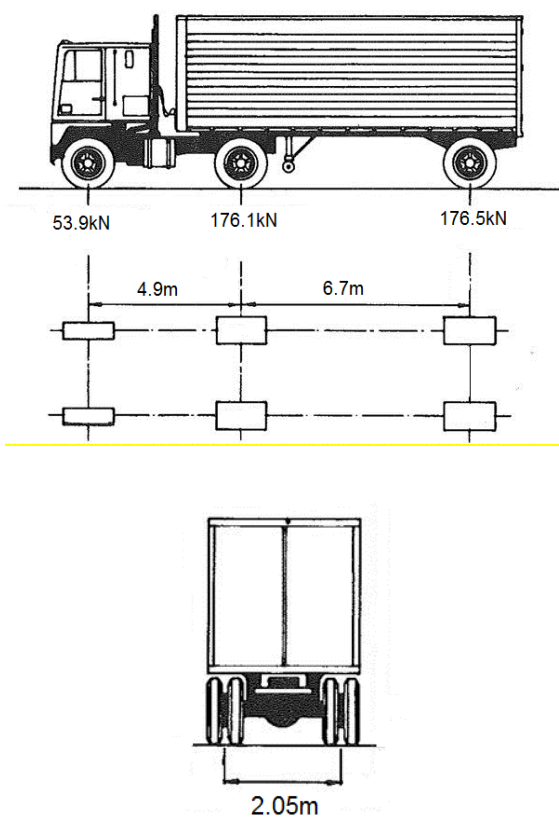


Figure 3.12 Schematic of Idealized Live Load Test Vehicle. (AASHTO Standard Specifications for Highway Bridges, 2002, with modifications)



Figure 3.13 Photo of Scoudouc Live Load Test Configuration.

The deck deflection was measured adjacent to the rear driving axle with a survey level and grade rod. The P5N pile strains were measured with a PAX Pile Driving Analyzer (see Figure 3.14) that was connected to the leads from two strain gauges that had been installed during construction. The strain gauges are located on opposite faces of the pile, 1m below the pile head. A thermometer was also installed on P5N with the intent of recording temperatures at the location of the strain gauge; however, the thermometer malfunctioned and no temperature readings were taken (see Figure 3.15). The goal was to monitor the temperature of the pile sleeve infill to establish how long it would remain in a frozen state once the backfill was installed and insulated the infill. It is conceivable that a climatological event, such as the flash freeze that occurred prior to the P10N pile test, could happen again. This could result in an increased soil-pile stiffness that would exist during construction period thermal expansion and contraction cycles, or even once the bridge opens to traffic.



Figure 3.14 Data Logger Indicating Strains on Pile P5N.



Figure 3.15 Strain Gauges and Wireless Thermometer Installed on Pile P5N.

A braking test was also conducted on the bridge, where the truck drove on the deck at a speed of 60km/h, and stopped within 30m. The assumption was that the deceleration was uniform over the stopping distance. The theoretical stopping time of 3.6 seconds matched field observations. Considering the stopping time, and a change in velocity from 60km/h to 0km/h, the deceleration was -4.63m/s^2 . The product of this deceleration and the mass of the truck, or 41460kg, resulted in a braking force of 192.0kN. This compares well with the CHBDC lane braking load of 299.7kN for the Scoudouc bridge, considering the test truck weighs approximately 2/3 of the CHBDC CL-625 truck.

3.3.2 Test Results

The maximum measured deck deflection was 11mm, measured at the rear driving axle, while the truck was moving southward. This occurred 26m from the north end of the bridge, as the front axle of the truck was 32m from the north abutment. It should be noted that measurements were taken at the rear driver axle of a tandem pair of axles, and the distance from the centre of the tandem axles to the front axle was 4.9m, while the distance between axles comprising the tandem pair was 1.3m. Figure 3.16 shows the truck's placement at maximum deck deflection.

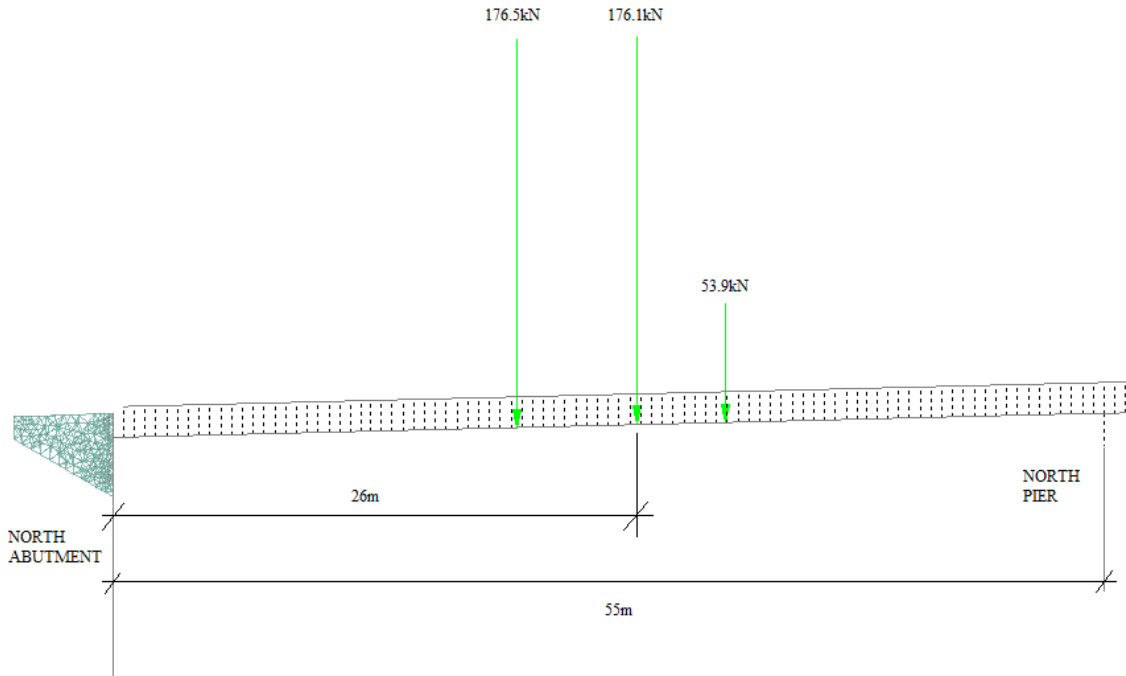


Figure 3.16 Truck Position and Direction at Maximum Deck Deflection.

Measurements were taken 1.8m from the centreline of the bridge, outside of the truck's footprint. The associated incremental pile stress due to the truck load was -4MPa (indicating tension) on the north face of P5N, and +6MPa on the south face. This represented the maximum range of incremental tensile and compressive stresses on pile P5N for the entire live load test, and can be interpreted as 1MPa of axial compression plus/minus 5MPa of bending stress. In turn, these values of stress are used to calculate a maximum measured axial force of 16.7kN and a maximum bending moment of 9.5kNm. It was noted that the stresses remained as such, even once the truck drove off the bridge. This either indicated that there was residual strain in pile P5N, or that the strain gauge malfunctioned. This residual deflection may be attributable to the loose pea gravel filling the void on the backside of the pile as it advanced, as described in Section 3.2.2, considering this was the first vehicular crossing of the bridge. Monitoring of the long-

term pile strain after removal of the vehicular load was not performed as this was beyond the scope of this work. Further studies should be conducted to confirm the variation of the residual deflection with time.

The effects of the horizontal load due to the braking test were undetected by the pile P5N strain gauge. This may be due to the lower-limit strain threshold of the gauges. The expected measured microstrain for an estimated lateral fixed pile head deflection of 0.063mm is 1.4 microstrain, and the calibration for these gauges entails applying a range of 0 microstrain to 1340 microstrain and observing the output voltage (see Appendix J for calibration sheets). The expected value only represents 0.2% of the average calibrated value; therefore, it is very possible that the actual strains were not able to be measured by the gauges.

The results of the static deck deflection test are displayed in Appendix E.

The measured deck deflections due to the truck load are presented in Figure 3.16 below:

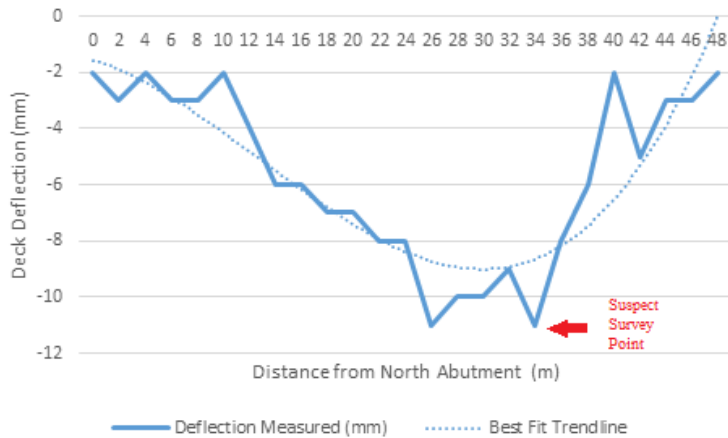


Figure 3.17 Measured Deck Deflections due to Truck Load.

The measurements were taken at the rear drive wheel, and 1.8m from the centerline of the bridge, while the truck drove from the north abutment towards the south abutment. The north end of the bridge deck is shown in Figure 3.16, as the bridge is symmetrical and the live load test was conducted on approximately half of the bridge only. Only 48m of the deck is shown in Figure 3.15 because the survey data from 50m to 66m had some uncertainty, as a backsight reading for a turning point was questionable. Also, the reading at 34m from the north abutment is thought to be faulty, and should be ignored when comparing the measured deflection with the modelled deflection later in Section 5.2. The variation in measured deflections from the best-fit trendline may be attributable to the precision of the survey equipment used to conduct the test. An automatic level and field rod with 2mm increments was used, and deflections were noted to the nearest millimetre. Also, the test required that turning points be established to move the level closer to the test truck, and some error may have been incurred due to this.

Chapter 4 - Soil - Structure Interaction Models

4.1 Elastic Continuum Methods

4.1.1 Broms Static Equilibrium Solution

A soil-strength-based approach, based on work by Broms, was used to calculate a theoretical ultimate lateral load, P_u , of 312kN that could be applied to the pile P5N before reaching failure of the soil-pile system. This approach was used to estimate a safe lateral load for the pile tests, while trying to maximize soil engagement. In the absence of laboratory or in-situ soil parameter measurements, it was assumed that the soil had an effective soil friction angle of 28 degrees and effective unit weight of 18kN/m³. The effective friction angles are the average of values published in Carter and Bentley (1991) and Peck et al. (1974) for loose sand. The effective unit weight for loose sand was obtained from Lindeburg, (1991). The calculations are shown in Appendix F.

4.1.2 Hetenyi Differential Equation

Two solutions to the Hetenyi fourth order equation for a free-head pile P5N at the Scoudouc Bridge, representing an embedded pile in a soil with an equivalent soil stiffness k_e of 10538kN/m³, are presented in Appendix B. The first solution considered only the deflection of 37mm at groundline to calculate a maximum bending moment of 164.6kNm at 2.5m below the groundline, then simply superimposed the groundline moment of 85.7kNm (155.8kN x 0.55m) to obtain a maximum moment of 250.3kNm. The second solution added the groundline bending moment as a boundary condition, and the equation was re-solved to obtain the maximum moment of 198.8kNm occurring at 2.0m below the

groundline, with a pile head deflection of 54mm. These results are within 25.9% of each other, and demonstrate that the concept of superposition can be applied to obtain a reasonable value of maximum pile bending moment, while solving the equation with an initial boundary condition of applied pile head moment yields an unconservative result.

4.1.3 Poulos and Hull Linear Elastic Solution

Elastic continuum theory, based on Poulos and Hull's work, was used to calculate a pile head deflection of 22mm and maximum moment of 267kNm in pile P5N when a lateral head load of 155.8 kN was applied. An equivalent k_h of 10538kN/m³ was calculated by equating the second moments of area about a datum which represents the $\frac{1}{4}$ wavelength of the assumed pile curvature (ie $L_o=L_c/2$). A critical pile length L_c of 6.13m was calculated. The iterative procedure is outlined in Section 2.2.2.3. The magnitude and variation of k_h along the length of the pile was determined by assuming published values of soil stiffness, then adjusting these and best-fitting the pile to measured deflections and stresses. Autocad™ was used to calculate the second moment of inertia of the profile to obtain the equivalent value of horizontal subgrade modulus for use in the computations of critical pile length. Because the variables for critical length L_c and horizontal subgrade reaction k_h are inter-dependent, iterations are required to converge on the solution. The variation of horizontal subgrade reaction with depth along Pile P5N is displayed graphically in Figure 4.1.

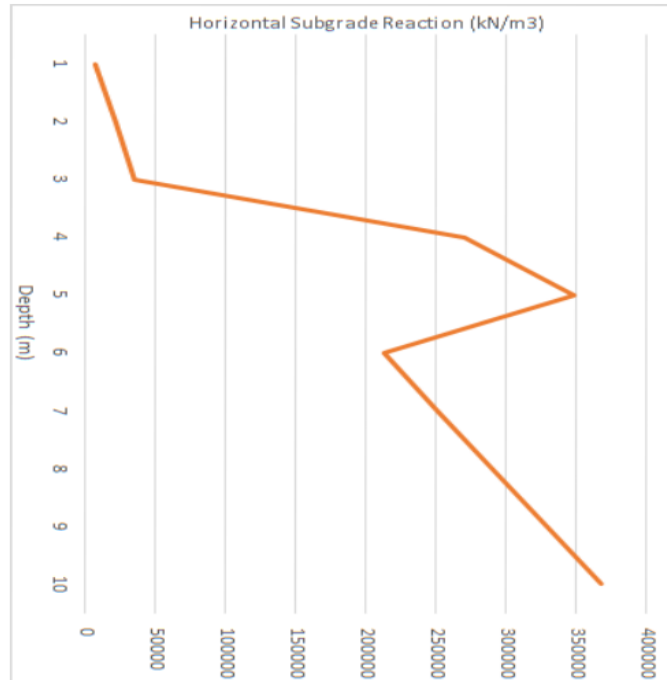


Figure 4.1 Variation of k_h Along Pile P5N.

The Poulos and Hull elastic solution calculations are shown in Appendix G.

4.2 Equivalent Cantilever Methods

4.2.1 Abendroth and Greimann Equivalent Cantilever Solution

An adaptation of continuum theory by Abendroth and Greimann, as it applies to integral abutment bridges, was used to calculate the maximum moment of 367kNm in pile P5N associated with a free-head lateral deflection of 54mm. The critical pile length L_c was calculated to be 6.18m. The equivalent cantilever length was determined to be 4.75m from the point of lateral load application to the fixed base. An equivalent value of k_h was

calculated in the same fashion that was done in Poulos and Hull's solution. The calculations are shown in Appendix H.

4.2.2 2D Pile Modelled as Equivalent Cantilever

A two-dimensional free-standing cantilever model of an idealized P5N pile was created with STAAD.Pro software. A cantilever length of 4.75m to the point of load application was assumed, which represents the cantilever length calculated with Abendroth and Greimann's method. The maximum moment was calculated by setting a free-head lateral pile deflection of 46mm at 0.45m below the pile head, which was inferred from the 54mm head deflection observed in the field. The analysis generated a moment value of 367kNm, and this result was verified with common beam equations.

$$P=3EI\Delta/L_e^3=(3)(205\times 10^3)(293\times 10^6)(46)/(4750)^3=77343\text{N}$$

$$M=PL_e=(77343)(4750)=367\times 10^6\text{Nmm}=367\text{kNm}$$

The STAAD model is shown in Figure 4.2.

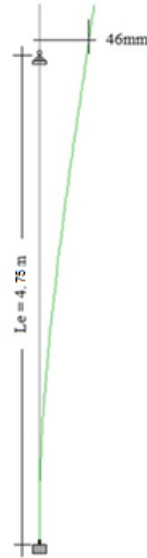


Figure 4.2 2D Pile Modelled as Equivalent Cantilever.

4.2.3 2D Bridge Modelled with Equivalent Cantilever Piles

Engineers often idealize an integral abutment bridge as a two-dimensional frame to calculate anticipated deflections, pile forces and bending moments due to vehicular live loads. The idea is to represent each of the superstructure, abutment and piles with elements that have equivalent mass and stiffness. Fixed connections are defined at the superstructure-abutment and abutment-pile interfaces to represent the rotational fixity that is inherent in an integral abutment bridge. In the case of a 2D bridge modelled with equivalent cantilever piles, the piles have a fixed base, and their length is determined by computational solutions such as Abendroth and Greimman's (1987).

A 2D bridge frame was created in STAAD.Pro, with equivalent cantilevered piles measuring 4.20m below the bottom of the abutment. This length was obtained by subtracting 0.55m, which is the distance from the point of lateral load application to the

bottom of the abutment, from the equivalent cantilever length of 4.75m based on Abendroth and Greimman's theory. One girder, of the bridge's four girders, was used to represent the superstructure, and the equivalent stiffness of 3.5 piles (one quarter of fourteen piles) was assigned to the cantilever. The abutment was represented by a stiff concrete beam element 1.2m high, 3.5m wide, and 5.1m long. Rigid connections were assigned to the girder-abutment and abutment-pile connections. The piers were represented by rollers, with the three translational degrees of freedom restrained, and the three rotational degrees of freedom released. The abutment backfill was represented by linear springs at the top, middle and bottom of the abutment wall to represent the 75mm compression foam. The spring constant was calculated by summing the total spring reaction that is assumed to occur if the compression foam is the maximum specified value of 100kPa over a deflection of 0.0375m, then dividing by four (4) because the model only represents one girder. The interior lateral load sharing factor of 0.587, as defined in the CHBDC CAN S6-14 and calculated as per clause 5.6.4.3, was applied to the test truck to provide the proportionate axle loads. The maximum deck deflection as analyzed by STAAD was 14.9mm, located 26.7m from the north abutment as the truck's front axle was 32m from the north abutment, driving southward. This compares well with the location of measured maximum deck deflection of 26m from the north abutment, as seen in Figure 3.16.

Figure 4.3 shows the idealized STAAD bridge model.

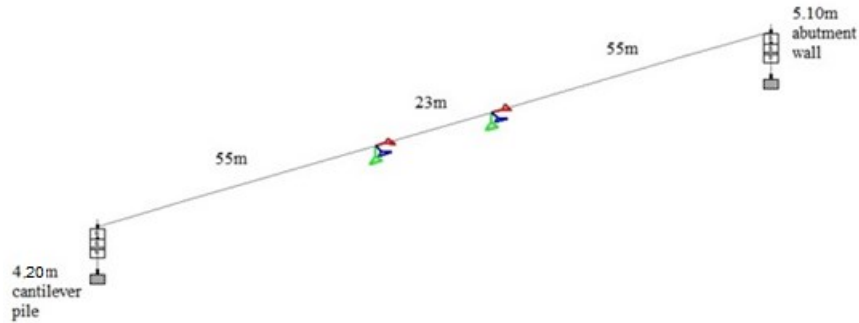


Figure 4.3 Idealized STAAD 2D Frame Bridge Model (Single Girder).

The maximum axial force in the idealized pile due to the vehicular live load was 221.8kN when the front axle was 12m from the north abutment, which coincides with the trailer wheels just embarking onto the bridge. The maximum bending moment in the idealized pile was 237.2kNm when the front axle was 26m from the north abutment. The idealized abutment could be considered stiff enough to distribute the truck load evenly between 3.5 piles, and the corresponding maximum axial load would be 63.2kN, and the maximum moment would be 67.8kNm. The maximum stress in the pile when the front axle is 26m from the abutment, considering a stiff idealized abutment, would be 39.6MPa.

However, upon close investigation of these results, and consideration of the lateral load-sharing methodology of the CHBDC, it was determined that this approach should not be used to distribute the stresses produced by the design truck load to individual piles. The lateral load sharing factor of 0.587, as determined by applying the CHBDC method, was established to estimate girder moment and deflection only. A safe assumption for distribution of the abutment load to the individual piles is that the abutment is much stiffer than the piles, and the load will be shared equally to all 14 piles. This is shown to

be correct when inspecting the results of the 3D bridge model in Section 4.3.3. Therefore, a second 2D idealized bridge frame model was established to represent the stiffness and mass of the entire superstructure, abutment and pile configuration, to estimate the maximum axial force and bending moment in the individual piles. This required that the entire 406.5kN truck be applied to the idealized superstructure.

The maximum axial force in the newly idealized pile, now representing 14 piles, due to the vehicular live load was 361.1kN when the front axle was 12m from the north abutment, which coincides with the trailer wheels just embarking onto the bridge. The maximum bending moment in the idealized pile, now representing 14 piles, was 330.3kNm when the front axle was 26m from the north abutment. Figures 4.4 and 4.5 show the placement of the truck for maximum axial pile force and maximum pile moment, respectively.

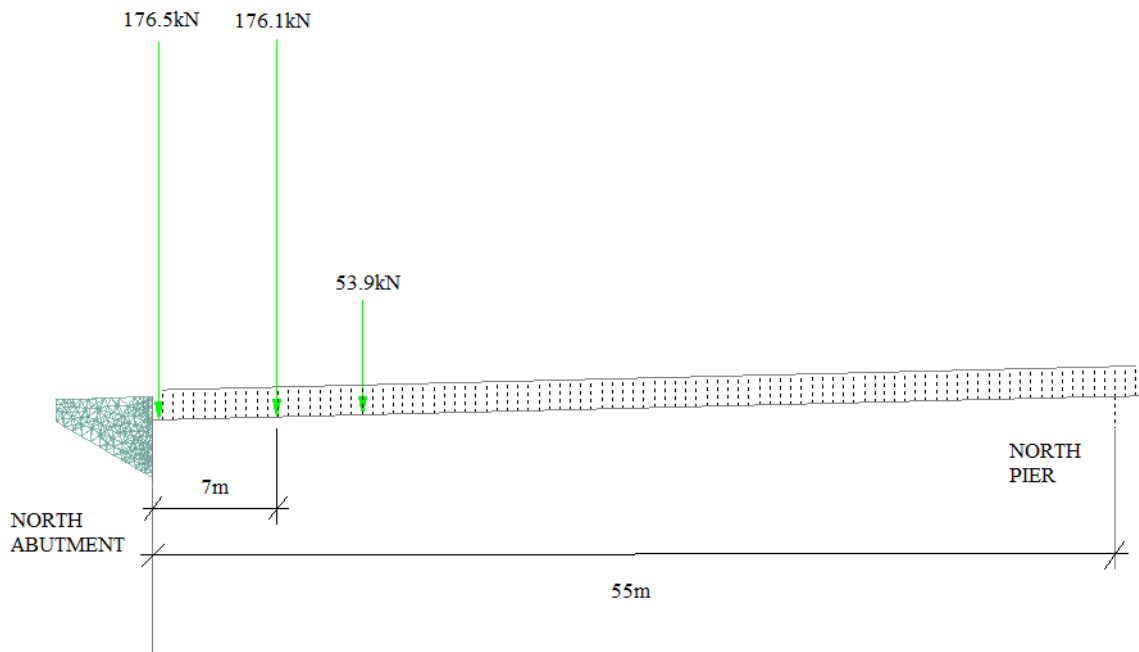


Figure 4.4 Truck Position and Direction for Maximum Pile Axial Force.

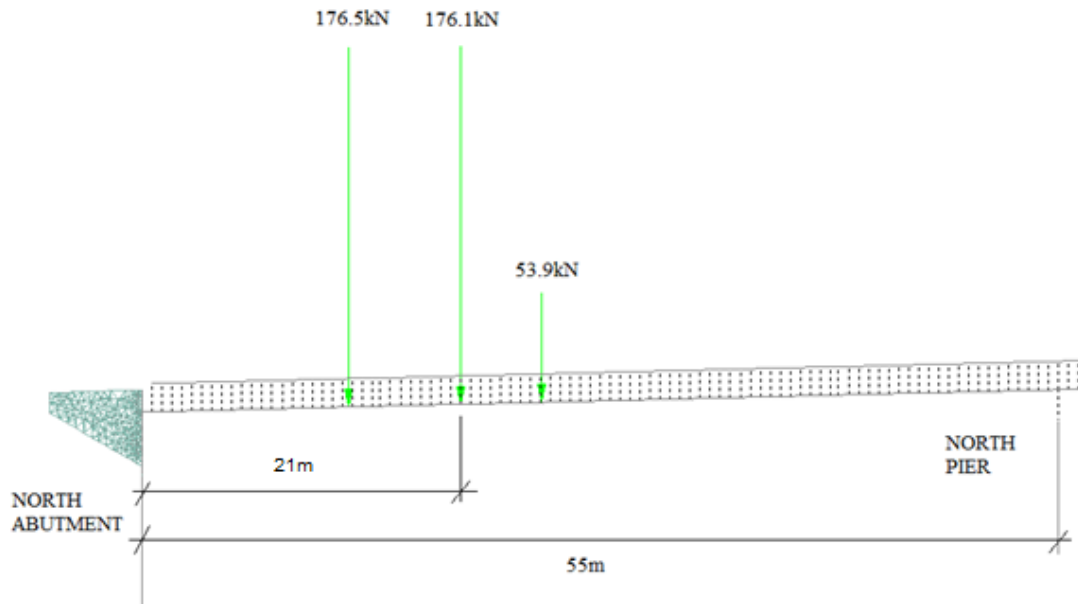


Figure 4.5 Truck Position and Direction for Maximum Pile Bending Moment.

Upon observation of these results and Figures 4.4 and 4.5, one notes that the truck position that creates the maximum pile moment coincides with the truck position that creates the maximum negative girder end moment, and this does not coincide with the truck position that creates the greatest positive “midspan” girder moment and deflection (see Figure 3.15) because of the degree of girder rotational fixity at the abutment. The inferred individual pile maximum axial force and associated stresses are 25.8kN, -4.5MPa and +7.5MPa, respectively. The individual pile maximum bending moment and associated stresses are 23.6kNm, -11.5MPa and +13.5MPa, respectively. These maximum pile stresses are greater than those of -4MPa and +6MPa measured in the field. The difference may be attributable to the fact that upon elastic axial deflection of the piles, the soil underlying the abutment may bear some of the abutment load and restrict

pile strain. The model does not have vertical springs to represent this reaction. Also, the strain gauges had been installed during the construction of the abutment 9 months before the live load test was conducted, and it is possible that these were damaged during subsequent construction activities.

A braking load of 192kN was also applied to the idealized bridge model to represent the braking field test. (The truck drove 60km/h and stopped over a distance of 30m.) The pile head deflection barely registered at 0.014mm.

4.3 Soil Spring Methods

4.3.1 2D Pile Modelled with Discrete Linear Soil Springs

To more accurately represent deflection, shear and moment distribution, as well as general lateral behaviour of an embedded pile, engineers often represent the soil-pile system as a beam element (pile) with discrete springs (soil) along its length. In this case, the stiffnesses of linear springs are determined to best-fit a modelled pile P5N head deflection of 54mm and measured stress of 46MPa, when subjected to a lateral head load of 155.8kN. This is the first step of a process described in Section 6.3, whereby P-Y curves and non-linear soil springs are developed for use in modelling the integral abutment bridge.

A 2D STAAD model of a 10.3m embedded H-pile was created with discrete linear soil springs acting laterally along the length of the pile at 1m increments. Three soil strata exist along its length, and each was represented by linearly increasing soil stiffness. The top layer was 3m deep, and consisted of a pea gravel encased in a steel pipe sleeve. The

next layer was 2m deep, and consisted of a layer of Type A granular backfill. The bottom layer consisted of Type B granular backfill. It is assumed that these soil types are consistent with the Canadian Highway Bridge Design Code CAN CSA S6-14 Soil Groups I and II, respectively, as described in Table 7.4 *Soil Classifications*. Assumed, typical values of horizontal subgrade reaction as published in the Canadian Foundation Engineering Manual 3rd Edition, and the Canadian Highway Bridge Design Code were used. No design information was available for the pea gravel, but the site investigation determined that it was uniform 8mm fractured stone. The published estimates for the variation of horizontal subgrade reaction (n_h) were used as an initial assumption when fitting the model to the field measurements, and these are 2200kN/m³, 24000kN/m³ and 12000kN/m³ for the top, middle and bottom soil layers respectively. It was determined that 2200kN/m³ was too soft at the top of the pile as the head deflection greatly exceeded 54mm, and 4400kN/m³ was used instead. Furthermore, a stiffness reduction factor of 90% was applied to the entire profile to “best-fit” the pile head deflection of 54mm and stress of 42MPa measured on pile P5N in the field.

Table 4.1 shows the variation of linear soil stiffness with depth for pile P5N at a head deflection of 54mm.

Table 4.1 Variation of Soil Stiffness for Pile P5N at a Head Deflection of 54mm.

Penetration (m)	soil	n_h kN/m ³	k_h kN/m ³	A m ²	k kN/m	$k'=0.9k$ kN/m
1	pea gravel	4400	7097	0.31	2200	1980
2	pea gravel	4400	21290	0.31	6600	5940
3	pea gravel	4400	35484	0.31	11000	9900
4	Class A	24000	270968	0.31	84000	75600
5	Class A	24000	348387	0.31	108000	97200
6	Class B	12000	212903	0.31	66000	59400
7	Class B	12000	251613	0.31	78000	70200
8	Class B	12000	290323	0.31	90000	81000
9	Class B	12000	329032	0.31	102000	91800
10	Class B	12000	367742	0.31	114000	102600
10.3	Class B	12000	392903	0.31	121800	109620

The model was subjected to a head load of 155.8kN, which resulted in a head deflection of 54mm, producing a maximum pile moment of 265kNm. The pile exhibited contraflexure (see Figure 4.6), as expected, with the first zero displacement at 4.91m below the pile head, and the second at 9.23m below pile head.

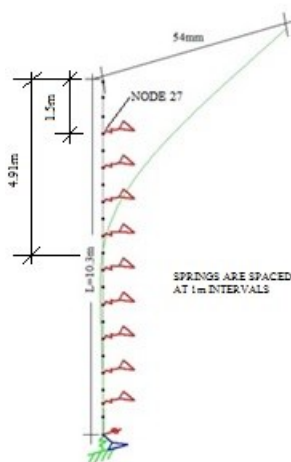


Figure 4.6 Results for 2D Pile Modelled with Discrete Linear Soil Springs.

The significance of the distance of 4.91m is that it represents the depth along the pile below which lateral pile deflections and stresses are negligible. This compares well to the equivalent cantilever length of 4.75m (to the point of load application) determined by using the Abendroth and Greimman method. Considering the load was applied 0.45m below the pile head, the overall length of cantilever pile is 5.20m. The difference between the two methods is 0.29m, or 5.9%, which can be partially attributed to the response of the pile below this depth, as the equivalent cantilever approach has zero deflection, and the 2D model has slight contra-flexure, and as a result has small deflections below this depth.

4.3.2 2D Bridge Modelled with Discrete Linear Soil Springs

The 2D bridge modelled with equivalent cantilever piles, as described in Section 4.2.3, was refined by replacing the equivalent cantilever piles with a soil-pile system consisting of a beam element representing the embedded pile, and linear soil springs representing the soil stiffness. The linear spring stiffnesses to be used in the 2D bridge modelled with discrete linear soil springs were established in Section 4.3.1. The spring modelled soil-pile system will more accurately represent the actual behaviour of the soil-pile system in an integral abutment bridge, and will allow pile deflections and stresses to be observed along the entire length of the pile.

A 2D bridge model was created in STAAD.Pro, and linear soil springs were assigned to pile nodes to represent the soil stiffness. The spring constants were calculated by using published values of n_h from the CFEM and CHBDC. The soil springs at the piles are

linear, and have been assigned spring constants that relate to n_h values of 4400kN/m³, 24000kN/m³ and 12000kN/m³ for the pea gravel, Type A granular and Type B granular soil layers, respectively. The abutment was represented by a stiff concrete beam element 1.2m high, 3.5m wide, and 5.1m long. Rigid connections were assigned to the girder-abutment and abutment-pile connections. The piers were represented by rollers, with the three translational degrees of freedom restrained, and the three rotational degrees of freedom released. The abutment backfill was represented by linear springs at the top, middle and bottom of the abutment wall to represent the 75mm compression foam. The spring constant was calculated by summing the total spring reaction that is assumed to occur if the compression foam is stressed to the maximum specified value of 100kPa over a deflection of 0.0375m, then dividing by four (4) because the model only represents one girder. The interior load sharing factor of 0.587, as defined in the CHBDC CAN S6-14 and calculated as per clause 5.6.4.3, was applied to the test truck to provide the proportionate axle loads. The maximum deck deflection as analyzed by STAAD was 13.6mm, located 26.7m from the north abutment (See Figure 3.16) as the truck's front axle was 32m from the north abutment, driving southward. Figure 4.7 shows the idealized STAAD bridge model.

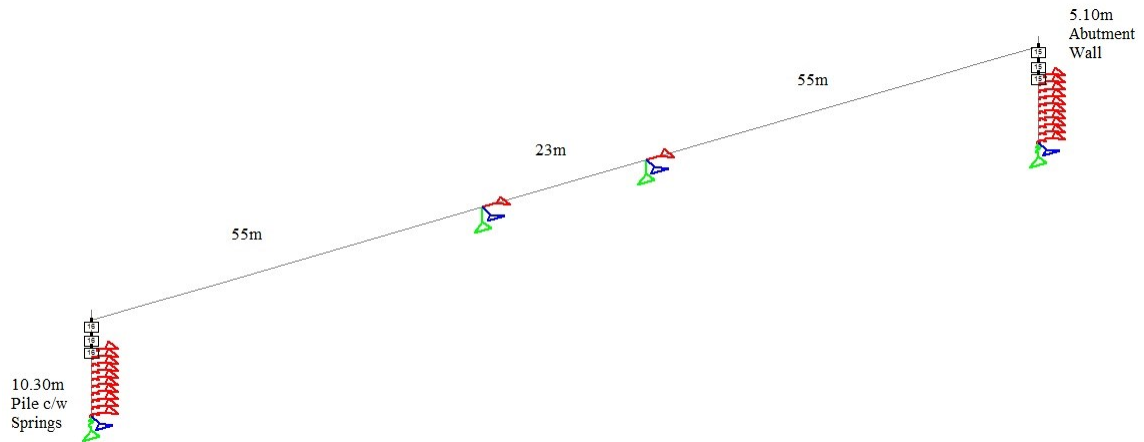


Figure 4.7 2D Frame with Linear Soil Springs.

The maximum axial force in the idealized pile due to the vehicular live load was 214.5kN when the front axle was 12m from the north abutment, and the maximum bending moment in the idealized pile was 223.1kNm when the front axle was 26m from the north abutment, while the truck drove southward. For the same reasons described in Section 4.2.3, it was determined that this approach should not be used to distribute the stresses produced by the design truck load to individual piles. Therefore, a second 2D idealized bridge frame model was established to represent the stiffness and mass of the entire superstructure, abutment and pile configuration, to estimate the maximum axial force and bending moment in the individual piles. This required that the entire 406.5kN truck be applied to the idealized superstructure.

The maximum axial force in the newly idealized pile, now representing 14 piles, due to the vehicular live load driving southward, was 360.2kN when the front axle was 12m from the north abutment (see Figure 4.4), which coincides with the trailer wheels just embarking onto the bridge. The maximum bending moment in the idealized pile, now representing 14 piles, was 327.6kNm when the front axle was 26m from the north

abutment (see Figure 4.5). Upon observation of these results, one notes that the truck position that creates the maximum pile moment coincides with the truck position that creates the maximum negative girder end moment, and this does not coincide with the truck position that creates the greatest positive “midspan” girder moment and deflection because of the degree of girder rotational fixity at the abutment. The inferred individual pile maximum axial force and associated stresses are 25.7kN, -3.9MPa and +6.9MPa, respectively. The individual pile maximum bending moment and associated stresses are 23.4kNm, -11.4MPa and +13.4MPa, respectively. These pile stresses are significantly greater than those of -4MPa and +6MPa measured in the field. The difference may be attributable to the reasons described in Section 4.2.3.

A braking load of 192kN was also applied to the idealized bridge model to represent the braking field test. (The truck drove 60km/h and stopped over a distance of 30m.) The pile deflection barely registered at 0.014mm.

4.3.3 3D Bridge Modelled with Discrete Linear Soil Springs

The idealized 2D Bridge modelled with discrete linear soil springs was refined to represent the entire integral abutment bridge in 3D. This model will more accurately distribute the vehicular loading to the various elements, such that deflections and stresses can be determined throughout the bridge.

A 3D bridge model was created in STAAD.Pro, and linear soil springs were assigned to pile nodes to represent the soil stiffness. The pile spring and backfill spring constants were calculated in the same manner as described in Section 4.3.2. Four composite girders

represent the girders and deck, and these are connected laterally by intermediate diaphragms. The abutment diaphragm and wingwalls were represented by concrete plate elements, 1.2m thick, and rigid connections were assigned to the girder-abutment and abutment-pile connections. An idealized design truck was created to represent the actual test truck used for the Scoudouc bridge live load test (see Section 3.3 Scoudouc Bridge Live Load Test). The maximum deck deflection due to the passing of the idealized design vehicle is 9.7mm on the bridge centerline, and 9.1mm at a 1.8m lateral offset from centreline, and is located 26.9m from the north abutment as the truck drives southward, and the front axle is 32m from the north abutment (see Figure 3.16).

The maximum axial force in the modelled P5N pile due to the vehicular live load was 28.2kN when the front axle was 12m from the north abutment (see Figure 4.4), and the associated bending moment was 14.2kNm. The maximum bending moment in the modelled P5N pile was 30.8Nm when the front axle was 26m from the north abutment (see Figure 4.5), and the associated axial load was 19.5kN. The truck locations which create maximum deck deflection, maximum pile axial force, and maximum bending moment are practically the same as those observed in the 2D models of Sections 4.2.3 and 4.3.2. Upon observation of these results, one notes that the truck position that creates the maximum pile moment coincides with the truck position that creates the maximum negative girder end moment, and this does not coincide with the truck position that creates the greatest positive “midspan” girder moment and deflection because of the degree of girder rotational fixity at the abutment.

A braking load of 192kN was also applied to the idealized bridge model to represent the braking field test. (The truck drove 60km/h and stopped over a distance of 30m.) The pile deflection barely registered at 0.063mm.

A view of the model is shown below in Figure 4.8, and the modelled deck maximum deflection curve is represented in Figure 4.9.

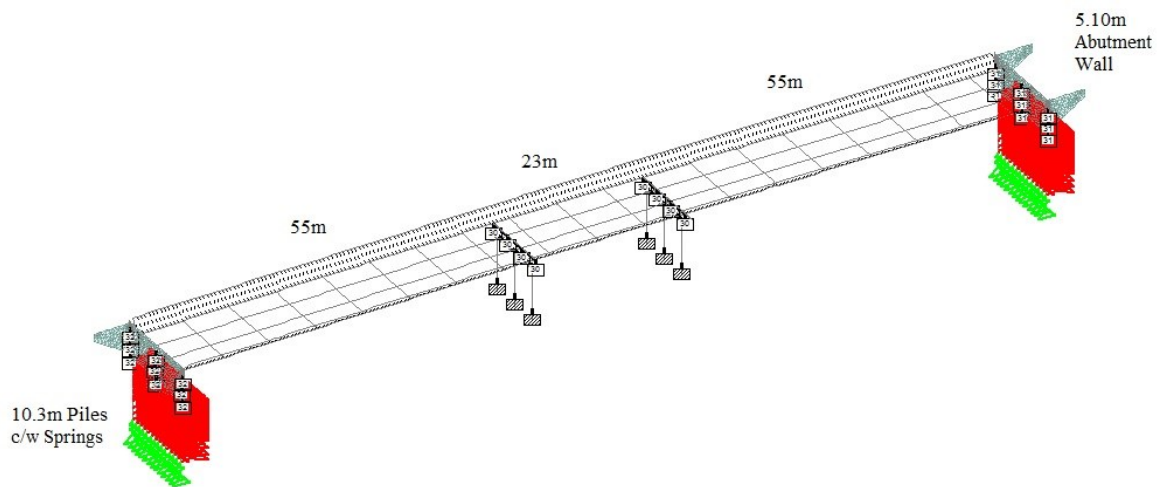


Figure 4.8 3D Bridge Modelled with Discrete Linear Soil Springs.

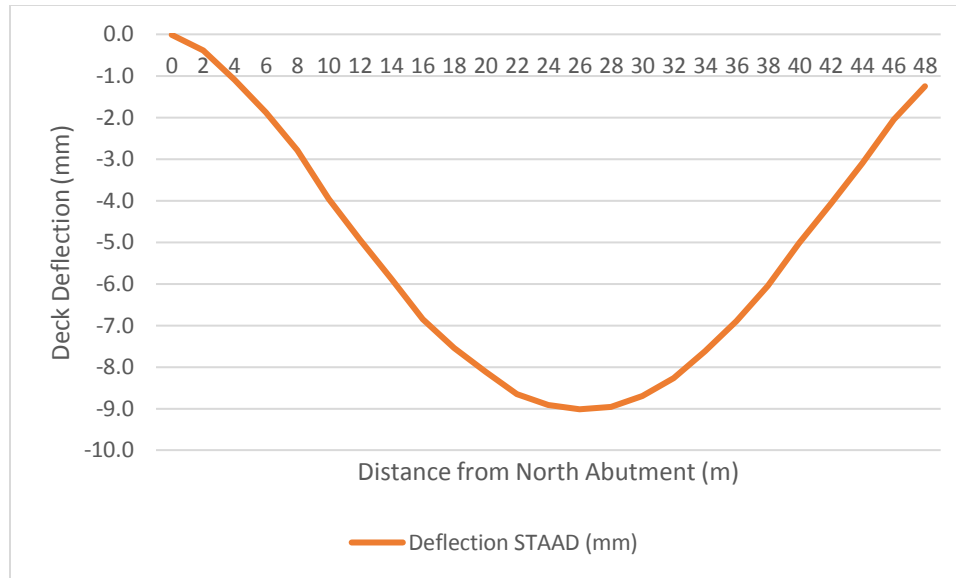


Figure 4.9 Modelled Deck Maximum Deflection Curve.

The curve exhibited in Figure 4.9 represents the vertical deflections of the deck (y-axis) occurring a certain horizontal distance from the north abutment (x-axis) as the STAAD design truck was moved along the deck in 0.6m increments. As noted in the previous sections which presented the results of each bridge analysis, the maximum deck deflections occurred approximately 5m behind the front axle as the design truck drove southward. This is consistent with the fact that the maximum moment should occur at the load closest to the centre of gravity, which is the rear drive wheel. Some slight variances were observed throughout the analyses, and these may be attributable to the fact that the load was moved along the deck in 0.6m increments, and the actual location of maximum moment or deflection may be between the deck nodes to which the truck wheel loads were applied.

The stress in pile P5N caused by the passing of the design truck was a maximum of +17.6MPa (compression) and -15.2MPa (tension) when the truck was driving south and the front axle was 32m from the north abutment. The screenshot of the pile P5N analysis shown in Figure 4.10 presents the state of stress (y pointing south) in pile P5N when the truck is in the position described above.

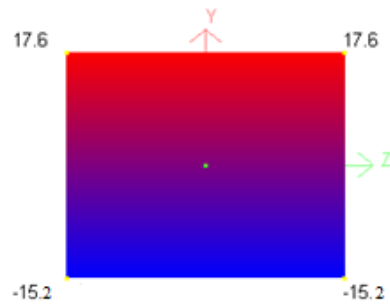


Figure 4.10 Maximum Modelled Live Load Stress in Pile P5N (MPa).

Chapter 5 - Comparison of Results from Linear-Elastic Methods

5.1 Single Pile Analyses

The various elastic methods used to calculate individual free-head pile maximum moment, head deflection, ultimate load and critical length when pile P5N was subjected to a head load of 155.8kN (which represents the maximum load applied in the test) were in general agreement with one another, and matched well with the field measurements.

Table 5.1 summarizes some of these values for each method.

Table 5.1 Summary of Results from Individual Pile Elastic Solutions and Models.

Method of Analysis	Head Load (kN)	Head Deflection (mm)	M_{max} (kNm)	H_u (kN)	L_c (m)
Partial Differentiation ₁ *	n/a	37*	250*	na	na
Partial Differentiation ₂ **	155.8	37**	199**	na	na
Broms	155.8	na	na	312	na
Poulos	155.8	42	267	na	6.1
Abendroth	na	46 [#]	367	na	6.2
2D Cantilever	155.8	54	367	na	na
2D Spring	155.8	54	265	na	na
Field Test	155.8	54	na	na	na

*Free head pile, deflection at ground line.

**Free head pile with deflection and moment at groundline, caused by lateral load applied 0.55m above groundline.

[#]Deflection at point of load application, 0.45m below head.

The first partial differential solution was calculated by assuming a lateral load was applied to the free-head at ground level to obtain a deflection of 37mm, which represents

the ground line deflection of the STAAD model with 54mm of head deflection. Considering there is also an 85kNm moment at ground line in the model (155.8kN x 0.55m), this was superimposed onto the partial differential pile moment value of 165kNm, to obtain 250kNm at a depth below groundline of 2.5m. This was an accurate approximation, but the proper calculation with a boundary condition of $EI d^2y/dx^2=85\text{kNm}$ at $x=0\text{m}$ (groundline) was defined, and the solution solved again to obtain a maximum moment of 199kNm at a depth below groundline of 2.0m. The worksheets for these solutions are shown in Appendix B.

The results of the partial differentiation of the classic beam on elastic subgrade solution provided an unconservative estimate of maximum moment of 199kNm at 2.0m depth when a free-head head deflection of 37mm and moment of 85kNm were imposed at ground-line, and an equivalent horizontal subgrade reaction of 10538kN/m³ was used, which represents an equivalent value of soil stiffness, calculated using Abendroth's second moment of inertia method (see Appendix H). Both the partial differentiation, and the determination of equivalent soil stiffness are tedious calculations, and these are presented in Appendices B and G, respectively, to demonstrate how early beam on elastic subgrade problems were solved. In practice, other means of estimating these values, such as using graphs provided by Broms, tables provided by Poulos and Hull, or equivalent cantilever equations developed by Abendroth, are typically used.

Brom's method of estimating the ultimate lateral pile head load of 312kN provided a value that could be used in the field to establish the maximum test head load. Using a factor of safety of 2, which is common in working stress design of steel and concrete structures, a test pile head load was limited to approximately half of the ultimate pile

head load that was obtained by Broms' method. This method depends on the fact that that the pile acts as a long pile, and that the system would fail due to yielding of the pile, as opposed to failure of the soil. Assumptions of soil properties were made because no test data was available for the soil properties of the "pea gravel" aggregate that was used to backfill the pile encasements. An effective saturated unit weight of 18kN/m³, and an effective friction angle of 28 degrees were used in the calculations. Some of the error in the results can be attributed to the estimation of the ordinate and abscissa values in Brom's tables due to logarithmic scales. The results of the static push test on pile P5N show that 155.8kN of lateral load was required to move the pile head 54mm. The resulting measured strain 1m below the pile head was used to calculate a moment of 79.4kNm, while the single pile STAAD model had a moment of 85.7kNm at the same location. The maximum moment by observing the single pile STAAD model with linear springs was 265kNm, located 3.5m below the pile head.

Poulos and Hull's method of calculating maximum moment and head deflection yielded results that generally agreed with the other structural solutions and models. The critical length L_c of pile was calculated to be 6.13m. The maximum moment as determined by a linear-elastic approach was 267kNm, and the linear-elastic deflection at ground level was found to be 31mm. Considering a rotation of 0.011 radians, this translated to a pile head displacement of 42mm. This deflection is approximately 22% less than the actual field-tested head deflection of 54mm. (Once the non-linear factors for moment and deflection were applied in Section 6.1, the values became 381kNm and 67mm, respectively.) These calculations are presented in Appendix G.

Abendroth and Greimann's elastic method provided a critical pile length L_c of 6.18m, an equivalent cantilever length of 4.75m, and a maximum moment of 367kNm at a pile head displacement of 54mm (which coincides with a lateral pile displacement at the point of load application of 46mm). As for the Poulos and Hull method, an equivalent horizontal subgrade reaction, k_e , was determined using the second moment of inertia method. These values are dependent on the critical cantilever length, and thus the value of equivalent horizontal subgrade reaction was similar to that calculated using Abendroth and Greimann's method. The value of k_e found using the Poulos and Hull value of L_c was 10537kN/m³, while the value of k_e found using the Abendroth value of L_c was 10538kN/m³. These values are in excellent agreement.

A 2D STAAD model of a free-standing cantilever was subjected to a free-head lateral deflection of 46mm at point of load application, which is 0.45m below the pile head. Therefore, the overall length of the cantilever was 5.20m, while the effective length of the cantilever was set at 4.75m, which coincides with the length established using the Abendroth method in Appendix H. The STAAD analysis provided a moment at the base of the cantilever of 367kNm. This value is exactly that calculated with the Abendroth method, and the results were verified by hand, by using elastic beam theory, or $\Delta=PL^3/3EI$. Considering $M=PL$, the formula can be rearranged to be expressed as $\Delta=ML^2/3EI$, which is the formula that was used by Abendroth.

A 2D STAAD model of a 10.3m pile embedded in three soil strata of varying stiffness had a 155.8kN lateral head load applied to the model, and the soil stiffness was adjusted to fit the field measurements of 54mm head deflection and 42MPa stress at 1m below the

pile head. This produced a maximum pile moment of 265kNm at 3.50m below pile head. The pile exhibited contra-flexure, as expected, with the first zero displacement at 4.912m below the pile head, and the second at 9.234m below pile head. A reasonable fit was observed when the soil stiffness was adjusted to 90% of the published n_h values, with a modelled head deflection of 54mm and a modelled stress of 46MPa as compared to the field-measured 42MPa. The lower measured stress could be attributable to slip in the mechanically fastened strain gauge, since the gauge is bolted through the pile flange. Also, the fact that it is through-bolted and not adhered to the face of the pile could result in a strain reading that is closer to the average flange stress, as opposed to extreme fibre stress. Another difference could be the actual pile stiffness, as a product of Young's modulus of elasticity, E , and moment of inertia, I , in comparison to the modelled pile stiffness. Mill certificates for the pile steel were not available at the time of writing; therefore, the actual steel modulus of elasticity is not known. The actual cross-sectional geometry of the pile could also be different from that modelled, thus introducing error.

A quick comparison of the values obtained by the Poulos and Hull, Abendroth and Greimann, and 2D-Spring methods reveals that the first method almost matches the maximum moment found by the 2D Spring method. Contrary to this, the second method over-estimates the benchmark 2D Spring method value by 38%. Also, the maximum moment is conceptualized to occur at a depth below pile head of 5.20m when using the Abendroth and Greimann method, while the 2D Spring method calculates it at a depth of 3.5m below the pile head.

When the test range of pile head forces were applied to the single pile FEM-Winkler model with the linear variation of soil stiffness indicated in Table 4.1, it was observed

that the modelled head deflections exceeded the field-measured head deflections for most of the range. The lateral test head loads of 155.8kN, 144.3kN, 120.3kN, 97.4kN, 73.3kN, 45.8kN and 20.6kN produced model head deflections of 53.9mm, 49.9mm, 41.6mm, 33.7mm, 25.4mm, 15.8mm, and 7.1mm, respectively. This was an indication of soil non-linearity, and would be investigated further (see Section 6.3 for Inference of Non-Linear Soil Springs). Figure 5.1 compares the modelled and field measured head deflections when linear springs are used to predict the pile response.

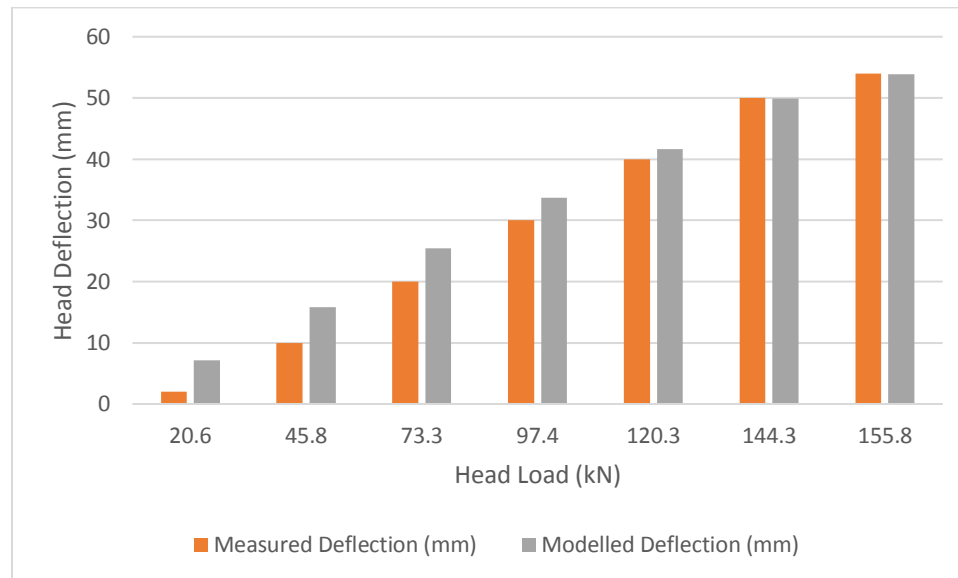


Figure 5.1 Comparison of Modelled and Field-Measured Head Deflections.

Through observation of Figure 5.1, one can see that the model does not accurately predict the pile response at low values of head load. The greatest difference between the measured and modelled head load response is at a head load of 20.6kN, where the predicted head deflection of 7.1mm is 255% greater than the measured 2mm deflection. The soil spring constants used in the model are not stiff enough at low head loads;

however, they predict the pile response to the 144.3kN and 155.8kN heads loads quite accurately. This demonstrates that non-linear springs are required to accurately predict the pile response through the entire range of displacement.

5.2 Bridge Analyses

All three methods which incorporated the results from the single pile analyses to establish idealized bridge models provided reasonable results. A comparison of the 2D Cantilever Frame, 2D Bridge with Linear Soil Springs, 3D Bridge with Linear Soil Springs models, as well as the live load test, is presented in Table 5.2.

Table 5.2 Comparison of Pile and Deck Response for the Linear Bridge Analyses.

Bridge Analyses and Live Load Test	Maximum Deck Deflection (mm)	Position and Direction of Truck (m-S or m-N)	Maximum Pile Axial Force (kN)	Position and Direction of Truck (m-S or m-N)	Maximum Pile Bending Moment (kNm)	Position and Direction of Truck (m-S or m-N)
2D Cantilever Frame	14.9	32.0-S (max defl. at 26.7m)	26.8	12.0-S	23.6	26.0-S
2D Bridge (Linear Soil Springs)	13.6	32.0-S (max defl. at 26.7m)	26.2	12.0-S	23.4	26.0-S
3D Bridge (Linear Soil Springs)	9.1	32.0-S (max defl. at 26.9m)	28.2	12.0-S	30.8	26.0-S
Live Load Test	11	32.0-S (max defl. at 26m)	16.7	n/a	9.5	n/a

Note: Distances are taken from north abutment.

The locations of maximum deck deflection occur very close to the centre of the main 55m span for the 2D and 3D models, and the truck positioning is such that the maximum deflection occurs at the rear driver axle (see Figure 3.16). This agrees with the principle that the maximum deflection should occur when the truck's axle which is closest to the

truck's centre of mass is positioned on the span centre. The maximum pile axial forces in each of the models differ very slightly, and they all occur when the truck entirely embarks on the bridge (see Figure 4.4), with the rear axle at the north abutment (heading southward). This is in agreement with the principle that the maximum shear occurs in the girder when the entire truck is on the span, and the rear axle is just on the end of the deck. The maximum pile bending moments in the 2D models are within 0.2kN of one another, or 0.9%; however, the pile moment provided by the 3D model is greater than the 2D models, at 30.8kNm. The latter represents 131% of the average of the 2D model pile moments. All maximum pile moments occur when the rear drive wheel is 21m from the abutment (see Figure 4.5).

The higher values of maximum deck deflection, axial pile force and pile bending moment in the 2D models can be partly attributed to a higher live load distribution factor. The CHBDC was used to calculate a value of 0.587 for the 2D models, and the 3D model shows that the interior girders are only subjected to 0.472 (or 47.2%) of the truck load. This is a reasonable value considering the wheels of the truck fall between both interior girders, and only a small portion of the load would be transferred laterally to the exterior girders via the intermediate diaphragms. Another reason for greater deck deflections in the 2D models is that they do not consider the stiffness from the concrete barriers.

A graph of the deflection at the northwest end of the deck, measured and modelled, by increment is plotted in Figure 5.2. The 3D linear spring bridge model was used to calculate the deck deflections.

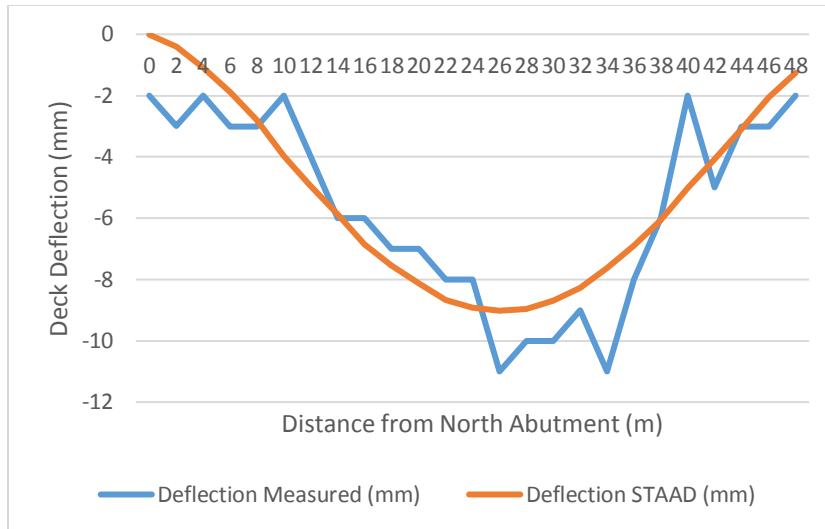


Figure 5.2 Measured and Modelled Bridge Deck Deflection due to Vehicular Loading.

This graph shows that the predicted deflection trend is similar to the measured results, and the maximum values of 9.1mm and 11mm occur at approximately the same location on the bridge (26m from the North abutment). The difference in deflection values can be due to the actual bridge components' stiffnesses being less than what was calculated and modelled, as no material records were available. Also, the live load survey was conducted with a level and rod that was graduated to the nearest 2mm; therefore, some degree of error may have been incurred through the process of measuring deflections.

Chapter 6 - Refinement of Solutions and Models Due to Soil Non-Linearity

6.1 Poulos and Davis Soil Non-Linearity Factors

To account for the nonlinear response of piles under lateral loading conditions, Poulos and Davis (1980) proposed nonlinear solutions by applying yield factors to the linear solutions. The modified ground-line deflection and rotation, are expressed by the following Equations:

$$\rho_{\text{plas}} = \rho_{\text{gelas}} / F_{\rho} \quad (\text{Equation 6.1})$$

$$\phi_{\text{plas}} = \phi_{\text{elas}} F_{\phi} \quad (\text{Equation 6.2})$$

Where ρ_{elas} and ϕ_{elas} are the deflection and the rotation from the elastic solution, and F_{ρ} and F_{ϕ} are yield deflection and rotation factors, respectively. These are functions of the relative eccentricity (ratio of unsupported pile length to embedded pile length) of the load, e/L , the pile flexibility factor, K_R , and the applied load level, which is expressed as a dimensionless ratio H/H_u , where H is the applied load and H_u is the ultimate lateral load capacity of the pile (Poulos and Davis, 1980).

The variable e is defined as the length of pile which is unsupported above the groundline, and is equal to 0.55m, and L is the embedded length of the pile, and equal to 9.3m.

Therefore, the value of e/L is 0.06. The variable K_R is defined as follows:

$$K_R = E_p I_p / E_s L^4 \quad (\text{Equation 6.3})$$

The graphs from which F_ρ and F_ϕ are to be derived are shown in Figures 6.1 and 6.2, respectively. It is worth noting that these graphs are to be used for a soil with uniform secant modulus of elasticity (E_s); however, as the value of L_c was calculated with an equivalent, uniform value of k_h ; therefore, it is felt that these graphs can be used to modify the linear values calculated in Section 4.1.2.

Considering a lateral head load of 155.8kN, and an ultimate head load of 312kN obtained by following Broms' Static Equilibrium Solution, we've obtained a H/H_u ratio of 0.5. By examining Figure 6.1, a value of F_ρ of 0.62 is interpolated. Likewise, by examining Figure 6.2, a value of F_ϕ of 0.70 is interpolated. These values, when applied to the linear elastic values of ground line deflection and rotation of 31mm and 0.011 (Section 4.1.2), yield values of ρ_{plas} and ϕ_{plas} of 50mm and 0.015 radians, respectively. These values translate to a pile head deflection and pile moment of 67mm and 381kNm, respectively.

The estimated value of head deflection of 67mm assuming soil non-linearity exceeds the value of 54mm obtained by assuming linearity by 24%; and, the estimation of maximum moment of 381kNm assuming soil non-linearity is 43% greater than the 267kNm obtained by assuming soil linearity. The value of maximum pile moment of 381kNm agrees closely with the maximum pile moment of 372kNm obtained by using Abendroth and Greimann's method; however, it is 44% greater than the maximum pile moment obtained from the 2D FEM-Winkler model.

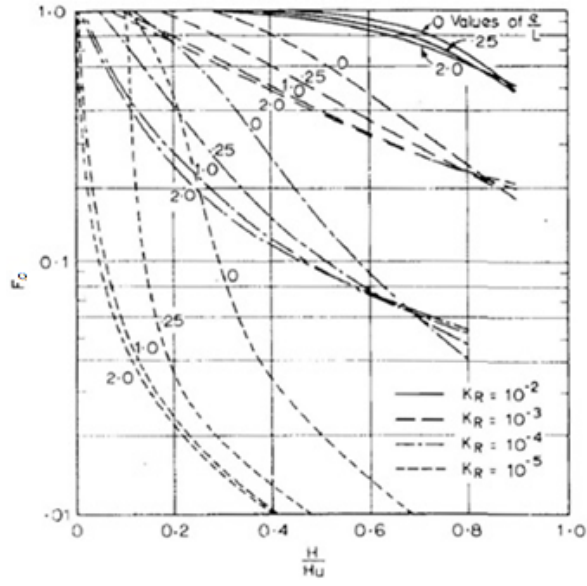


Figure 6.1 Yield-Displacement factor, F_ρ , for Free Head Pile in Soil with Uniform E_s .
(Poulos and Davis, 1980)

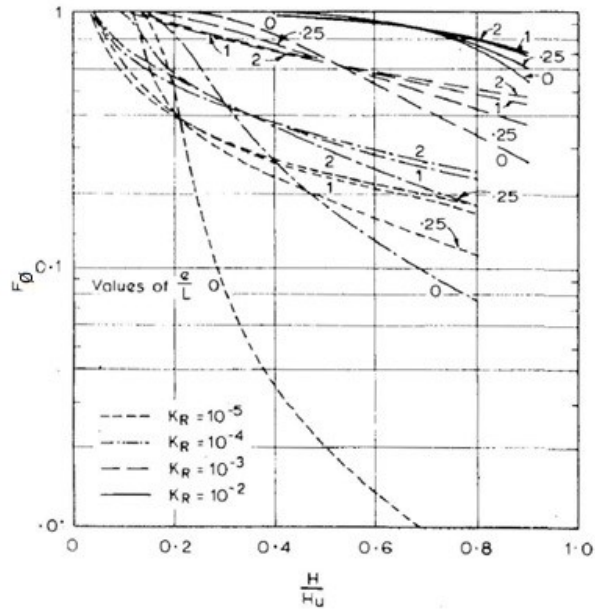


Figure 6.2 Yield-Rotation factor, F_ϕ , for Free Head Pile in Soil with Uniform E_s .
(Poulos and Davis, 1980)

6.2 Non-Linear Composite Backfill Springs

This section presents three methods used to calculate the effective stiffness of non-linear coupled abutment backfill springs, which will better represent the non-linear interaction of the abutment backwall, the compression foam and the granular backfill.

As per the contract plans and specifications, a 75mm thick layer of compression foam was installed along the backside of the abutment wall to reduce backfill pressures at the wall interface. It is a low-density, closed cell, cross-linked foam material with a minimum movement range of 50% compression and 25% tension, and meets the requirements of Table 6.1.

Table 6.1 Compression Foam Specifications. (NBDTI, 2009).

Property	Test	Requirement
Compressive Strength at 50% Deflection	ASTM D-1056	100 kPa Minimum
Tensile Strength	ASTM D 3575-91 Suffix T	400 kPa Minimum
Compression Set at 50% Deflection, 22 Hour Loading, 24 Hour recovery	ASTM D-1056	90% Minimum Recovery
Water Absorption (lbs/ft ² cut surface)	ASTM D-3575 Suffix L	0.05 Maximum

Assuming the compression foam provides the minimum compressive resistance, then it has a spring constant value of 100kPa per 0.0375m, which is equivalent to 2667kN/m per m² of coverage. Considering the surface area of the abutment wall is 5.1mx14.1m, then the total compression foam reaction if depressed to 50% is 191757 kN/m. The heavily reinforced concrete abutment wall is very stiff at 1.2m thick; therefore, it was decided to

represent the foam stiffness with nine discrete springs of 21306kN/m stiffness each, positioned as shown in Figure 6.3.

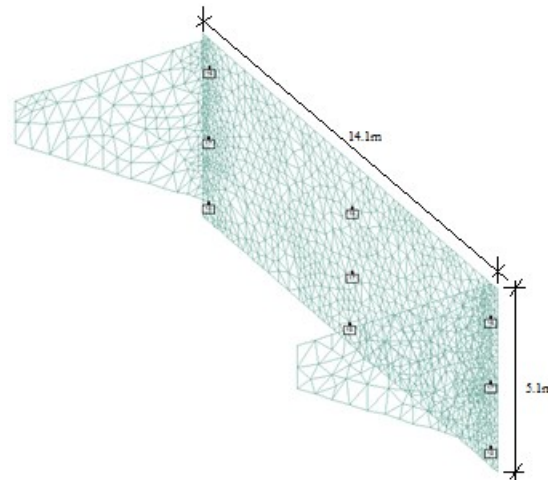


Figure 6.3 Positioning of North Abutment Backfill Springs (South Abutment Similar).

The second part of the coupled system is the stiffness of the backfill soil, and this can be calculated in several ways. Three of these methods are presented in the following sections, and are referred to as Carvajal's Method, Terzaghi's Method #1 and Terzaghi's Method #2. These titles were chosen because of each individual's respective contributions to the determination of the magnitude and variation of soil stiffness with depth, and is only meant to identify the primary theory used in each method. The use of these titles does not imply that these are recognized, published methods, and the use of these titles should be limited to this thesis.

6.2.1 Carvajal's Method

The backfill passive pressure force resisting movement at the abutment varies non-linearly with lateral displacement. It is common practice to represent the non-linear

lateral soil reaction that develops at the wall using a bi-linear spring. The spring stiffness is dependent on both the near-field conditions within a zone of about three times the height of the abutment and far-field conditions beyond this zone, depending on the stiffness of the abutment-embankment system relative to the bridge and the period of the far-field embankment (Carvajal, 2011). Only the near-field characteristics are of interest here for the anticipated soil deflections due to abutment movement caused by thermal, wind and vehicular loading are assumed to be attenuated within short proximity of the bridge, and certainly within three times the abutment height, which is the zone that is defined by Carvajal (2011). Therefore, the soil portion of the composite spring will be represented linearly. For abutment walls taller than 1.7m, the lateral stiffness of integral abutments is dependent on the flexibility of the abutment wall, height of wall, and the mode of deformation (Carvajal, 2011). For these abutments, the near-field lateral stiffness can be approximated as:

$$K_{\text{abut}} = C \cdot w \cdot G_{\text{mob}} \quad (\text{Equation 6.4})$$

where, G_{mob} is the mobilized shear modulus of the bridge embankment in N/mm^2 , and w is the width of the abutment wall in millimetres. G_{mob} may be established using free-field ground response analysis; however, in the absence of this data, a value of G_{mob} as a function of E_{50} (N/mm^2) and an assumed Poisson's Ratio ν of 0.35 for a dense, drained sand (Kulhawey et al., 1983), will be used. The backfill is a Borrow D gravel compacted to 95% Standard Proctor Density, with an assumed equivalent constant E_{50} of 40MPa. Maintaining moment equilibrium about the base of the abutment wall, and assuming a linear distribution of stiffness with depth, which is consistent with Terzaghi (1955) for a

non-cohesive soil, then the maximum E_{50} value at the base of the wall is gradient is 120MPa, and the E_{50} gradient, also known as n_h , is 23.5MPa/m. This means that E_{50} values at 1m, 3m and 4.5m depth will be 23.5MPa, 70.5MPa, and 105.8MPa, respectively. The following well-known formula is used to calculate the corresponding mobilized Shear Modulus values:

$$G_{mob} = E_{50} / (2(1 + \nu)) \quad \text{(Equation 6.5)}$$

The equivalent constant G_{mob} is 14.8MPa, and the corresponding equivalent constant K_{abut} is 229548kN/m. For each depth of 1m, 3m and 4.5m along the abutment wall, the corresponding G_{mob} values are 8.7MPa, 26.1MPa, and 39.2MPa. The value of C varies with the abutment type as shown in Table 6.2.

Table 6.2 Values of C for Different Abutment Types of IABs. (Carvajal, 2011).

Full-height abutment		Stub abutment		Median value
Flexible	Rigid	$h = 2 \text{ m}$	$h = 3 \text{ m}$	
1.26	0.94	0.96	1.16	1.1

Through examination of Table 6.2, a value of C of 1.1 is chosen, which represents the average value for flexible and rigid full-height abutments. Applying this to Equation 5.4, and knowing the abutment wall width is 14.1m, yields abutment spring constants K_{abut} of 8996kN/m, 26987kN/m, and 40532kN/m for each of the three (3) top, middle and bottom springs, respectively.

6.2.2 Terzaghi's Method #1

Alternately to Carvajal's method, a linear distribution of stiffness of $n_h=15686\text{kN/m}^3$ is assumed with depth, which is slightly less than the 18000kN/m^3 published by Terzaghi, (1955), for a non-cohesive, dense soil above groundwater. The value of n_h was obtained by maintaining translational static equilibrium in equating the resultant forces from the equivalent uniform E_{50} and linearly increasing E_{50} , irrespective of the location of the resultant. The resultant spring constants for each of the equivalent uniform E_{50} and linearly increasing E_{50} are 235290kN/m for the entire width of the 14.1m abutment wall. This reduces to three (3) discrete upper springs of 10449kN/m , three intermediate springs of 31349kN/m , and three lower springs of 36574kN/m . This will be referred to as the Terzaghi 1 method.

6.2.3 Terzaghi's Method #2

Another approach, Terzaghi 2, may consider a linear distribution of stiffness of $n_h=23500\text{kN/m}^3$ is assumed with depth, which is slightly greater than the 18000kN/m^3 published by Terzaghi, 1955, for a non-cohesive, dense soil above groundwater. The value of n_h in this case was obtained by maintaining rotational static equilibrium in equating the moments about the base of the abutment wall, considering the location of the resultant forces from the equivalent uniform E_{50} and linearly increasing E_{50} . The resultant spring constant from the linearly increasing E_{50} is 352500kN/m for the entire width of the 14.1m abutment wall. This reduces to three (3) discrete upper springs of 15666kN/m , three intermediate springs of 47000kN/m , and three lower springs of 54833kN/m .

6.2.4 Comparison of Means to Find Effective Backfill Stiffness

The latter method provides a stiffer backfill estimate, and a comparison of the results is provided in Figure 6.4. The lower stiffness results obtained with Carvajal's (2011) method may be because it is empirical in nature, based on the results from large scale abutments testing at University of California Davis (Maroney 1995), and does not account for the actual abutment height. Also, the value of n_h established by the author, assuming rotational static equilibrium between the equivalent uniform E_{50} and linearly increasing E_{50} was calculated about the base of the abutment wall and hence resulted in a much larger abutment wall pressure in the lower portion of the wall. Translational static equilibrium was not maintained in this case, as it was in the second method described above. It is the results of the second method that will be used to calibrate the 3D model of the bridge, as these include the actual abutment wall geometry, and they agree nicely with the backwall stiffness using Carvajal's (2011) equation.

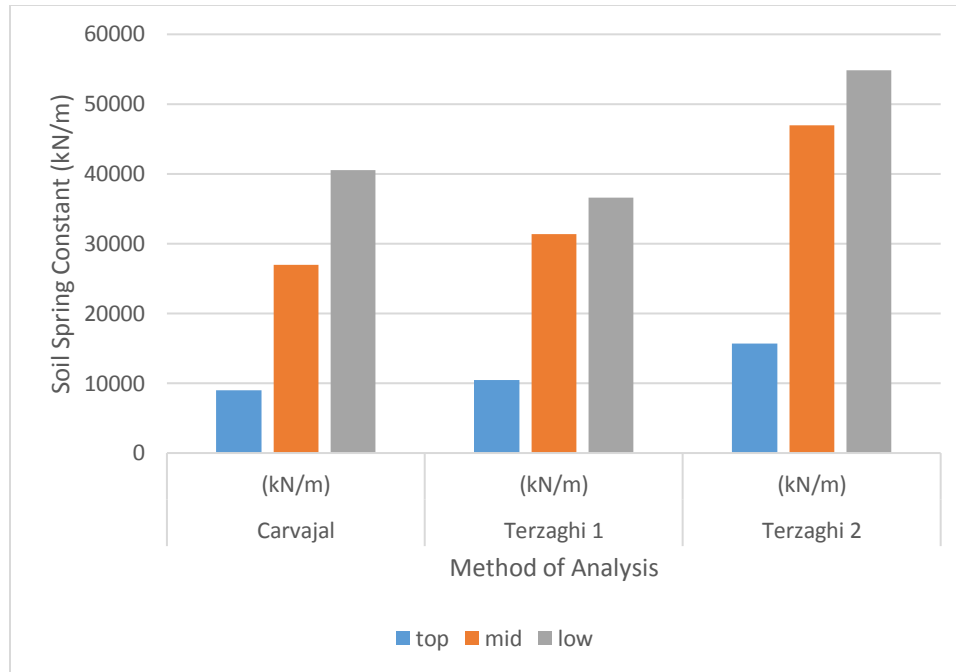


Figure 6.4 Comparison of Carvajal (2011) and (modified) Terzaghi (1955) Backfill Spring Constants.

The backfill soil springs are superimposed onto those representing the compression foam, to provide coupled springs. The coupled springs are arranged in series, and provide a theoretical equivalent spring constant as follows:

$$1/k_{eq}=1/k_1+1/k_2 \quad (\text{Equation 6.6})$$

Therefore, the theoretical equivalent spring constants for the Scoudouc bridge backfill are 7010kN/m, 12685kN/m, and 13463kN/m for the each of the three (3) upper, middle and lower springs, respectively. These values are only be valid for a deflection up to 37.5mm, at which point it is assumed that the compression foam fails and the complete granular backfill stiffness would be engaged. So, non-linear springs were defined in STAAD to reflect the abrupt increase in soil stiffness at an abutment wall deflection of 37.5mm. The STAAD definitions of the upper, intermediate and lower north abutment non-linear

backfill soil springs are listed in Tables 6.3, 6.4 and 6.5, and displayed schematically in Figures 6.5, 6.6, and 6.7, respectively.

Table 6.3 Upper Non-Linear Backfill Soil Spring Definition – North Abutment.

Deflection (m)	Spring Constant (kN/m)
-0.200	10449
-0.038	7010
0.000	0
0.100	0

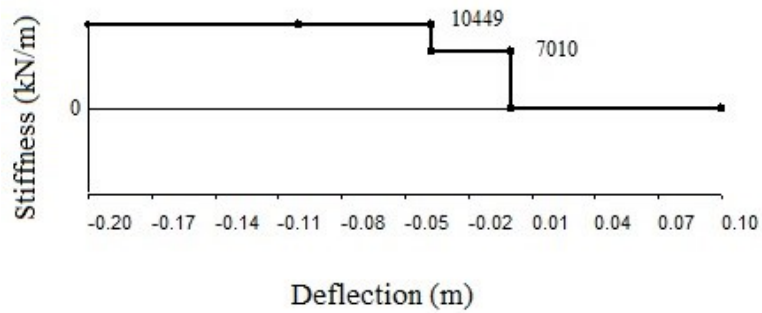


Figure 6.5 Upper Non-Linear Backfill Soil Spring Definition – North Abutment.

Table 6.4 Middle Non-Linear Backfill Soil Spring Definition – North Abutment.

Deflection (m)	Spring Constant (kN/m)
-0.200	31349
-0.038	12685
0.000	0
0.100	0

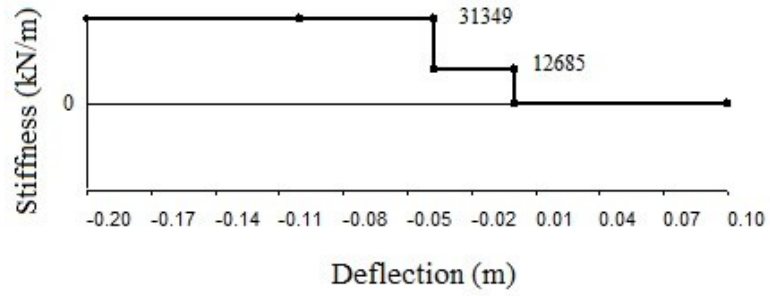


Figure 6.6 Middle Non-Linear Backfill Soil Spring Definition – North Abutment.

Table 6.5 Lower Non-Linear Backfill Soil Spring Definition – North Abutment.

Deflection (m)	Spring Constant (kN/m)
-0.200	36574
-0.038	13463
0.000	0
0.100	0

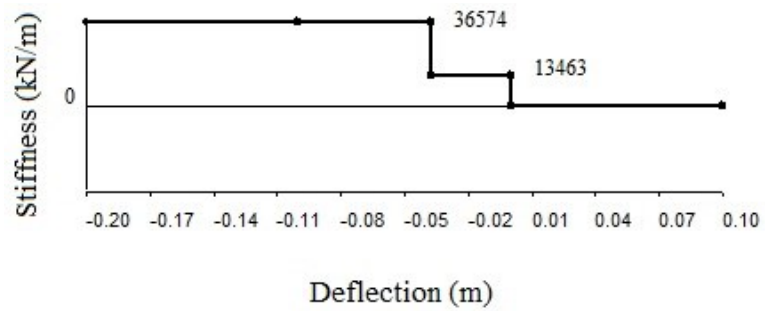


Figure 6.7 Lower Non-Linear Backfill Soil Spring Definition – North Abutment.

The STAAD definitions of the upper, middle and lower south abutment non-linear backfill soil springs are listed in Tables 6.6, 6.7, and 6.8, and displayed schematically in Figures 6.8, 6.9 and 6.10, respectively.

Table 6.6 Upper Non-Linear Backfill Soil Spring Definition – South Abutment.

Deflection (m)	Spring Constant (kN/m)
-0.300	0
0.000	0
0.000	7010
0.038	10449
0.300	10449

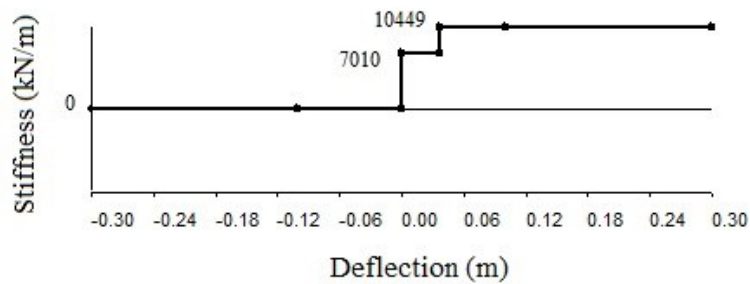


Figure 6.8 Upper Non-Linear Backfill Soil Spring Definition – South Abutment.

Table 6.7 Middle Non-Linear Backfill Soil Spring Definition – South Abutment.

Deflection (m)	Spring Constant (kN/m)
-0.300	0
0.000	0
0.000	12685
0.038	31349
0.300	31349

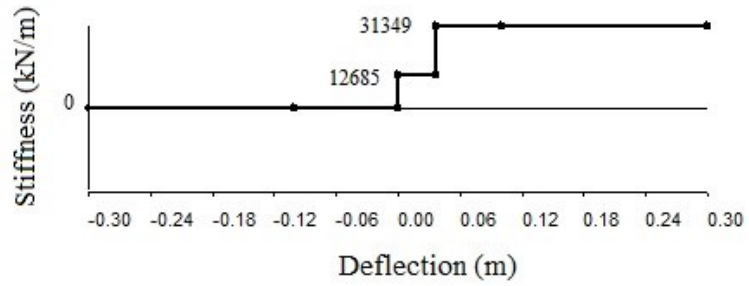


Figure 6.9 Middle Non-Linear Backfill Soil Spring Definition – South Abutment.

Table 6.8 Lower Non-Linear Backfill Soil Spring Definition – South Abutment.

Deflection (m)	Spring Constant (kN/m)
-0.300	0
0.000	0
0.000	13463
0.038	36574
0.300	36574

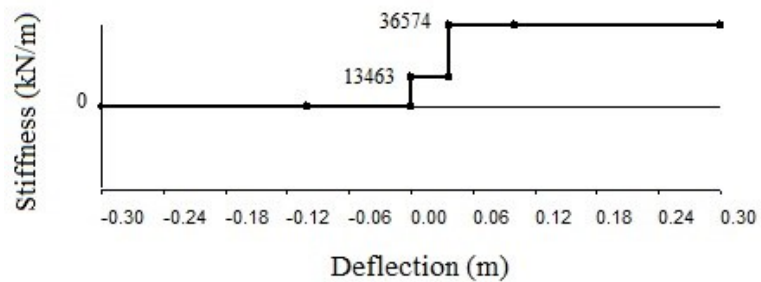


Figure 6.10 Lower Non-Linear Backfill Soil Spring Definition – South Abutment.

6.3 Inference of Non-Linear Soil-Pile Spring Stiffness

6.3.1 Creation of Single Pile Linear FEM-Winkler Models

Two-dimensional models were created in STAAD.Pro to represent the embedded pile with discrete linear soil springs representing the inferred soil stiffness of the soil-pile system at head deflections of 2mm, 10mm, 20mm, 30mm, 40mm, 50mm, and 54mm. The model with head deflection of 40mm had a response that matched very closely the field measurements when the published values of n_h of 4400kN/m³, 24000kN/m³ and 12000kN/m³ were applied to the pea gravel, Type A gravel and Type B gravel, respectively. The spring constants for the remaining models were calculated by applying a stiffness augmentation or reduction factor to this baseline model, as described in section 4.3.1. Table 6.9 shows the “best-fit” stiffness variation for each of the seven FEM-Winkler pile models representing the field-measured 2mm, 10mm, 20mm, 30mm, 40mm, 50mm, and 54mm of head deflection.

Table 6.9 Soil Stiffness Variation for FEM-Winkler Single Pile Models.

Depth (m)	2mm k'=10k (kN/m)	10mm k'=2.5k (kN/m)	20mm k'=1.5k (kN/m)	30mm k'=1.15k (kN/m)	40mm k'=1.0k (kN/m)	50mm k'=0.9k (kN/m)	54mm k'=0.9k (kN/m)
0.5	22000	5500	3300	2530	2200	1980	1980
1.5	66000	16500	9900	7590	6600	5940	5940
2.5	110000	27500	16500	12650	11000	9900	9900
3.5	840000	210000	126000	96600	84000	75600	75600
4.5	1080000	270000	162000	124200	108000	97200	97200

Depth	2mm k'=10k	10mm k'=2.5k	20mm k'=1.5k	30mm k'=1.15k	40mm k'=1.0k	50mm k'=0.9k	54mm k'=0.9k
5.5	660000	165000	99000	75900	66000	59400	59400
6.5	780000	195000	117000	89700	78000	70200	70200
7.5	900000	225000	135000	103500	90000	81000	81000
8.5	1020000	255000	153000	117300	102000	91800	91800
9.3	1140000	285000	171000	131100	114000	102600	102600

Table 6.10 shows the response of the field-tested P5N pile, and that of the linear STAAD models, for varying head loads.

Table 6.10 Response of P5N During Lateral Load Test and Single Pile Linear Modelling.

Load (kN)	Field Deflection (mm)	STAAD Deflection (mm)	Field Stress (MPa)	STAAD Stress (MPa)	Ratio Measured Predicted
20.6	2	2.2	4.3	6	0.72
45.8	10	9.8	10.7	13.5	0.79
73.3	20	19.8	18.3	21.6	0.85
97.4	30	29.9	25.3	28.7	0.88
120.3	40	39.5	32.1	35.4	0.91
144.3	50	49.9	39.1	42.5	0.92
155.8	54	53.9	41.9	45.9	0.91

Through comparison of the field and modelled stresses of Table 6.10, it is shown that the modelled head deflections and pile stresses when using linear soil springs closely mimic those measured in the field. The ratio of measured to predicted stresses ranges from a low of 0.72 for a head load of 20.6kN, to a high of 0.92 for a head load of 50mm. The error range for head deflection is 0.2% at a measured head deflection of 54mm, and 10% at a

measured head deflection of 2mm. This difference in value could be attributable to the transit and ruler only being precise to the nearest millimeter. The error range for pile stress is 12% at a measured head deflection of 54mm, and 43% at a measured head deflection of 2mm. This variance of stress could be due to the deflection measuring apparatus, as mentioned earlier, and possible slippage of the mechanically-fastened strain gauges. Another source of error is the fact that the strain gauges are bolted through the flanges, and would only measure true extreme fibre strain if the nuts were torqued enough to result in a friction connection as opposed to a bearing connection.

6.3.2 Establishment of P-Y Curves for Pile P5N

Seven independent single-pile FEM-Winkler models with linear soil springs were created to represent each of 2mm, 10mm, 20mm, 30mm, 40mm, 50mm, and 54mm head displacements. Soil stiffness was manipulated within the confines of published theories on the variation of horizontal subgrade reaction within a cohesionless soil (ie linearly increasing with depth), and the response of the best-fit soil-pile systems were noted. The values of soil displacement and reaction at each spring location, for each model described above, were used to create P-Y curves (see Section 2.2.2.2 for a description of the P-Y method).

6.3.3 Definition of Non-Linear Soil Springs

The curves were then used to define non-linear soil springs which behaved as the independent linear springs did through the range of soil-pile deflection experienced

during the pile lateral load test. One P-Y curve was created for each of the ten springs along the length of the pile, and that for the top spring (node 27) is shown in Figure 6.11.

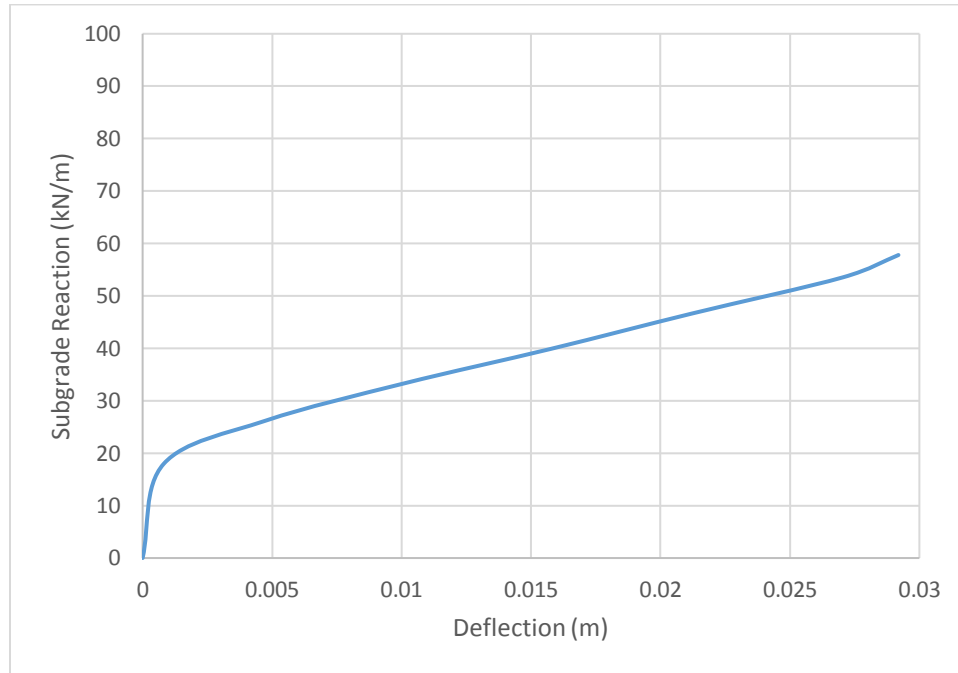


Figure 6.11 P-Y Curve for Top Spring at Node 27.

The non-linear spring for Node 27, located 1.5m below the pile head and 0.5m below the groundline (see Figure 4.6 for location on FEM-Winkler model), is defined by the P-Y curve above and is shown in Table 6.11 and Figure 6.12.

Table 6.11 Variation of Stiffness with Deflection for Spring at Node 27.

Deflection (m)	Spring Constant (kN/m)
-0.23000	1981
-0.0292	1981
-0.0270	1185
-0.0212	1238
-0.0158	1162
-0.0101	1328
-0.0048	2088
-0.0008	22011
0.0000	22011
0.0000	22011
0.0008	2088
0.0048	1328
0.0101	1162
0.0158	1238
0.0212	1185
0.0270	1981
0.0292	1981
0.1600	1981

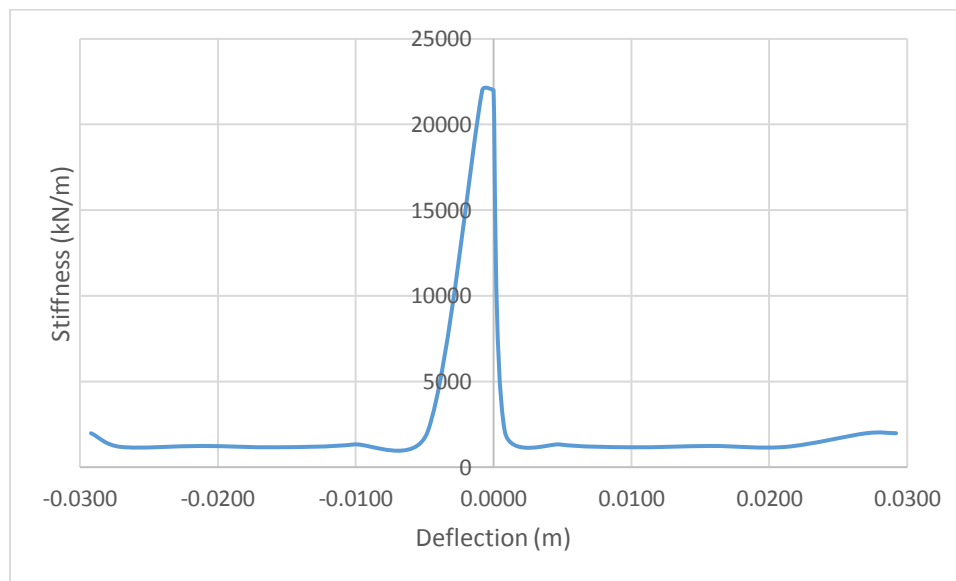


Figure 6.12 Graphic Representation of Non-Linear Soil Spring for Node 27.

A spreadsheet which shows the development of all the P-Y curves is located in Appendix I.

The 2D single pile model in Figure 4.6 was refined to include the non-linear springs that were developed for each node. The pile responded closely to the predicted values of head deflection and pile stress through the range of lateral head loads. A comparison of single pile response for the field test, the model with linear soil springs, and the model with non-linear soil springs is presented in Table 6.12.

Table 6.12 Comparison of Single Pile Responses.

Head Load (kN)	Measured Field Deflection (mm)	Predicted Deflection (Linear Model) (mm)	Predicted Deflection (Non-Linear Model) (mm)	Measured Field Stress (MPa)	Predicted Stress (Linear Model) (MPa)	Predicted Stress (Non-Linear Model) (MPa)
20.6	2	2.2	2.2	4.3	6	5.5
45.8	10	9.8	9.6	10.7	13.5	12.2
73.3	20	19.8	19.5	18.3	21.6	19.6
97.4	30	29.9	29.5	25.3	28.7	26.1
120.3	40	39.5	39	32.1	35.4	32.2
144.3	50	49.9	49.1	39.1	42.5	38.6
155.8	54	53.9	53.2	41.9	45.9	41.7

Through observation of Table 6.12, it is shown that the modelled head deflections and pile stresses when using non-linear soil springs closely mimic those measured in the field. The predicted deflections from the linear spring model are closer to the field-measured values; however, the goal is to develop one set of springs that can predict the pile response over a range of head loads, and the non-linear springs can provide that. Also, the non-linear spring provides more accurate pile stress results. The error range for head deflection is 1.5% at a measured head deflection of 54mm, and 10% at a measured head

deflection of 2mm. This variation in deflection value could be attributable to the transit and ruler only being precise to the nearest millimeter. The error range for pile stress is 2% at a measured head deflection of 54mm, and 39% at a measured head deflection of 2mm. This stress error could be due to the deflection measuring apparatus, as mentioned earlier, and possible slippage of the mechanically-fastened strain gauges. Another source of error is the fact that the strain gauges are bolted through the flanges, and would only measure true extreme fibre strain if the nuts were torqued enough to result in a friction connection as opposed to a bearing connection.

6.4 Calibration of Bridge Model with Non-Linear Soil Springs

The 3D model with linear soil springs was updated to incorporate non-linear soil springs, such that a more accurate bridge response could be predicted. The bridge model was calibrated by replacing the linear soil springs representing the soil stiffness behind the abutment and along the length of the piles with non-linear soil springs. The non-linear backfill and pile spring constants were obtained by the methods described in Sections 6.2 and 6.3, respectively. The bridge was represented by the same beam and plate elements described in Section 4.3.3.

The maximum deck deflection due to the passing of the idealized test vehicle was 9.6mm along the bridge centerline, and 8.9mm at a 1.8m lateral offset from this point, and was located 26.9 from the north abutment as the truck drives southward and the front axle is 32m from the north abutment (see Figure 3.16 for reference of truck positioning).

The maximum axial force in the modelled P5N pile due to the vehicular live load was 28.1kN when the front axle was 12m from the north abutment (see Figure 4.4), and the associated bending moment was 13.6kNm. The maximum bending moment in the idealized pile was 29.2 kNm when the front axle was 26m from the north abutment heading south (see Figure 4.5), and the associated axial load was 18.7kN. Upon observation of these results, one notes that the truck position that creates the maximum pile moment coincides with the truck position that creates the maximum negative girder end moment, and this does not coincide with the truck position that creates the greatest positive “midspan” girder moment and deflection because of the degree of girder rotational fixity at the abutment.

A braking load of 192kN was also applied to the idealized bridge model to represent the braking field test. (The truck drove 60km/h and stopped over a distance of 30m.) The pile deflection barely registered at 0.051mm.

A picture of the model is shown below in Figure 6.13.

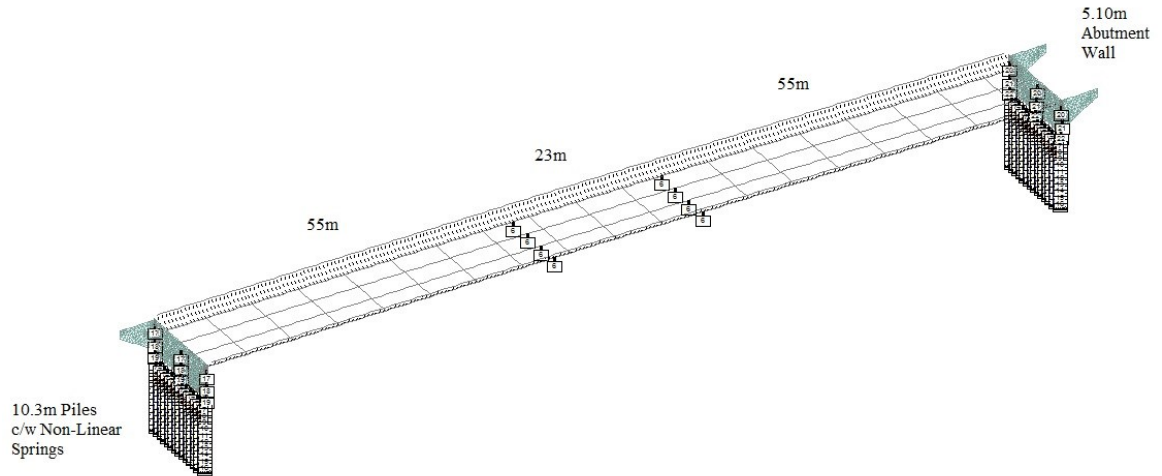


Figure 6.13 3D Bridge Model with Non-Linear Soil Springs.

The stress in pile P5N caused by the passing of the virtual test truck was a maximum of +16.8MPa (compression) and -14.5MPa (tension) when the truck was driving south and the front axle was 32m from the north abutment. The screenshot of the model analysis shown in Figure 6.14 presents the state of stress (y pointing south) in pile P5N when the truck is in the position described above.

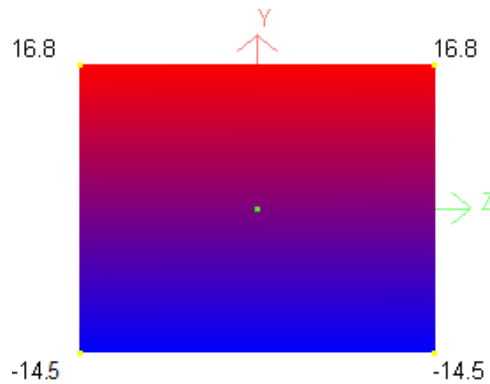


Figure 6.14 Maximum Modelled Live Load Stress in Pile P5N (MPa).

A comparison of the results of the linear bridge models and non-linear bridge model for maximum deck deflection, pile moment and axial load shows that they are in agreement.

Table 6.13 summarizes the results.

Table 6.13 Summary of Results from Bridge Models with Linear and Non-Linear Soil Springs.

Bridge Analyses and Live Load Test	Maximum Deck Deflection (mm)	Position and Direction of Truck (m-S or m-N)	Maximum Pile Axial Force (kN)	Position and Direction of Truck (m-S or m-N)	Maximum Pile Bending Moment (kNm)	Position and Direction of Truck (m-S or m-N)
2D Cantilever Frame	14.9	32.0-S (max defl. at 26.7m)	25.8	12.0-S	23.6	26.0-S
2D Bridge (Linear Soil Springs)	13.6	32.0-S (max defl. at 26.7m)	25.7	12.0-S	23.4	26.0-S
3D Bridge (Linear Soil Springs)	9.1	32.0-S (max defl. at 26.9m)	28.2	12.0-S	30.8	26.0-S
3D FEM Winkler (Non-Linear Soil Springs)	8.9	32.0-S (max defl. at 26.9m)	28.1	12.0-S	29.2	26.0-S
Live Load Test	11	32.0-S (max defl. at 26m)	16.7	n/a	9.5	n/a

*Distances were taken from North Abutment.

A quick review of table 6.13 reveals that the difference in response between the 3D bridge models with linear and non-linear soil springs is negligible. The maximum deck deflections of 9.1mm and 8.9mm, respectively, are within 2.2% of one another. The maximum pile axial forces of 28.2kN and 28.1kN, respectively, are within 0.4% of each

other, and the maximum pile bending moments of 30.8kNm and 29.2kNm, respectively, are within 5.5% of one another.

Chapter 7 - Discussion

A recommended approach to the design of piles supporting an IAB is presented, including a method to define the non-linear soil spring stiffness for use in the FEM-Winkler method. The procedure begins with a simple lateral load test performed on a single pile, followed by structural modelling with discrete uncoupled linear soil springs to mimic the pile response at various head deflection increments, followed by the development of P-Y curves from the nodal displacements and reactions, and ends with the definition of non-linear spring stiffness constants to be used in the FEM-Winkler modelling of the bridge.

7.1 Conceptual IAB Design

Before the above-noted procedure can be implemented, the first typical step in the process of IAB design involves the development of a conceptual bridge design. Factors such as length of bridge, skew of bridge, serviceability of bridge, regional seismicity and site geology are important considerations. Of these, the most important in the design considerations of IABs is the site geology. As per the description of IABs provided in the Introduction, these bridge types rely on the flexibility of the soil-pile system, while at the same time requiring lateral support from the same system. One must first estimate the pile depth to fixity at each support, which is typically defined as that point along the length of the pile below which the lateral deflection does not exceed 5% of the maximum lateral deflection of the pile embedded in soil. If fixity is not achieved, then the pile will behave as a short pile and will essentially rock about its tip when subjected to the cyclic loading of an IAB foundation. To estimate the depth to fixity, one could use a numerical

solution such as that of Abendroth and Greimman (1987) to obtain the equivalent cantilever length of the pile. The inputs for this process include the pile stiffness and the soil stiffness. The latter is often described by an estimate of the horizontal subgrade reaction, k_h , which may either be provided by the project's geotechnical engineer, or can be estimated by referring to published documents such as the Canadian Foundation Engineering Manual, or the Canadian Highway Bridge Design Code. It is commonly assumed that cohesionless soils have k_h values that vary linearly with depth, while cohesive soils have uniform k_h values. This is because the k_h is governed by the effective vertical pressure in the cohesionless soil, while the k_h value in cohesive soils is dependent primarily on the undrained shear strength, which is not a function of depth. Upon reviewing the site's borehole logs, one can determine whether an equivalent value of k_h must be calculated due to significant variation of soil stiffness with depth. The borehole logs will also show if the pile can be driven into the natural ground, or if the site must be modified to ensure pile fixity can be achieved (such as at Scoudouc).

Once it has been determined that an IAB is feasible for the site, with considerations such as maximum length and skew angle, the general arrangement of the IAB can be finalized. At this point, a 2D model of the bridge can be developed, including piles represented by an equivalent cantilever length. The results of this analysis will provide estimates of the stresses in the piles due to vehicular, wind, seismic and thermal loading. The bridge deck, abutment diaphragm and piles are modelled as a frame, representing the mass and stiffness of each component, to form an idealized bridge system.

The 2D model can be further refined during the design process to represent a 3D bridge model with the soil-pile system incorporated as beam elements with discrete linear

springs. The same values of k_h that were used as input in the Abendroth or Poulos solutions can be used to calculate the spring constants at varying depth. This model refinement will yield more accurate and representative results of stress and displacement; however, there is uncertainty in the value of k_h , and this will introduce error in the modelling.

7.2 Lateral Pile Load Test

It is for this reason that some bridge engineers, including this author, recommend that a pile lateral load test be performed to validate preliminary assumptions of soil stiffness, and that the information gathered be used to define non-linear soil spring stiffness constants. The in-situ lateral load test and subsequent analyses described in this thesis are a practical and economical approach to measuring the soil-pile system stiffness. The information gathered can be used to predict the pile response due to vehicular loading of integral abutment bridges, without having to conduct extensive and costly lateral pile load tests, such as those contained in The American Society for Testing and Materials standard D3966/D3966M-07 (2013) *Standard Test Methods for Deep Foundations Under Lateral Load*, as described in Chapter 2. Though these tests provide valuable information regarding the response of laterally-loaded piles, they are not often conducted in practice due to their complexity, time requirements and elevated costs. Furthermore, it is difficult to establish production pile site conditions at a different location due to geology and other site specific characteristics.

As an alternative, a simplified in-situ lateral load pile test for IAB's whose piles are encased in sleeves that are infilled with loose soil is recommended. The results will provide design engineers with a good estimate of a production pile/soil system stiffness such that preliminary SSI models may be calibrated to more accurately predict the constructed IAB's behaviour.

The following is a summary of the steps required to conduct the lateral load pile test, develop P-Y curves, and define non-linear soil springs for piles in integral abutment bridges:

Step 1: Gather the required instrumentation and equipment, including a transit, graduated ruler, 20-ton hydraulic jack complete with dial gauge, jacking beam assembly and strain measuring device such as a PDA.

Step 2: Install the jacking beam between the piles located adjacent to the test pile (see Figure 7.1), ensuring all components are secure. Install the jack horizontally, between the jacking beam and the test pile. Install two strain gauges as far down from the pile head as practically and safely as possible (typically 1.0-1.5m).

Step 3: Measure the horizontal distance between the piles, the vertical distance from the pile head to the point of applied load, the vertical distance from the pile head to the top of the infill soil, and the vertical distance from the point of applied load to the strain gauges.

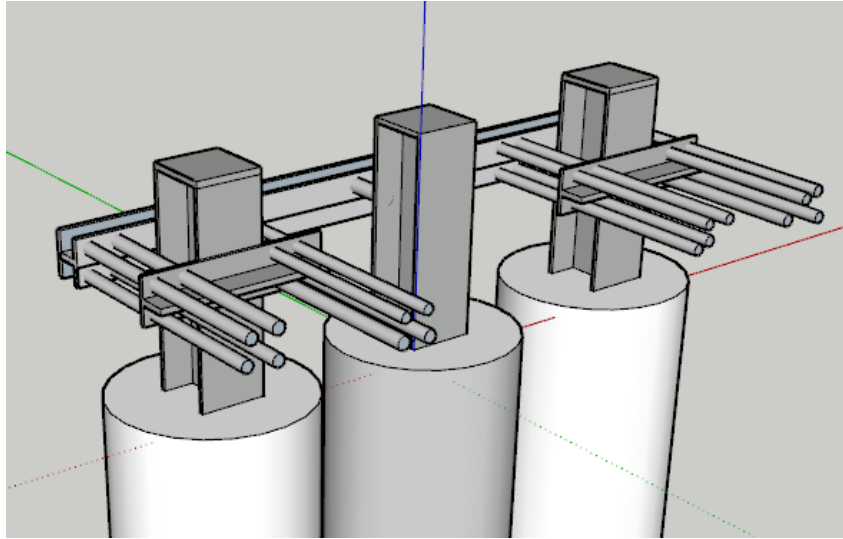


Figure 7.1 Production Pile Lateral Load Test Set-Up.

Step 4: Calculate the ultimate lateral pile head load by Brom's method. Divide this value by two and use it as the maximum lateral load to be applied to the test pile.

Step 5: Slowly apply the jacking load and stop to measure the head deflection, the lateral force and the strain in the pile. Perform this task in two millimeter increments, and record all values, up to a head load of approximately $0.5H_u$.

Step 6: Slowly reduce the pressure on the jack and record the same information in deflection decrements of 4-6mm to obtain a trace of residual strain.

Step 7: Once the load is off the test pile, measure the residual strain at the no-load condition.

7.3 Development of P-Y Curves

With the results of the static push test, one can “best-fit” the pile within a soil whose stiffness is represented by a series of discrete, uncoupled linear soil springs to re-create the field response of pile head displacement and pile bending stress, when subjected to a known lateral head load. The value of k_h is to be adjusted with depth, according to soil type, for each of the separate models to reach agreement with the test results. Effort should be made to ensure head displacement values are modelled to within 1mm of field measurements, while pile bending stresses should be modelled to within 3MPa of field measurements. The soil displacement and associated reaction can be obtained from each node to which is attached a spring, on each model. Then, for a given node on each model, the values of displacement (Y) and reaction (P) are combined to create a node-specific P-Y curve.

A non-linear soil spring can be derived from each P-Y curve by assigning the change in reaction to the respective deflection range, and dividing the former by the latter to obtain the tangential soil stiffness. These stiffness values are then assigned to the deflection range in the structural modelling software (STAAD.Pro in this case) to create non-linear soil springs.

These non-linear soil springs can either be incorporated in the 2D frame model to replace the linear soil springs, or a 3D bridge model can be created, and incorporate the non-linear soil springs, to more accurately represent the overall bridge behaviour.

Here is a summary of the steps to follow once the push test is complete:

Step 1: Establish FEM-Winkler models to represent each of the 2mm, 5mm, 10mm, 20mm, 30mm, etc. head displacements. Begin with published values of k_h for each respective soil type in the profile to calculate linear soil springs at 1m intervals along the pile, and adjust as needed to obtain the desired head deflection and pile curvature for the applied head load. Ensure pile stress is matched to within 3MPa, and head deflection is within 1mm.

Step 2: Obtain the modelled soil-pile deflection and reaction at each linear spring node, and tabulate these. For each node, use the deflection and reaction values from each of the models to create a P-Y curve. Each node must have a uniquely representative P-Y curve.

Step 3: Use the P-Y curve for each node to define a non-linear spring. STAAD.Pro uses the tangential values of stiffness on the P-Y curve to create non-linear springs, as opposed to using the secant value (E_s) or the 50% of ultimate (E_{50}) value.

Step 4: Create a single pile FEM-Winkler model with the non-linear springs, and apply a range of lateral loads to the pile head to verify correctness. Each combination of pile head deflection, lateral load and pile stress should agree with the field measurements.

Step 5: Incorporate the non-linear springs into the 2D or 3D FEM-Winkler model to more accurately predict the IAB's response to vehicular, thermal, wind or earthquake loading.

This process is well suited for IABs with abutment piles that are encased in a sleeve filled with a flexible medium because the piles are predominantly isolated from each other, and the influence of the reaction piles is assumed to be negligible. If the piles are not encased in a sleeve filled with a loose medium, then caution must be taken to account for the

interaction of adjacent piles by maintaining a safe distance (2.5m minimum as per ASTM D3966) between the reaction and test piles.

Chapter 8 – Conclusions and Recommendations

8.1 Conclusions

The cohesionless soils in which the Scoudouc Bridge piles are embedded have shown a certain degree of non-linearity; however, their response beyond a very low-strain yield point was predominantly linear. The pile head of the soil-pile system exhibited a similar response for each of the piles tested at the Scoudouc Bridge, as well as the pile at the Picadilly mine site.

To account for soil non-linearity, three modifications were made to the linear solutions or models. Firstly, factors established by Poulos and Davis (1980) were applied to the results obtained by the Poulos and Hull (1989) solution, and accurate results were obtained. Secondly, coupled springs were defined to more accurately represent the backfill system comprised of granular backfill with geogrid, and a compression foam at the abutment backwall interface. Lastly, non-linear soil springs were developed by compiling results from linear soil spring models, and when incorporated in the soil-pile system, the system response was accurate through the entire range of head loads.

The FEM-Winkler approach to predicting the response of laterally-loaded piles appears to provide results that are within the expected range of accuracy. Its simplicity and ease of use make it a commonly-used method for the design of IABs; however, the most important variable required in the process is the most difficult to determine with a high degree of certainty: the modulus of horizontal subgrade reaction, k_h . Many researchers such as Terzaghi (1955) have published values of soil stiffness parameters n_h , E_s or E_{50} for use in elastic solutions to SSI problems, and these can yield accurate results when

used properly. For instance, these published values allowed for an accurate prediction of soil-pile system response at high strains, such as those expected during thermal expansion and contraction (Huntley and Valsangkar, 2013) but underestimated the low-strain lateral stiffness of the soil-pile system, such as those resulting from vehicular loading.

The structural software program STAAD.Pro has proven to be a useful tool in “best-fitting” piles within a soil medium, to enable the prediction of pile lateral deflections and reactions along the pile by the FEM-Winkler method. Earlier methods of solving the “beam on elastic subgrade” problem, such as the finite difference and partial differentiation methods, did not permit the soil stiffness to be represented as non-linear. STAAD.Pro has multi-linear spring capability, and utilizes the user-input tangential segments of the P-Y curve to define the overall non-linearity. The FEM-Winkler approach, conducted with STAAD.Pro, takes much less effort than performing these lengthy and tedious procedures, often done manually in years pre-dating computers.

The elastic solutions of Broms (1964) and Poulos and Hull (1989) provided valuable preliminary single-pile design information which would have allowed the bridge design engineer to do early planning for the flexibility and support requirements of the Scoudouc IAB. The Abendroth and Greimann (1987) equivalent cantilever model provided the basis of a 2D bridge model founded on beam-columns. The results agreed well with all other forms of analyses, once an equivalent value of k_h was obtained. Their method of calculating the equivalent k_h is in concert with the philosophy that the stiffness in the top portion of the soil-pile system is far more critical to its lateral response than the soils at depth. This reinforces the concept that the soil modulus is more influential at the top of the pile than it is at the bottom. An aspect of this method that is welcomed by structural

engineers is the conversion of a composite, fully embedded “black box” system, to an idealized free-standing beam-column whose behaviour is very well understood.

The Hentenyi partial differential equation for estimating pile moments due to applied head load, moment or deflection provided unconservative results. The value of maximum pile moment was less than results obtained from all other methods. The principle of superposing the applied pile head moment to the solution which only considered the lateral deflection at ground level provided conservative, and more accurate results.

A simple lateral load test conducted on production piles provided the soil-pile system’s stiffness, from which inferred P-Y curves could be developed, and non-linear spring constants established. It is understood that the data gathered is essentially static, and that soil behaviour is strain and time dependent; however, even the instantaneous feedback can be used to calibrate the FEM-Winkler model to account for soil non-linearity.

A conventional Pile Driving Analyzer was effective in measuring the strain in the pile when subjected to a lateral head load. Most transportation agencies require that a certain percentage of piles within an IAB abutment be dynamically analyzed for axial capacity, so this equipment is often on site during the pile driving phase. The operator could easily be trained to participate in the lateral load pile tests.

The computer aided design software package AUTOCAD was used to facilitate the computations to determine the effective k_h at pile P5N, and could calculate the second moment of inertia of the irregular stiffness distribution with depth. This would save a design engineer valuable time, especially considering it is an iterative process (values of L_c and k_h are inter-dependent variables).

8.2 Recommendations

The time variation in stiffness of the soil which surrounds the piles should be considered in the design process of any IAB. The simple test described in this paper will provide the design engineer with a much better understanding of the behaviour of the soil-pile system as it is incorporated into the IAB; however, only the soil's initial state is tested. Further research should be done to establish production pile tests that could be conducted during the construction of the abutments to aid in forecasting the long-term, cyclic behaviour of the soil-pile system, and the response of the IAB. Long-term stiffness predictions must be made, based on scientific research and lateral load pile trials in different soil types.

The potential for degradation of some soil types is real, and has been recognized by some Canadian transportation agencies, such as Alberta Transportation. They have replaced the loose soil infill with polystyrene pellets, whose performance and durability are well documented. The use of synthetic materials, such as polystyrene pellets or shredded recycled rubber tires, as soil substitutes in IAB abutments should be investigated further.

It was assumed that the interaction between the reaction piles and test pile was negligible due to pile isolation; however, further investigation into the interaction between these piles, when encased in sleeves filled with a loose medium, is necessary to confirm if this is a valid assumption.

Further investigation into the strong linear relationship between lateral pile head load and deflection beyond an initially very stiff zone is recommended. This behaviour was observed at both the Picadilly site, in natural soil, and at the Scoudouc site, with

manufactured loose infill. At Scoudouc, there may exist a “flow” of particles from the front of the pile to the CSP interface, then split to follow the inside perimeter of the CSP sleeve, to finally rest at the backside of the pile once the push is completed.

Monitoring of the long-term pile strain after removal of the vehicular loading was not performed as this was beyond the scope of this work. Further studies should be conducted to confirm the variation of the residual deflection with time.

Studies should be conducted to measure the dynamic response of IAB production piles, such that characteristics such as damping may be better estimated. This variable is critical for the seismic design of IABs.

References

- Abendroth, R., Greimann, L. (1987) Rational Design for Integral Abutment Piles. Transportation Research Record 1223.
- Abendroth, R., Greimann, L. (2005) Field testing of Integral Abutments. Final Rep. HR-399, Iowa State University, Ames, Iowa.
- American Association of State Highway and Transportation Officials. (2002) AASHTO Standard Specifications for Highway Bridges, 17th Edition. 1028 pp.
- ASTM D3966-07 (2007) Standard Test Methods for Deep Foundations Under Lateral Load. American Society for Testing and Materials. 18 pp.
- Brena, S., Bonczar, C., Civjan, S. Dejong, J., Crovo, D. (2007) Evaluation of Seasonal and Yearly Behavior of Integral Abutment Bridge. Journal of Bridge Engineering, ASCE, 12(3). pp. 296-305.
- Broms, B. (1964a) Resistance of Piles in Cohesive Soils, Journal of the Soil Mechanics Division, ASCE, Vol. 90, No. SM3: 27-63.
- Broms, B. (1964b) Resistance of Piles in Cohesionless Soils, Journal of the Soil Mechanics Division, ASCE, Vol. 90, No. SM3: 123-156.
- Broms, B. (1965) Design of Laterally Loaded Piles, J. Soil Mech. and Found. Div., ASCE, 91 (SM3), 77-99.
- Broms, B., Ingelson, I. (1971) Earth Pressure Against the Abutments of a Rigid Frame Bridge. Geotechnique, 21(1). pp. 15-28.
- Budhu, M., Davies, T. (1986) Design Equations for Laterally Loaded Piles Embedded in Sand. Proceedings of the International Conference on Deep Foundations, Beijing, China, Sept. 1-5, 1986.
- Budhu, M., Davies, T. (1987). Non-linear Analysis of Laterally Loaded Piles in Cohesionless Soils. Canadian Geotechnical Journal, Vol. 24, pp. 289-296.
- Byrne, P., Cheung, H., Yan, L. (1987) Soil Parameters for Deformation Analysis of Sand Masses. Canadian Geotechnical Journal, 24(3).
- Canadian Highway Bridge Design Code (CAN CSA S6-14) (2016) Update No. 1, CSA Group, 875 pp.
- Canadian Foundation Engineering Manual, 3rd Edition. (1992) Canadian Geotechnical Society. 512 pp.
- Carter, M., Bentley, S. (1991) Correlations of Soil Properties. Pentech Press. 130 pp.
- Carvajal, J. (2011) Seismic Embankment Abutment Interaction for Integral Abutment Bridges, Ph.D Thesis, Faculty of Graduate Studies, UBC, Vancouver, British Columbia, Canada.

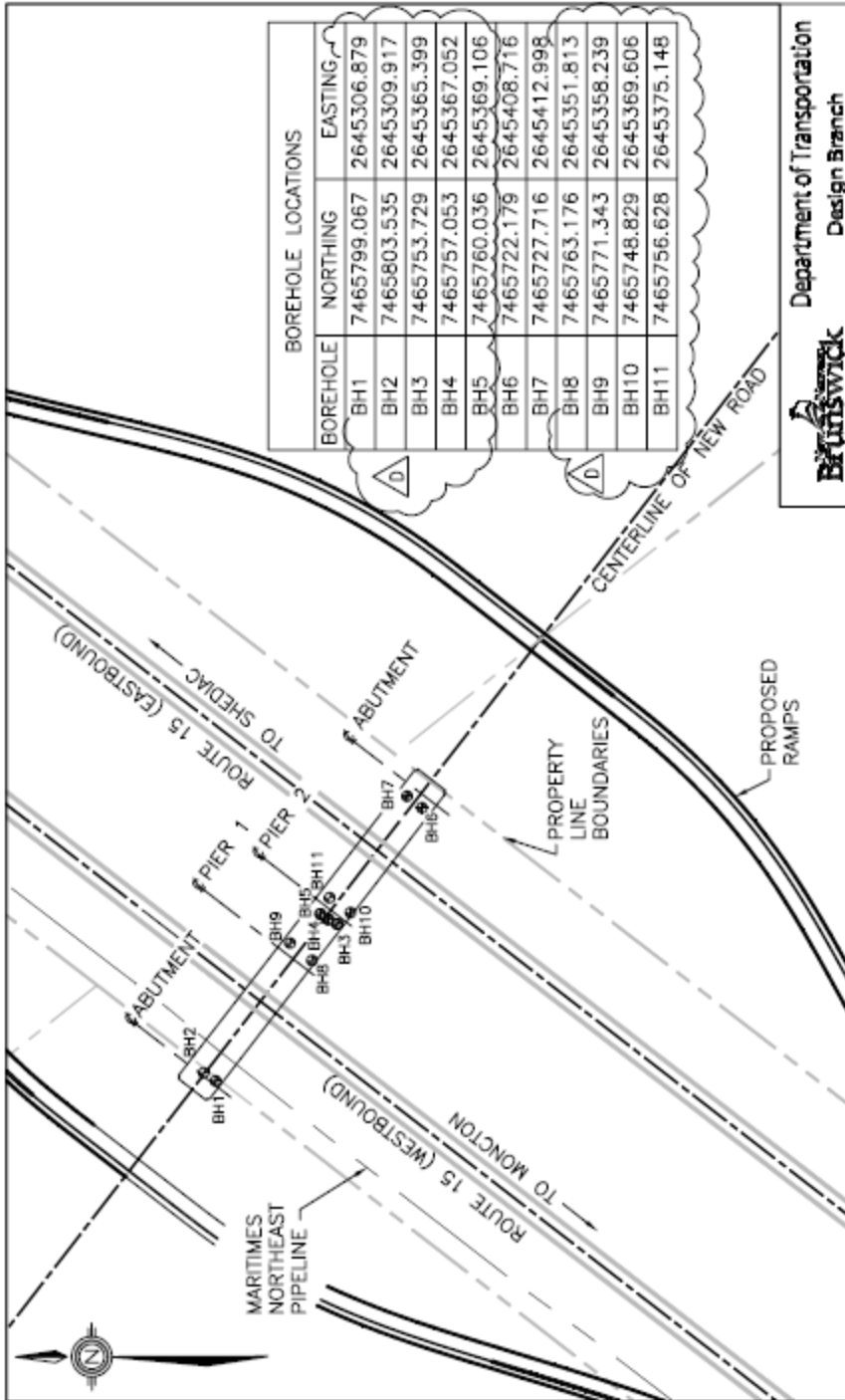
- Chen, W., Duan, L. (2000) *Bridge Engineering Handbook*. CRC Press. New York.
- Coduto, D. (2001) *Foundation Design Principles and Practices*. Prentice Hall. New Jersey. 883 pp.
- Cook, A., Abendroth, R. (2010) *Instrumentation and Monitoring of an Integral Abutment Bridge Supported on HP-Steel Piles/Concrete Drilled Shafts*. Iowa State University. Graduate Theses and Dissertations. Paper 11756.
- Davisson, M., Gill, H. (1963) Laterally Loaded Piles in a Layered Soil System. *Proc. American Society of Civil Engineers*, Vol. 89 SM3, pp.63-94.
- Davisson, M., Robinson, K. (1965) Bending and Buckling of Partially Embedded Piles. 6th International Conference on Soil Mechanics and Foundation Engineering. Montreal, Canada. Volume 2. pp. 243-246.
- Duncan, J., Byrne, P., Wong, K., Mabry, P. (1980) Strength, Stress-Strain and Bulk Modulus Parameters for Finite Element Analyses of Stresses and Movements in Soil Masses. Report No. UCB/GT/80-01. Office of Research Services, College of Engineering, University of California, Berkeley.
- El Naggar, H., Duguay, F., Mahgoub, A., Valsangkar, A. (2016) Impact of the Employed Soil Model on the Predicted Behaviour of Integral Abutment Bridges. 69th Canadian Geotechnical Conference, Vancouver, Canada.
- Fleming, K., Weltman, A., Randolph, M., Elson, K. (1992) *Piling Engineering*, Second Edition, Blackie & Son Ltd., London, 398 pages.
- Gle, D.R., Woods, R.D. (1984) Suggested Procedure for Conducting Dynamic Lateral-Load Tests on Piles. *American Society for Testing and Materials*. pp. 157-171
- Greimann, L., Wolde-Tinsae, A., Yang, P. (1982) Nonlinear Pile Behavior in Integral Abutment Bridges.
- Hetenyi, M. (1946) *Beams on Elastic Foundations*. Ann Arbor, University of Michigan Press.
- Hjelmstad, K., Taciroglu, E. (2003) Mixed Variational Methods for Finite Element Analysis of Geometrically Nonlinear Inelastic Bernoulli-Euler Beams, *Comm. J. Num. Meth. Engrg.*, 19, 809-832.
- Huang, J. (2011) Development of Modified P-Y Curves for Winkler Analysis to Characterize the Lateral Load Behavior of a Single Pile Embedded in Improved Soft Clay. Iowa State University. Graduate Theses and Dissertations. Paper 12114.
- Huntley, S., Valsangkar, A. (2014) Behaviour of H-Piles Supporting an Integral Abutment Bridge. *Canadian Geotechnical Journal*. Volume 51. pp. 713-734.
- Huntley, S., Valsangkar, A. (2013) Field Monitoring of Earth Pressures on Integral Bridge Abutments. *Canadian Geotechnical Journal*. Volume 50. pp 841-857.
- Kim, W., Laman, J. (2010a). Integral Abutment Bridge Response Under Thermal Loading, *Engineering Structures* 32(6): 1495–1508.

- Kim, W., Laman, J., Jeong, Y., Ou, Y, Roh, H. (2015) Comparative Study of Integral Abutment Bridge Structural Analysis Methods. *Canadian Journal of Civil Engineering*, Volume 43. pp. 378-389.
- Lindeburg, Carter, M. and Bentley, S. (1991). Correlations of soil properties. Penetech Press Publishers, London. And Peck, R., Hanson, W., and Thornburn, T. (1974). *Foundation Engineering Handbook*. Wiley, London.
- Matlock, H. (1970) Correlations for design of laterally loaded piles in soft clay. *In Proceedings of the 2nd Offshore Technology Conference*, Houston, Tex., Vol. 1, pp. 577–588.
- Mayne, P., Kulhawy, F. (1983). Closure, "K_o-OCR Relationships in Soil", *Journal of the Geotechnical Engineering Division, ASCE*, Vol. 109 (GT2), pp. 867-869.
- McClelland, B., Focht, J. Jr. (1958) Soil Modulus of Laterally Loaded Piles, *Transactions, American Society of Civil Engineers*, Vol 123, Paper No. 2954, 1049-1063.
- Meymand, P.J. (1998), "Shaking Table Scale Model Tests of Nonlinear Soil-Pile_Superstructure Interaction, In Soft Clay", PhD dissertation, University of California, Berkeley.
- Obrzud, R., Truty, A. (2012) *The Hardening Soil Model – A Practical Guidebook Z Soil*. PC 100701 report.
- Peck, R., Hansen, W., Thornburn, T. (1974) *Foundation Engineering*, 2nd ed. John Wiley and Sons, New York.
- Poulos, H., Hull, T. (1989) *The Role of Analytical Mechanics in Foundation Engineering*, *Foundation Engineering, Current Principles and Practices*, ASCE 2: 1578-1606.
- Poulos, H., Davis, E. (1980) *Pile Foundation Analysis and Design*. John Wiley and Sons Inc. New York.
- Randolph, M. (1981) Response of Flexible Piles to Lateral Loading, *Geotechnique*, 31(2), pp. 247-259.
- Reese, L., Cox, W., Koop, F. (1974) *Analysis of Laterally Loaded Piles in Sand*. Offshore Technology Conference, Houston, Texas. Paper No. OTC 2080.
- Reese, L., Welch, R. (1975) Lateral Loading of Deep Foundations in Stiff Clay, *J. Geotech. Eng. Div., ASCE*, 101 (GT7), pp. 633-649.
- Reese, L. (1977) Laterally loaded piles: Program documentation. *J. Geotech. Eng. Div., Am. Soc. Civ. Eng.*, 103(4), pp. 287–305.
- Taciroglu, E., Hjelmstad, K. (2003). "Mixed variational methods for finite element analysis of geometrically nonlinear inelastic Bernoulli-Euler beams," *Comm. J. Num. Meth. Engrg.*, 19, 809-832.
- Terzaghi, K. (1955) Evaluation of Coefficients of Subgrade Reaction. *Geotechnique*, Volume 5. pp. 297-326.

Timoshenko, S., Goodier, J. (1951) Theory of Elasticity, 2nd Edition. McGraw-Hill Book Company Inc. 1951.

Vesic, A. (1961) Beams on Elastic Foundations. In Proceedings of the 5th International Conference on Soil Mechanics and Foundation Engineering, Paris, 17-22 July 1961. Dunod, Paris. Vol. 1, pp. 845-850.

APPENDIX A - SCOUDOUC BRIDGE BOREHOLE LOGS



		Department of Transportation Design Branch	
project/project title SCOUDOC INDUSTRIAL DRIVE - ROUTE 15 U/P		SITE LAYOUT BOREHOLE LOCATIONS	
		No.: - rev. D	
10/14/09 date D	BOREHOLE LOCATIONS AS DRILLED IN THE FIELD CTD	design by/verify par EB	check by/verify par
02/12/09 date C	ADDED BOREHOLES AND RELOCATED BH1 & BH2 CTD	design by/verify par EB	check by/verify par
No.	revisions by/par	design by/verify par EB	check by/verify par
scale/echelle 1:2000	date DEC. 2008	drawn by/dessine par CTD	check by/verify par

BOREHOLE LOG REPORT

CLIENT NBDOT
 LOCATION SCOUDELOC INDUSTRIAL DRIVE - ROUTE 15 UPGRADE
 DATE 09/03/11 WATER LEVEL NOT MEASURED

PAGE 1 OF 1
 PROJECT No. 033-09
 BOREHOLE No. BH-1

ELEV. (M)	DEPTH (M)	SOIL DESCRIPTION	STRATA PLOT	WATER LEVEL	SAMPLE NO.	BLOW / 0.15m	R.O.D. or N	RECUPERATION (R)	COMMENTS	
47.06	0	SILTY SAND, SOME CLAY, TRACES OF GRAVEL, BROWN.	[Pattern]							
	0.30				SS-1	28	>50	80		
	0.68	BEDROCK: SANDSTONE, BROWN	[Pattern]		CB-1	30	81		SPLIT SPOON REFUSAL AT 0.68 METERS	
	1									COMPRESSION STRENGTH: 30.7 MPa (1.24 TO 1.49m)
	1.52				CB-2	8	100			
	2									
	3	BEDROCK: BEDDED SANDSTONE, GRAY	[Pattern]		CB-3	14	97			
	3.05									
	3.73									
	4				CB-4	38	100		COMPRESSION STRENGTH: 45.3 MPa (5.28 TO 5.40m)	
	4.57									
	5									
	6	END OF BOREHOLE AT 6.10 METERS								
	6.10									
	7									
	8									
	9									



BOREHOLE LOG REPORT

CLIENT NBDOT PAGE 1 OF 1
 LOCATION SCOUDOUC INDUSTRIAL DRIVE - ROUTE 15 UPGRADE PROJECT No. 033-09
 DATE 09/03/11 WATER LEVEL NOT MEASURED BOREHOLE No. BH-2

ELEV. (M)	DEPTH (M)	SOIL DESCRIPTION	STRATA PLOT	WATER LEVEL	SAMPLE NO.	BLOW / 0.15m	R.O.D. or N	RECUPIRATION (R)	COMMENTS
47.22	0	SILTY SAND, SOME CLAY, TRACES OF GRAVEL, BROWN.	[Pattern]						
	0.61				SS-1	50	>50	33	SPLIT SPOON REFUSAL AT 0.68 METERS
	0.68	BEDROCK: SANDSTONE, BROWN	[Pattern]		CB-1	20	81		COMPRESSION STRENGTH: 35.2 MPa (1.28 TO 1.45m)
	1								
	1.52				CB-2	8	97		
	2								
	3								
	3.05								
	3.96				CB-3	0	94		
	4	BEDROCK: BEDDED SANDSTONE, GRAY	[Pattern]						
	4.57								
	5				CB-4	18	100		COMPRESSION STRENGTH: 39.8 MPa (5.69 TO 5.71m)
	6								
	6.10	END OF BOREHOLE AT 6.10 METERS							
	7								
	8								
	9								



*APPENDIX B - PARTIAL DIFFERENTIATION SOLUTIONS FOR BEAM ON
ELASTIC SUBGRADE*

Beam on elastic subgrade solution for P5N

$$E_p I_p \frac{d^4 y}{dx^4} = Q \frac{d^2 y}{dx^2} = E_s y = 0$$

$$V = \frac{d^3 y}{dx^3} \quad M = EI \frac{d^2 y}{dx^2} \quad s = \frac{dy}{dx}$$

Assume solution of the form

$$y = e^{mx}$$

$$y^I = m e^{mx}$$

$$y^{II} = m^2 e^{mx}$$

$$y^{III} = m^3 e^{mx}$$

$$y^{IIII} = m^4 e^{mx}$$

Where

$$E_p = 205000 \text{ N/mm}^2$$

$$I_p = 293.0 \times 10^6 \text{ mm}^4$$

$$E_s = K_{he} \times d$$

$$= 10538 \text{ KN/m}^3 \times 0.3 \text{ m}$$

$$= 3267 \text{ KN/m}^2$$

$$= 3.3 \text{ N/mm}^2$$

$$\therefore E_p I_p \times m^4 e^{mx} + E_s \times e^{mx} = 0$$

$$e^{mx} (E_p I_p \times m^4 + E_s) = 0$$

$$e^{mx} (205000 \times 293.0 \times 10^6 m^4 + 3.3) = 0$$

$$e^{mx} (60.0 \times 10^{12} m^4 + 3.3) = 0$$

$$\begin{aligned} \therefore \quad \text{roots} \quad & 0.00034+0.00034i \\ & 0.00034-0.00034i \\ & -0.00034+0.00034i \\ & -0.00034-0.00034i \end{aligned}$$

Euler identities $e^{ix} = \cos x + i \sin x$

$$e^{-ix} = \cos x - i \sin x$$

$$\begin{aligned} y &= C_1 e^{(0.00034+0.00034i)x} + C_2 e^{(-0.00034+0.00034i)x} + C_3 e^{(-0.00034-0.00034i)x} + C_4 e^{(0.00034-0.00034i)x} \\ &= e^{0.00034x} (C_1 e^{0.00034ix} + C_4 e^{-0.00034ix}) + e^{-0.00034x} (C_2 e^{0.00034ix} + C_3 e^{-0.00034ix}) \\ &= e^{0.00034x} [C_1 (\cos 0.00034x + i \sin 0.00034x) + C_4 (\cos 0.00034x - i \sin 0.00034x)] \\ &\quad + e^{-0.00034x} [C_2 (\cos 0.00034x + i \sin 0.00034x) + C_3 (\cos 0.00034x - i \sin 0.00034x)] \\ &= e^{0.00034x} [(C_1 + C_4) \cos 0.00034x + (iC_1 - iC_4) \sin 0.00034x] \\ &\quad + e^{-0.00034x} [(C_2 + C_3) \cos 0.00034x + (iC_2 - iC_3) \sin 0.00034x] \\ &= e^{0.00034x} (A \cos 0.00034x + B \sin 0.00034x) + e^{-0.00034x} (C \cos 0.00034x + D \sin 0.00034x) \end{aligned}$$

Apply Boundary conditions:

$$y=37\text{mm} \quad @ \quad x=0$$

$$y=0\text{mm} \quad @ \quad x=\infty$$

$$dy/dx = 0 \quad @ \quad x=\infty$$

$$E_p I_p d^2y/dx^2 \quad @ \quad x=0$$

$$37=1(A+0)+1(C+0) \quad A+C=37$$

$$0=\infty(A\cos\infty+B\sin\infty)+0(C\cos\infty+0\sin\infty) \quad \therefore \cos\infty=\sin\infty$$

$$0=\infty(A\sin\infty+B\sin\infty)$$

$$0=A\sin\infty+B\sin\infty$$

$$\begin{aligned} dy/dx = & -e^{0.00034x} \times 0.00034A \times \sin 0.00034x + 0.00034e^{0.00034x} \times A \cos 0.00034x \\ & + e^{0.00034x} \times 0.00034B \times \cos 0.00034x + 0.00034e^{0.00034x} \times B \sin 0.00034x \\ & - e^{-0.00034x} \times 0.00034C \sin 0.00034x - 0.00034e^{-0.00034x} \times C \cos 0.00034x \\ & + e^{-0.00034x} \times 0.00034D \cos 0.00034x - 0.00034e^{-0.00034x} \times D \sin 0.00034x \end{aligned}$$

$$0 = -\infty A \sin \infty + \infty A \sin \infty$$

$$+ \infty B \sin \infty + \infty B \sin \infty$$

$$- 0 C \sin \infty - 0 C \sin \infty$$

$$+ 0 D \sin \infty - 0 D \sin \infty$$

$$0 = 2 \infty B \sin \infty \quad \therefore \quad B=0$$

$$A+B = 0 \quad \therefore \quad A=0$$

$$A+C=37 \quad \therefore \quad C=37$$

$$dy/dx = -e^{-0.00034x} 0.00034 C \sin 0.00034x - 0.00034 e^{-0.00034x} \cos 0.00034x \\ + e^{-0.00034x} 0.00034 D \cos 0.00034x - 0.00034 e^{-0.00034x} D \sin 0.00034x$$

$$d^2y/dx^2 = 4.28 \times 10^{-6} e^{-0.00034x} \sin(0.00034x) - 4.28 \times 10^{-6} e^{-0.00034x} \cos 0.00034x \\ - (-4.28 \times 10^{-6}) e^{-0.00034x} \cos 0.00034x + 4.28 \times 10^{-6} e^{-0.00034x} \sin 0.00034x \\ + (-115.6 \times 10^{-9} D) e^{-0.00034x} \cos 0.00034x - 115.6 \times 10^{-9} D e^{-0.00034x} \sin 0.00034x \\ + (115.6 \times 10^{-9} D) e^{-0.00034x} \sin 0.00034x - 115.6 \times 10^{-9} D e^{-0.00034x} \cos 0.00034x$$

$$0 = [-4.27 \times 10^{-6} + 4.28 \times 10^{-6} - 115.6 \times 10^{-9} D - 115.6 \times 10^{-9} D]$$

$$\therefore D = 0$$

$$@x=0: y = e^{-0.00034x} (37 \cos 0.00034x + (37 \times 200000 \times 286.4 \times 10^6), \sin 0.00034x) \\ = 1 \quad (37)$$

$$@x=\infty: dy/dx = -e^{-0.00034x} 37 \sin 0.00034x - 0.00034 e^{-0.00034x} 37 \cos 0.00034x \\ + e^{-0.00034x} 0.00034 (137.14) \cos 0.00034x - 0.00034 e^{-0.00034x} (+34.14) \sin 0.00034x \\ = 0$$

$$@x=0 \quad d^2y/dx^2 = (4.28 \times 10^{-6}) (e^{-0.00034x}) \sin(0.00034x) - 4.28 \times 10^{-6} (e^{-0.00034x}) \cos 0.00034x \\ - (-4.28 \times 10^{-6}) e^{-0.00034x} \cos 0.00034x + 4.28 \times 10^{-6} e^{-0.00034x} \sin 0.00034x \\ + (-115.6 \times 10^{-9} (0)) e^{-0.00034x} \cos 0.00034x - 115.6 \times 10^{-9} (0) e^{-0.00034x} \sin 0.00034x \\ + (115.6 \times 10^{-9} (0)) e^{-0.00034x} \sin 0.00034x - 115.6 \times 10^{-9} (0) e^{-0.00034x} \cos 0.00034x \\ = -4.28 \times 10^{-6} + 4.28 \times 10^{-6} \\ = 0$$

∴ calculate M @ x = 1000

$$\begin{aligned}d^2y/dx^2 &= 1.01 \times 10^{-6} - 4.04 \times 10^{-6} + 4.04 \times 10^{-6} + 1.01 \times 10^{-6} \\ &= 2.02 \times 10^{-6}\end{aligned}$$

$$\begin{aligned}\therefore M &= 2.02 \times 10^{-6} \times 205000 \times 293.0 \times 10^6 \\ &= 121.3 \times 10^6 \text{ Nmm} \\ &= 121.3 \text{ kNm}\end{aligned}$$

calculate M @ x = 2500

$$\begin{aligned}d^2y/dx^2 &= 1.37 \times 10^{-6} - 1.21 \times 10^{-6} + 1.21 \times 10^{-6} + 1.37 \times 10^{-6} \\ &= 2.74 \times 10^{-6}\end{aligned}$$

$$\begin{aligned}\therefore M &= 2.74 \times 10^{-6} \times 205000 \times 293.0 \times 10^6 \\ &= 164.6 \times 10^6 \text{ Nmm} \\ &= 164.6 \text{ kNm}\end{aligned}$$

Now modify BC to account for moment at ground level as a result of eccentricity

From STAAD: $M_{\text{GROUND}} = 85.0 \text{ kNm}$

From CALL: $M_{\text{GROUND}} = 0.55 \times 155.8 = 85.7 \text{ kNm}$

Modified BC: $d^2y/dx^2 = 85.0 \times 10^6 \text{ Nmm} / 200000 \text{ N/mm}^2 \times 286.4 \times 10^6 \text{ mm}^4$
 $= 1.484 \times 10^{-6} / \text{mm}$

$$d^2y/dx^2 = 4.28 \times 10^{-6} e^{-0.00034x} \sin(0.00034x) + 4.28 \times 10^{-6} e^{-0.00034x} \cos(0.00034x)$$

$$\begin{aligned}
&+ 4.28 \times 10^{-6} e^{-0.00034x} \cos(0.00034x) + 4.28 \times 10^{-6} e^{-0.00034x} \sin(0.00034x) \\
&- 115.6 \times 10^{-9} D e^{-0.00034x} \cos(0.00034x) - 115.6 \times 10^{-9} D e^{-0.00034x} \sin(0.00034x) \\
&+ 115.6 \times 10^{-9} D e^{-0.00034x} \sin(0.00034x) - 115.6 \times 10^{-9} D e^{-0.00034x} \cos(0.00034x)
\end{aligned}$$

$$1.484 \times 10^{-6} = -4.28 \times 10^{-6} + 4.28 \times 10^{-6} - 115.6 \times 10^{-9} D - 115.6 \times 10^{-9}$$

$$\therefore D = -6.42$$

$$y = e^{-0.00034x} (A \cos 0.00034x + B \sin 0.00034x) + e^{-0.00034x} (C \cos 0.00034x + D \sin 0.00034x)$$

$$y = e^{-0.00034x} (37 \cos 0.00034x + D \sin 0.00034x)$$

$$dy/dx = 0.00034 \cdot e^{-0.00034x} \cdot [(D-37) \cos 0.00034x - (D+37) \sin 0.00034x]$$

$$d^2y/dx^2 = -0.231 \times 10^{-6} \cdot e^{-0.00034x} \cdot (D \cos 0.00034x - 37 \sin 0.00034x)$$

Evaluate d^2y/dx^2 with $D = 0$ and $x = 1000$:

$$d^2y/dx^2 = 2.03 \times 10^{-6} \quad \therefore \quad M = 121.9 \text{ kNm}$$

Evaluate d^2y/dx^2 with $D = -6.42$ and $x = 1000$:

$$d^2y/dx^2 = 3.03 \times 10^{-6} \quad \therefore \quad M = 182.0 \text{ kNm}$$

Evaluate d^2y/dx^2 with $D = -6.42$ and $x = 2500$

$$d^2y/dx^2 = 3.17 \times 10^{-6} \quad \therefore \quad M = 190.4 \text{ kNm}$$

Evaluate d^2y/dx^2 with $D = -6.42$ and $x = 3000$

$$d^2y/dx^2 = 2.91 \times 10^{-6} \quad \therefore \quad M = 174.8 \text{ kNm}$$

Evaluate d^2y/dx^2 with $D = -6.42$ and $x = 2000$

$$d^2y/dx^2 = 3.31 \times 10^{-6} \quad \therefore \quad M = 198.8 \text{ kNm MAX!}$$

Evaluate d^2y/dx^2 with $D = -6.42$ and $x = 1500$

$$d^2y/dx^2 = 3.29 \times 10^{-6} \quad \therefore \quad M = 197.6 \text{ kNm}$$

APPENDIX C - PICADILLY PILE TEST DATA

STATIC PUSH TEST ON PILE T-3024 in EAST DIRECTION					
T-3024	T-3024		Gauge		T-3024
Reading	Displ.	Cum. Displ.	Reading	Force	Force
(mm)	(mm)	(mm)	(psi)	(lbs)	(kN)
218.0	0.0	0.0	0.0	0.0	0.0
219.0	1.0	1.0	1000.0	5150.0	22.9
220.0	1.0	2.0	1600.0	8240.0	36.7
221.0	1.0	3.0	2000.0	10300.0	45.8
222.0	1.0	4.0	2200.0	11330.0	50.4
223.0	1.0	5.0	2800.0	14420.0	64.1
224.0	1.0	6.0	3100.0	15965.0	71.0
225.0	1.0	7.0	3300.0	16995.0	75.6
226.0	1.0	8.0	3600.0	18540.0	82.5
227.0	1.0	9.0	4100.0	21115.0	93.9
228.0	1.0	10.0	4200.0	21630.0	96.2
229.0	1.0	11.0	4500.0	23175.0	103.1
230.0	1.0	12.0	5200.0	26780.0	119.1
231.0	1.0	13.0	5600.0	28840.0	128.3
232.0	1.0	14.0	5800.0	29870.0	132.9
233.0	1.0	15.0	6200.0	31930.0	142.0
234.0	1.0	16.0	6500.0	33475.0	148.9
235.0	1.0	17.0	6900.0	35535.0	158.1
236.0	1.0	18.0	7100.0	36565.0	162.6
237.0	1.0	19.0	7400.0	38110.0	169.5

LOG OF BOREHOLE BH109

SHEET 1 OF 2

PROJECT No.: TE73031 CLIENT: Potash Corp PROJECT NAME: Picadilly Mine Site LOCATION: Penobsquis, NB DATE DRILLED: 2-8-08 LOGGED BY: L.Sharpe	ELEVATION: 33.34 m DATUM: Geodetic METHOD: Auger DIAMETER: 150 mm WATER LEVEL: 0.91 m CONTRACTOR: Boart Longyear	
---	---	--

DEPTH (m)	ELEVATION (m)	STRATIGRAPHIC DESCRIPTION	STRATA PLOT	WATER LEVEL	SAMPLES				UNDRAINED SHEAR STRENGTH (kPa)				PLASTIC NATURAL LIQUID LIMIT MOISTURE CONTENT				
					TYPE	NUMBER	RECOVERY (mm)	N-VALUE or PROB %	OTHER TESTS	STANDARD PENETRATION TESTS Blows/0.3m				W _p	W	W _L	
										20	40	60	80				20
0	33.34				AU												
1	32.42	Loose, brown silty SAND with organic matter and wood debris.			SS	1	125	4									
2		Compact brown silty SAND with some gravel.			SS	2	400	18									
3					SS	3	375	25									
4					SS	4	425	15									
5	28.77	Compact to very dense silty clayey SAND with gravel.			AU												
6					SS	5	375	12									
7					SS	6	250	20									
8					AU												
9					SS	7	225	15									
10					SS	8	150	18									
11					AU												
12					SS	9	275	21									
13					SS	10	350	51									
14					AU												
15					SS	11	375	26									
16					SS	12	250	50									
17	23.89	Poor quality, fine-grained sandstone BEDROCK with siltstone seams near top of rock layer.			SS	13	125	34 50-50									

GEOTECHNICAL BOREHOLE PCS - PENOBSQUIS & PICADILLY GPJ AMEC HALIFAX GDT 5/13/08

LOG OF BOREHOLE BH110

SHEET 1 OF 1

PROJECT No.: TE73031 CLIENT: Potash Corp PROJECT NAME: Picadilly Mine Site LOCATION: Penobsquis, NB DATE DRILLED: 2-5-08 LOGGED BY: L.Sharpe	ELEVATION: 34.38 m DATUM: Geodetic METHOD: Auger DIAMETER: 150 mm WATER LEVEL: 1.22 m CONTRACTOR: Boart Longyear	
---	---	--

DEPTH (m)	ELEVATION (m)	STRATIGRAPHIC DESCRIPTION	STRATA PLOT	WATER LEVEL	SAMPLES					UNDRAINED SHEAR STRENGTH (kPa)			PLASTIC NATURAL LIQUID LIMIT MOISTURE CONTENT				
					TYPE	NUMBER	RECOVERY (%)	N-VALUE or RQD%	OTHER TESTS	STANDARD PENETRATION TEST Blows/0.3m			W _p	W	W _L		
										20	40	60				10	20
0	34.38	Loose to compact brown silty SAND, trace gravel.			AU												
1					SS	1	250	9		•							
	32.85	Compact to dense brown silty clayey SAND with gravel.			SS	2	300	16		•							
2					SS	3	400	17		•							
					SS	4	450	56			•						
3					AU												
					SS	5	475	18		•							
4					SS	6	375	19		•							
5					AU												
					SS	7	0	26		•							
6					SS	8	300	26		•							
7					AU												
					SS	9	375	39			•						
8		- Cobbles			SS	10	225	23 37 50-100									
					AU												
					SS	11	375	36		•							
					SS	12	225	45 50-75									
9	25.23	End of Borehole @ 9.1 m			AU												

GEO TECHNICAL BOREHOLE_PCS_PENOBOSQUIS & PICADILLY.OPJ_AMEC-HALIFAX.GDT_01/08/08

LOG OF BOREHOLE BH111

SHEET 1 OF 2


PROJECT No.: TE73031 CLIENT: Potash Corp PROJECT NAME: Picadilly Mine Site LOCATION: Penobsquis, NB DATE DRILLED: 2-12-08 LOGGED BY: L.Sharpe	ELEVATION: 32.59 m DATUM: Geodetic METHOD: Auger DIAMETER: 150 mm WATER LEVEL: 0.91 m CONTRACTOR: Boart Longyear	
--	---	--

DEPTH (m)	ELEVATION (m)	STRATIGRAPHIC DESCRIPTION	STRATA PLOT	WATER LEVEL	SAMPLES				UNDRAINED SHEAR STRENGTH (kPa)				PLASTIC NATURAL LIQUID					
					TYPE	NUMBER	RECOVERY (mm)	N-VALUE or ROD%	OTHER TESTS	STANDARD PENETRATION TEST				W _p	W	W _L		
										Blows/0.3m							WATER CONTENT (%)	
0	32.59	Compact brown silty SAND with some gravel.			AU													
1					SS 1	250	25		•									
2					SS 2	325	26		•									
3	30.00				SS 3	400	12		•									
		Compact brown SAND with trace silt			SS 4	350	27		•									
3					AU													
4					SS 5	350	14		•									
5					SS 6	400	17		•									
6					AU													
7					SS 7	150	19		•									
8					AU													
9					SS 8	50	13		•									
10					AU													
11					SS 9	100	10		•									
	24.05				Compact to very dense brown silty clayey SAND with gravel.			SS 10	100	14		•						
9		AU																
11		SS 11	425	34					•									

GEOTECHNICAL BOREHOLE PCS - PENOBSQUIS & PICADILLY, GPJ, AMEC HALEX, GDT 8/13/08

LOG OF BOREHOLE BH112

SHEET 1 OF 1

PROJECT No.: TE73031 CLIENT: Potash Corp PROJECT NAME: Picadilly Mine Site LOCATION: Penobsquis, NB DATE DRILLED: 2-8-08 LOGGED BY: L.Sharpe	ELEVATION: 33.05 m DATUM: Geodetic METHOD: Auger DIAMETER: 150 mm WATER LEVEL: 0.61 m CONTRACTOR: Bort Longyear	
---	--	---

DEPTH (m)	ELEVATION (m)	STRATIGRAPHIC DESCRIPTION	STRATA PLOT	WATER LEVEL	SAMPLES				UNDRAINED SHEAR STRENGTH (kPa)				PLASTIC NATURAL LIQUID LIMIT MOISTURE CONTENT						
					TYPE	NUMBER	RECOVERY (mm)	N-VALUE or RQD%	OTHER TESTS	STANDARD PENETRATION TEST Blows/0.3m				W _p	W	W _L			
										20	40	60	80				10	20	30
0	33.05	Compact to dense brown silty SAND with gravel		▽	AU														
0.5					SS 1	200	17												
1.0					SS 2	325	32												
1.5					SS 3	375	39												
2.0					SS 4	500	35												
2.5					AU														
3.0					SS 5	375	53												
3.5					SS 6	0	17												
4.0					AU														
5.5	27.56				Compact to dense brown silty clayey SAND with gravel - Increasing clay content		▽	AU											
6.0								SS 7	0	19									
6.5		SS 8	200	22															
7.0		AU																	
7.5		SS 9	250	16															
8.0		AU																	
8.5		SS 10	425	29															
9.0		SS 11	75	14 50-2															
9.8	23.30	End of Borehole @ 9.8 m																	

GEO-TECHNICAL BOREHOLE PCS - PENOBSQUIS & PICADILLY GPJ, AMEC HALIFAX, GDT, 5/13/08

APPENDIX D – SCOUDOUC PILE TEST DATA

Table 3.1 Static Push Test on Pile P5N.

		West			East				P5N	P4	P6
Displ.	Cum.	Reading	Force	Force	Reading	Force	Force	Tot.	Tot.	Tot.	
(mm)	(mm)	(psi)	(lbs)	(kN)	(psi)	(lbs)	(kN)	(kN)	(kN)	(kN)	
0.0	0.0	0.0	0.0	0.0	0.0	0.0	0.0	0.0	0.0	0.0	
0.7	0.7	450.0	2317.5	10.3	450.0	2317.5	10.3	20.6	10.5	10.1	
0.4	1.1	600.0	3090.0	13.7	600.0	3090.0	13.7	27.5	14.0	13.5	
0.8	1.9	700.0	3605.0	16.0	800.0	4120.0	18.3	34.4	17.5	16.9	
0.7	2.6	900.0	4635.0	20.6	850.0	4377.5	19.5	40.1	20.4	19.7	
0.6	3.2	1000.0	5150.0	22.9	1000.0	5150.0	22.9	45.8	23.3	22.5	
0.7	3.9	1100.0	5665.0	25.2	1150.0	5922.5	26.3	51.5	26.3	25.3	
0.8	4.7	1200.0	6180.0	27.5	1250.0	6437.5	28.6	56.1	28.6	27.5	
0.7	5.4	1400.0	7210.0	32.1	1350.0	6952.5	30.9	63.0	32.1	30.9	
0.7	6.1	1500.0	7725.0	34.4	1450.0	7467.5	33.2	67.6	34.4	33.1	
0.8	6.9	1600.0	8240.0	36.7	1600.0	8240.0	36.7	73.3	37.4	35.9	
0.9	7.8	1750.0	9012.5	40.1	1600.0	8240.0	36.7	76.7	39.1	37.6	
0.6	8.4	1800.0	9270.0	41.2	1800.0	9270.0	41.2	82.5	42.0	40.4	
0.7	9.1	1900.0	9785.0	43.5	1900.0	9785.0	43.5	87.1	44.4	42.7	
0.7	9.8	1900.0	9785.0	43.5	2050.0	10557.5	47.0	90.5	46.1	44.4	
0.7	10.5	2100.0	10815.0	48.1	2150.0	11072.5	49.3	97.4	49.6	47.7	
0.6	11.1	2250.0	11587.5	51.5	2200.0	11330.0	50.4	101.9	52.0	50.0	
0.7	11.8	2250.0	11587.5	51.5	2400.0	12360.0	55.0	106.5	54.3	52.2	
0.7	12.5	2400.0	12360.0	55.0	2500.0	12875.0	57.3	112.3	57.2	55.0	
0.5	13.0	2500.0	12875.0	57.3	2500.0	12875.0	57.3	114.5	58.4	56.2	
0.8	13.8	2600.0	13390.0	59.6	2650.0	13647.5	60.7	120.3	61.3	59.0	
0.7	14.5	2600.0	13390.0	59.6	2900.0	14935.0	66.4	126.0	64.2	61.8	
0.6	15.1	2800.0	14420.0	64.1	2950.0	15192.5	67.6	131.7	67.1	64.6	
0.8	15.9	2850.0	14677.5	65.3	3050.0	15707.5	69.9	135.2	68.9	66.3	
0.9	16.8	2850.0	14677.5	65.3	3250.0	16737.5	74.5	139.7	71.2	68.5	
0.6	17.4	3100.0	15965.0	71.0	3200.0	16480.0	73.3	144.3	73.5	70.8	
0.7	18.1	3300.0	16995.0	75.6	3250.0	16737.5	74.5	150.0	76.5	73.6	
0.8	18.9	3400.0	17510.0	77.9	3400.0	17510.0	77.9	155.8	79.4	76.4	

APPENDIX E – SCOUDOUC BRIDGE LIVE LOAD TEST DATA

Table E.1 Deck Deflections due to Vehicular Live Load.

Rear Wheel Station (m)	Deflection Measured (mm)	Deflection STAAD (mm)
0*	-2	0.0
2	-3	-0.4
4	-2	-1.1
6	-3	-1.9
8	-3	-2.8
10	-2	-4.0
12	-4	-4.9
14	-6	-5.9
16	-6	-6.9
18	-7	-7.5
20	-7	-8.1
22	-8	-8.7
24	-8	-8.9
26	-11	-9.0
28	-10	-9.0
30	-10	-8.7
32	-9	-8.3
34	-11**	-7.6
36	-8	-6.9
38	-6	-6.1
40	-2	-5.0
42	-5	-4.1
44	-3	-3.1
46	-3	-2.1
48	-2	-1.2

*North_abutment

**Suspect_reading

APPENDIX F - BROMS COMPUTATIONAL SOLUTION

Long Pile, Free Head, Cohesionless Soil - Broms (1964b)

Ultimate Lateral Resistance	$H_u/k_p d^3 \gamma$	210	where	$H_u=$	312	kN
		(Fig. H.1)		$k_p=$	2.8	
				$d=$	0.31	m
	$e=$	0.55	m	$\gamma=$	18	kN/m ³
	$e/d=$	1.77				

System Yield Moment	$M_y/k_p \gamma d^4$	1437	where	$M_y=$	662	kNm
				$k_p=$	2.8	
				$\gamma=$	18	kN/m ³
				$d=$	0.31	m

Passive Soil Pressure Coefficient	$\tan^2(45+\phi'/2)$			$k_p=$	2.8	
				$\phi'=$	28	degrees
				$\phi'=$	0.49	radians

Pile Yield Moment	$f_y S$	662	kNm	$f_y=$	350	MPa
				$f_y=$	350000	kN/m ²
				$S=$	1890	cm ³
				$S=$	0.00189	m ³
				$I=$	0.000293	m ⁴

Where

$H_u=$	Ultimate lateral pile head load	(kN)
$k_p=$	Rankine passive soil pressure coefficient	
$d=$	Pile diameter	(m)
	Unit weight of	
$\gamma=$	soil	(kN/m ³)
$e=$	Length of unsupported pile	(m)
	Pile yield	
$M_y=$	moment	(kNm)
$\phi'=$	Effective friction angle of soil	(radians)
$f_y=$	Pile yield stress	(MPa)

$S =$ Pile section modulus (m^3)
 $I =$ Pile moment of inertia (m^4)

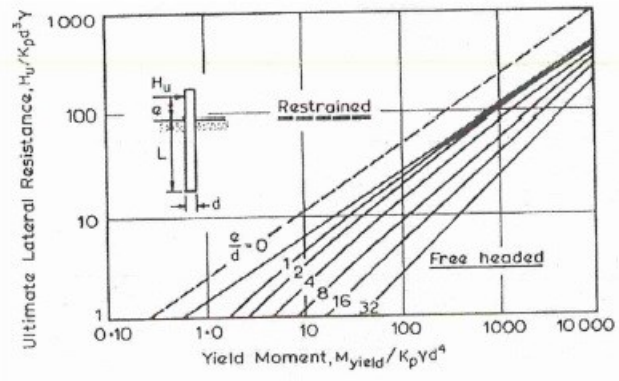


Figure H.1 Long Pile, from Broms, 1964b.

APPENDIX G - POULOS AND HULL COMPUTATIONAL SOLUTION

Long Pile, Free Head, Cohesionless Soil -

Poulos and Hull (1989)

Applied moment	M=		85.0	kNm
Applied horiz force	H=		155.8	kN
Critical Length	$L_c=$	$1.81dK^{0.2}$	6.13	m
	$m=$	n_h		kN/m^3
	$K_e=$		155303	
Diameter	$d=$		0.31	m
	$n_{h1}=$	0-3m	4400	kN/m^3
	$n_{h2}=$	3-5m	24000	kN/m^3
	$n_{h3}=$	5-9.3m	12000	kN/m^3
	$e=$		0.55	m
	$L_o=$	$L_c/2$	3.06	m
parallel axis theorem to find equivalent k_h	actual 2nd mom inertia=		0	m^4
	actual 2nd mom inertia=		101000	m^4
	rectangular 2nd mom inertia=		9.59	$*k_{he}$
	$k_{he}=$	act 2nd MI/rect 2nd MI	10537	kN/m^3
	triangular 2nd mom inertia=		2.40	$*k_{hmax}$
	$k_{hmax}=$	rect 2nd MI/triang 2nd MI	42147	kN/m^3
	$E_{smax}=$		13065	kN/m^2
	$m=n_h=$		4265	$kN/m^2/m$
	$K=$	$E_p/(m*d)$		Unitless
	$K_e=$	$E_p/(m_e*d)$	155064	Unitless
Pile Mod of Elast	$E_p=$		205000	Mpa
Pile Mod of Elast	$E_p=$		205000000	kN/m^2
Length of embed pile	$L=$		9.3	m
Variable	$x=$	$\log_{10}(L_e/d)$	1.30	Unitless
	$L_e=$	L_c if $L \geq L_c$	6.13	m
		L if $L < L_c/3$	9.3	m

Factor	$f_{\rho H} =$	$(13.10+11.09x)/mL_c^2$	0.000172	Unitless
Factor	$f_{\rho M} = f_{\phi H} =$	$(34.63+11.09x)/mL_c^3$	4.995E-05	Unitless
Factor	$f_{\phi M} =$	$(156.1+37.14x)/mL_c^4$	3.397E-05	Unitless
Factor	$f_{\rho F} =$	$(5.669+4.14\log_{10}x)/mL_c^2$	3.832E-05	Unitless
Factor	$I_{MF} =$	$(L_c/d)(0.23+0.44\log_{10}x)$	5.525	Unitless
Grounline defl	$\rho_{elas\ ground} =$	$Hf_{\rho H} + Mf_{\rho M}$	0.031	m
Groundline rot	$\varphi_{elas} =$	$Hf_{\phi H} + Mf_{\phi M}$	0.011	rad
Max moment	$M_{elas} =$	HdI_{MF}	266.9	kNm
Pile head defl	$\Delta_{elas} =$	$\varphi_{elas}e$	0.011	m
	$\rho_{elas\ head} =$	$\rho_{elas\ ground} + \Delta_{elas}$	0.042	m
	$e/L =$	(0 at ground)	0.059	or zero!
	$\Delta_{plas} =$	$\varphi_{plas}e$	0.015	m
	$\rho_{plas\ ground} =$	$\rho_{elas\ ground}/F_{\rho}$	0.050	m
	$\rho_{plas\ head} =$	$\rho_{elas\ head}/F_{\rho}$	0.067	m
	$\varphi_{plas} =$	$\varphi_{elas}/F_{\varphi}$	0.015	rad
	$M_{plas} =$	M_{elas}/F_{φ}	381.2	kNm
	$I_p =$	0.000293	m ⁴	
	$E_{se} =$	3266	kN/m ²	
	$L =$	9.3	m	
	$K_R =$	0.00246	Unitless	$E_p I_p / E_s L^4$
	$H_u =$	312	kN	from Broms
	$H/H_u =$	0.5	Unitless	
	$F_{\rho} =$	0.62	Unitless	from Fig 8.16
	$F_{\varphi} =$	0.70	Unitless	from Fig. 8.17

Where

M	Applied head moment	(kNm)
H	Applied lateral head load	(kN)
L_c	Critical pile length	(m)
K_e	Effective K constant	Unitless
d	Pile diameter	(m)
n_{hi}	Variation of k_h with depth for soil layer i	(kN/m ³)
L_o	Active pile length	(m)
k_{he}	Effective k_h	(kN/m ³)
k_{hmax}	Maximum k_h	(kN/m ³)
E_{smax}	Maximum E_s	(kN/m ²)
m	Variation of E_s with depth	(kN/m ³)
m_e	Effective Variation of E_s with depth	(kN/m ³)
E_p	Pile modulus of elasticity	(MPa)
L	Length of embedded pile	(m)
L_e	Effective pile length	(m)
ρ_{elas}		
ρ_{ground}	Pile deflection at groundline	(m)
ϕ_{elas}	Elastic Pile rotation at groundline	(rad)
M_{elas}	Maximum elastic pile moment	(kNm)
Δ_{elas}	Elastic Deflection difference from ground to pile head	(m)
$\rho_{elas\ head}$	Elastic pile deflection at head	(m)
Δ_{plas}	Plastic Deflection difference from ground to pile head	(m)
ρ_{plas}		
ρ_{ground}	Plastic pile deflection at ground	(m)
$\rho_{plas\ head}$	Plastic pile deflection at head	(m)
ϕ_{plas}	Plastic Pile rotation at groundline	(rad)
M_{plas}	Maximum plastic pile moment	(kNm)
I_p	Pile moment of inertia	(m ⁴)
E_{se}	Effective soil secant modulus of elasticity	(MPa)
K_R	Variable	Unitless
H_u	Ultimate pile head load	(kN)
F_ρ	Deflection yield factor	Unitless
F_ϕ	Rotation yield factor	Unitless
MI	Second moment of inertia of $k_h(x)$ about L_o	(m ⁴)
e	Distance from pile head to groundline	(m)

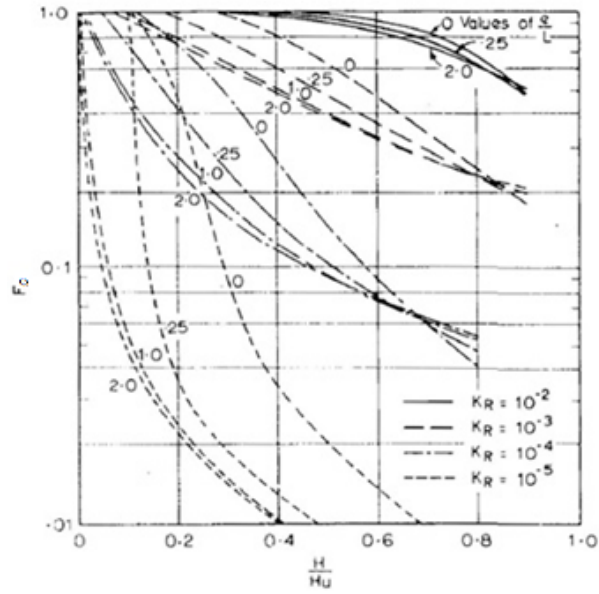


Figure I.1 Yield-Displacement factor, F_D , for Free Head Pile in Soil with Uniform E_s .
(Poulos and Davis, 1980)

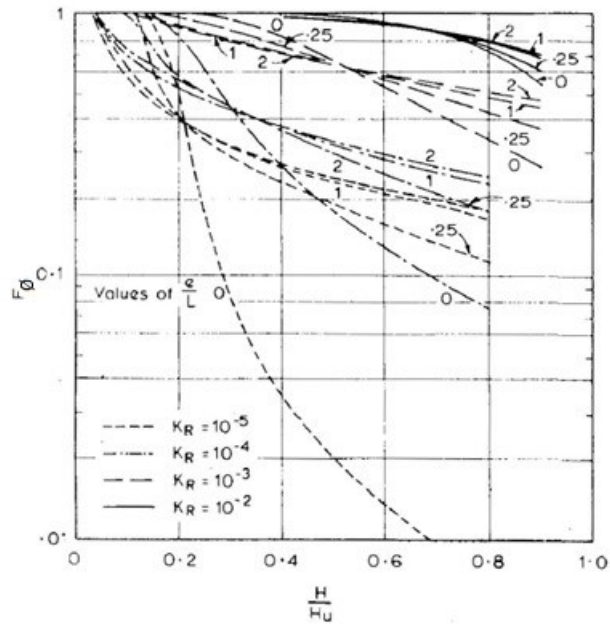


Figure I.2 Yield-Rotation factor, F_θ , for Free Head Pile in Soil with Uniform E_s .
(Poulos and Davis, 1980)

Table1: factors of the elastic response of piles solution by Poulos and Hull (1989).

Factor	$E_s = \text{constant}$	$E_s = mz$
K	E_p/E_s	E_p/mD
L_c/D	$2.09K^{0.25}$	$1.81K^{0.20}$
L_e	L_c if $L \geq L_c$, L if $L < L_c/3$	L_c if $L \geq L_c$, L if $L < L_c/3$
X	$\log_{10}\left(L_c/D\right)$	$\log_{10}\left(L_c/D\right)$
f_{yH}	$(L \geq L_c)$ $(0.976 + 2.196X)/E_s L$	$(13.10 + 11.09X)/mL_c^2$ $(3.18 + 9.70X)/mL^2$
$f_{yM} = f_{\theta H}$	$(L \geq L_c)$ $(5.52 + 9.08X)/E_s L_c^2$	$(34.63 + 11.09X)/mL_c^3$ $(2.41 + 12.71X)/mL^3$
$f_{\theta M}$	$(L \geq L_c)$ $(64.98 + 37.95X)/E_s L_c^3$	$(156.1 + 37.14X)/mL_c^4$ $(1.84 + 18.65X)/mL^3$
f_{yF}	$(L \geq L_c)$ $(1.336 + 1.64X)/E_s L_c$	$(5.67 + 4.14 \log_{10} X)/mL_c^2$ $(0.77 + 1.081X)/mL^2$
I_{MF}	$(L \geq L_c)$ $(L_c/D)(0.098 + 0.042X)$	$(L_c/D)(0.23 + 0.44 \log_{10} X)$ $(L/D)(0.76 - 0.35X)$

APPENDIX H - ABENDROTH AND GREIMANN CANTILEVER SOLUTION

Long Pile, Free Head, Cohesionless Soil -

Abendroth and Greimann (1987)

Critical Length	$L_c =$	$4(EI/k_h)^{0.25}$	6.18	m
	$E =$		205000	MPa
			205000000	kN/m ²
	$I =$		29300	cm ⁴
			0.000293	m ⁴
	$k_{he} =$		10538	kN/m ³
	$n_{h1} =$	0-3m	4400	kN/m ³
	$n_{h2} =$	3-5m	24000	kN/m ³
	$n_{h3} =$	5-9.3m	12000	kN/m ³
	$d =$		0.31	m
	$L_o =$	$L_c/2$	3.09	m
parallel axis theorem	actual 2nd mom inertia =		33439	m ⁴
	actual 2nd mom inertia =		101001	m ⁴
	rectangular 2nd mom inertia =		9.837	* k_{he}
	$k_{he} =$	actual 2nd MI/rect 2nd MI	10267	kN/m ³
	triangular 2nd mom inertia =		2.459	* k_{hmax}
	$k_{hmax} =$	rect 2nd MI/triang 2nd MI	41070	kN/m ³
	$E_{smax} =$		12732	kN/m ²
	$m =$		4120	kN/m ² /m
	$M_{pinned} =$	$D_1 EI \Delta / L_{Mpinned}^2$	367.0	kNm
	$V_{pinned} =$	$D_1 EI \Delta / L_{Vpinned}^3$	319.5	kN
	$M_{fixed} =$	$D_1 EI \Delta / L_{Mfixed}^2$	1062.9	kNm
	$V_{fixed} =$	$D_1 EI \Delta / L_{Vpinned}^3$	639.0	kN
	$D_1 \text{ fixed} =$		6	Unitless
	$D_1 \text{ free} =$		3	Unitless
	$\Delta =$		0.046	m
	$L_{Mpinned} =$		4.75	m

	$L_{Mfixed} =$	3.95 m
	$I_u =$	0.55 m
	$I_{eMpinned} =$	4.20 m
	$I_{eMfixed} =$	3.40 m
	$L_{vpinned} =$	2.96 m
	$L_{vfixed} =$	3.33 m
	$I_u =$	0.55 m
	$I_{eVpinned} =$	2.41 m
	$I_{eVfixed} =$	2.78 m
	$I_u/I_c =$	0.089 Unitless
From Fig 5.3 p. 94	$I_e/I_c =$	0.68 Unitless
From Fig 5.2 p. 94	$I_e/I_c =$	0.55 Unitless
From Fig 5.3 p. 94	$I_e/I_c =$	0.39 Unitless
From Fig 5.2 p. 94	$I_e/I_c =$	0.45 Unitless
Abendroth and Greimann (1987)		

Where

$L_c =$	Critical pile length	(m)
$d =$	Pile diameter	(m)
$n_{hi} =$	Variation of k_h with depth for soil layer i	(kN/m^3)
$L_o =$	Active pile length	(m)
$k_{he} =$	Effective k_h	(kN/m^3)
$k_{hmax} =$	Maximum k_h	(kN/m^3)
$E_{smax} =$	Maximum E_s	(kN/m^2)
$m =$	Variation of E_s with depth	(kN/m^3)
$E =$	Pile modulus of elasticity	(Mpa)
$I_e =$	Embedded pile length	(m)
Δ	Pile deflection at point of load application	(m)
$I =$	Pile moment of inertia	(m^4)
$M_{pinned} =$	Maximum pinned head pile moment	(kNm)
$V_{pinned} =$	Maximum pinned head pile shear	(kN)
$M_{fixed} =$	Maximum fixed head pile moment	(kNm)
	Maximum fixed head pile shear	(kN)
$V_{fixed} =$		
$D_1 =$	Constant	Unitless
$L_{Mpinned} =$	Pile length for pinned head moment	(m)

$L_{Mfixed} =$	Pile length for fixed head moment	(m)
$l_u =$	Unsupported pile length	(m)
$l_{eMpinned} =$	Embedded pile length for pinned head mom	(m)
$l_{eMfixed} =$	Embedded pile length for fixed head mom	(m)
$L_{Vpinned} =$	Pile length for pinned head shear	(m)
$L_{Vfixed} =$	Pile length for fixed head shear	(m)
$l_u =$	Unsupported pile length	(m)
$l_{eVpinned} =$	Embedded pile length for pinned head shear	(m)
$l_{eVfixed} =$	Embedded pile length for fixed head shear	(m)
$MI =$	Second moment of inertia of $k_h(x)$ about L_o	(m ⁴)

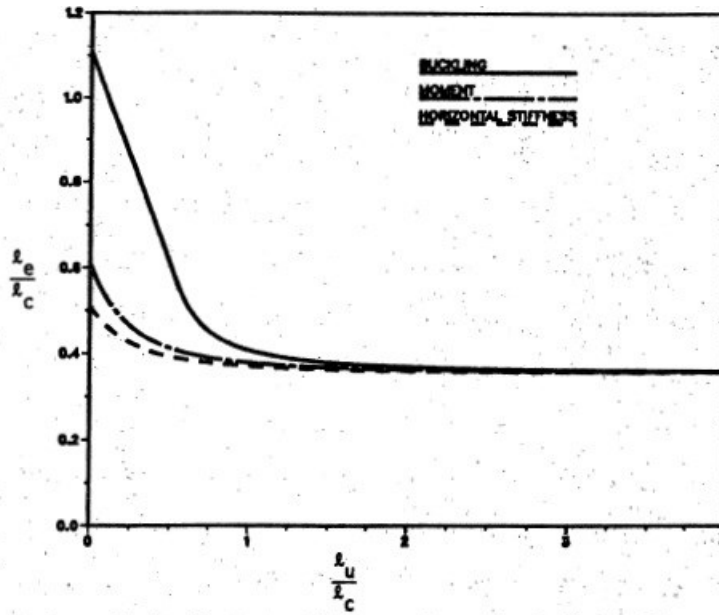


Figure 5.2. Equivalent cantilevers for fixed-head piles embedded in a uniform soil.

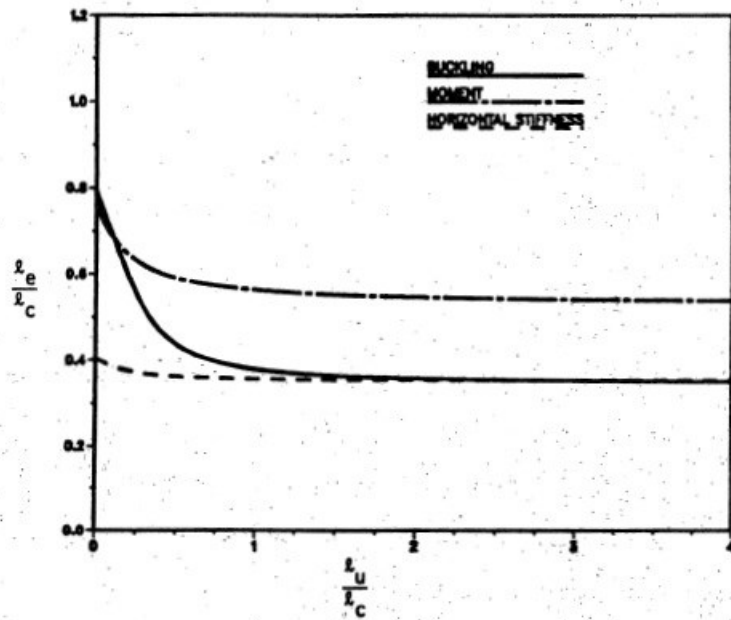


Figure 5.3. Equivalent cantilevers for pinned-head piles embedded in a uniform soil.

APPENDIX I - DEVELOPMENT OF NON-LINEAR SOIL SPRINGS

Head Deflection		2mm		Calculated	STAAD
Node	Reaction (kN/m)	Deflection (mm)	Deflection (m)	Stiffness (kN/m)	Stiffness (kN/m)
27	-17.983	0.817	0.000817	22011.016	22000
28	-14.77	0.224	0.000224	65937.5	66000
29	-0.217	0.002	0.000002	108500	110000
30	11.805	0.1	0.0001	118050	840000
31	1.343	-0.001	-0.000001	1343000	1080000
32	-0.651	0.001	0.000001	651000	660000
33	-0.173	0	0.0000001	780000	780000
34	0.032	0	0.0000000	900000	900000
35	0.017	0	0.0000000	1020000	1020000
36	0.1	0	0.0000001	1140000	1140000
37	-0.001	0	0.0000000	1217999.9	1218000

Head Deflection		10mm		Calculated	STAAD
Node	Reaction (kN/m)	Deflection (mm)	Deflection (m)	Stiffness (kN/m)	Stiffness (kN/m)
27	-26.238	4.771	0.004771	5499.476	5500
28	-36.396	2.206	0.002206	16498.64	16500
29	-1.904	0.692	0.000692	2751.4451	27500
30	-8.509	0.041	0.000041	207536.59	210000
31	23.72	-0.088	-0.000088	269545.45	270000
32	0.182	-0.00066	-6.6E-07	275757.58	165000
33	4.276	-0.022	-0.000022	194363.64	195000
34	0.056	0	0.0000001	560000	225000
35	-0.696	0.003	0.000003	232000	255000
36	-0.346	0.001	0.000001	346000	285000
37	0.055	0	0.0000001	550000	304500

Head Deflection		20mm		Calculated Stiffness (kN/m)	STAAD Stiffness (kN/m)
Node	Reaction (kN/m)	Deflection (mm)	Deflection (m)		
27	-33.303	10.092	0.010092	3299.941	3300
28	-48.969	4.946	0.004946	9900.728	9900
29	-27.353	1.658	0.001658	16497.59	16500
30	-16.953	0.135	0.000135	125577.8	126000
31	34.623	-0.214	-0.000214	161789.7	162000
32	14.816	-0.15	-0.00015	98773.33	99000
33	5.621	-0.048	-0.000048	117104.2	117000
34	0.078	-0.001	-0.000001	78000	135000
35	-1.144	0.007	0.000011	104000	153000
36	-0.707	0.004	0.000004	176750	171000
37	-0.01	0	0.000001	10000	182700

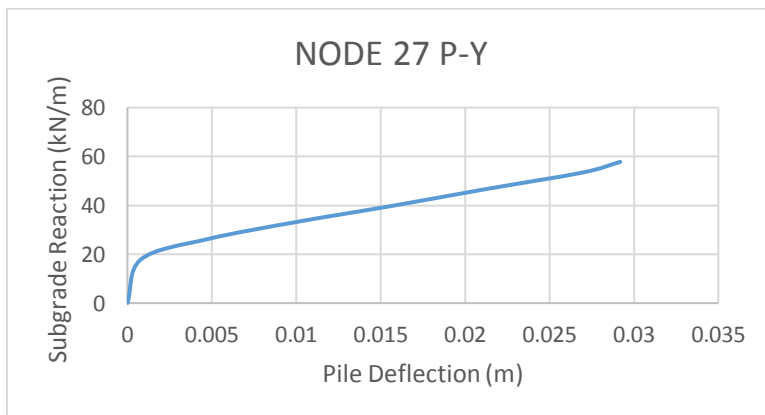
Head Deflection		30mm		Calculated Stiffness (kN/m)	STAAD Stiffness (kN/m)
Node	Reaction (kN/m)	Deflection (mm)	Deflection (m)		
27	-39.899	15.77	0.01577	2530.057	2530
28	-61.359	8.084	0.008084	7590.178	7590
29	-37.324	2.951	0.002951	12647.92	12650
30	-35.917	0.372	0.000372	96551.08	96600
31	43.578	-0.351	-0.000351	124153.8	124200
32	23.324	-0.307	-0.000307	75973.94	75900
33	11.418	-0.127	-0.000127	89905.51	89700
34	1.944	-0.019	-0.000019	102315.8	103500
35	-1.313	0.011	0.000013	101000	117300
36	-1.371	0.01	0.00001	137100	131100
37	-0.479	0.003	0.000003	159666.7	140070

Head Deflection		40mm		Calculated	STAAD
Node	Reaction (kN/m)	Deflection (mm)	Deflection (m)	Stiffness (kN/m)	Stiffness (kN/m)
27	-46.592	21.178	0.021178	2200.019	2200
28	-73.214	11.093	0.011093	6600.018	6600
29	-46.351	4.214	0.004214	10999.29	11000
30	-52.497	0.625	0.000625	83995.2	84000
31	51.12	-0.473	-0.000473	108076.1	108000
32	30.697	-0.465	-0.000465	66015.05	66000
33	16.748	-0.215	-0.000215	77897.67	78000
34	3.97	-0.044	-0.000044	90227.27	90000
35	-1.195	0.012	0.000012	99583.33	102000
36	-1.919	0.017	0.000017	112882.4	114000
37	-1.068	0.009	0.000009	118666.7	121800

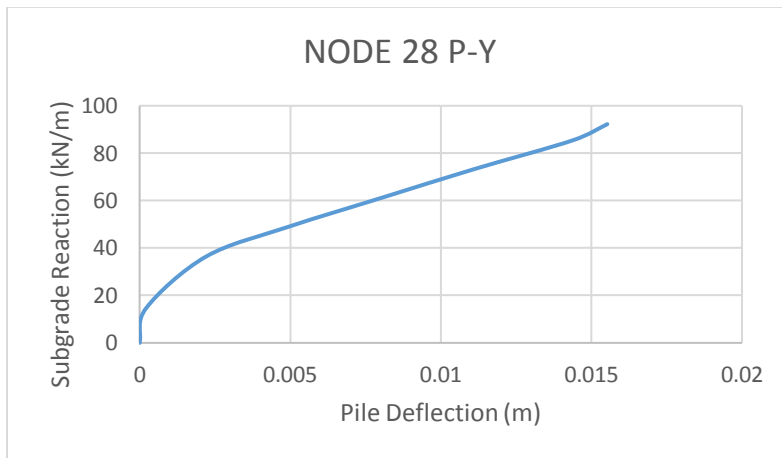
Head Deflection		50mm		Calculated	STAAD
Node	Reaction (kN/m)	Deflection (mm)	Deflection (m)	Stiffness (kN/m)	Stiffness (kN/m)
27	-53.532	27.037	0.027037	1979.953	1980
28	-85.428	14.382	0.014382	5939.925	5940
29	-55.633	5.62	0.00562	9899.11	9900
30	-69.952	0.925	0.000925	75623.78	75600
31	58.313	-0.6	-0.0006	97188.33	97200
32	38.229	-0.644	-0.000644	59361.8	59400
33	22.463	-0.32	-0.00032	70196.88	70200
34	6.366	-0.079	-0.000079	80582.28	81000
35	-0.865	0.009	0.000009	96111.11	91800
36	-2.453	0.024	0.000024	102208.3	102600
37	-1.807	0.016	0.000016	112937.5	109620

Head Deflection		54mm		Calculated	STAAD
Node	Reaction (kN/m)	Deflection (mm)	Deflection (m)	Stiffness (kN/m)	Stiffness (kN/m)
27	-57.799	29.191	0.029191	1980.028	1980
28	-92.237	15.528	0.015528	5940.044	5940
29	-60.067	6.067	0.006067	9900.61	9900
30	-75.527	0.999	0.000999	75602.6	75600
31	62.96	-0.648	-0.00065	97160.49	97200
32	41.276	-0.695	-0.0007	59389.93	59400
33	24.253	-0.345	-0.00035	70298.55	70200
34	6.873	-0.085	-8.5E-05	80858.82	81000
35	-0.934	0.01	0.00001	93400	91800
36	-2.649	0.026	0.000026	101884.6	102600
37	-1.951	0.018	0.000018	108388.9	109620

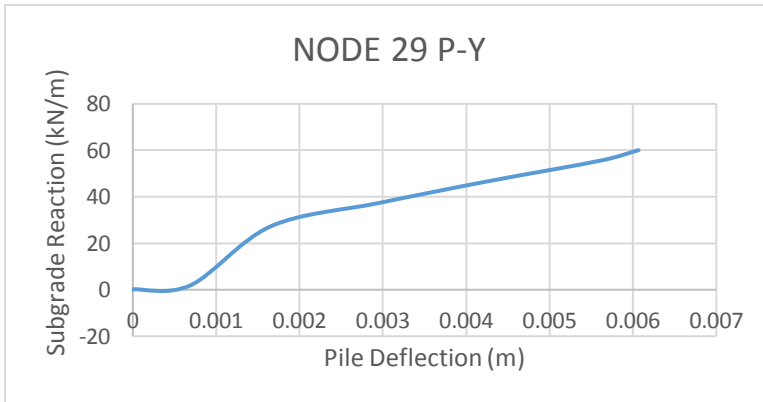
Node 27	P (kN)	y (m)	ΔP (kN)	Δy (m)	k (kN/m)
	0	0			
	17.983	0.000817	17.983	0.000817	22011.016
	26.238	0.004771	8.255	0.003954	2087.7592
	33.303	0.010092	7.065	0.005321	1327.7579
	39.899	0.01577	6.596	0.005678	1161.6766
	46.592	0.021178	6.693	0.005408	1237.6109
	53.532	0.027037	6.94	0.005859	1184.5025
	57.799	0.029191	4.267	0.002154	1980.9656



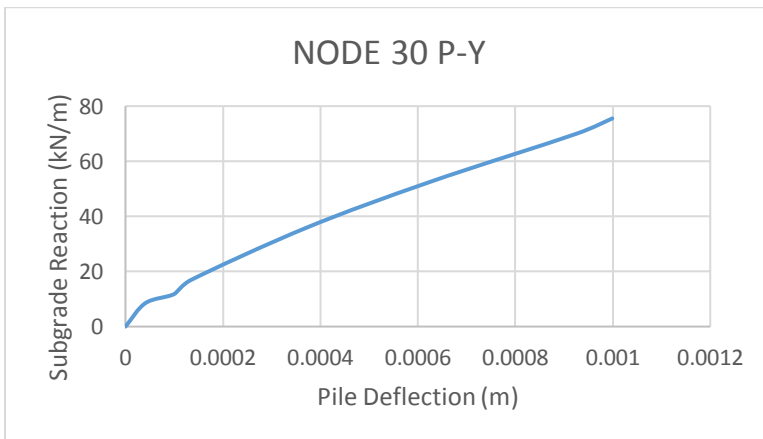
Node 28	P (kN)	y (m)	ΔP (kN)	Δy (m)	k (kN/m)
	0	0			
	14.77	0.000224	14.77	0.000224	65937.5
	36.396	0.002206	21.626	0.001982	10911.201
	48.969	0.004946	12.573	0.00274	4588.6861
	61.359	0.008084	12.39	0.003138	3948.3748
	73.214	0.011093	11.855	0.003009	3939.8471
	85.428	0.014382	12.214	0.003289	3713.5908
	92.237	0.015528	6.809	0.001146	5941.5358



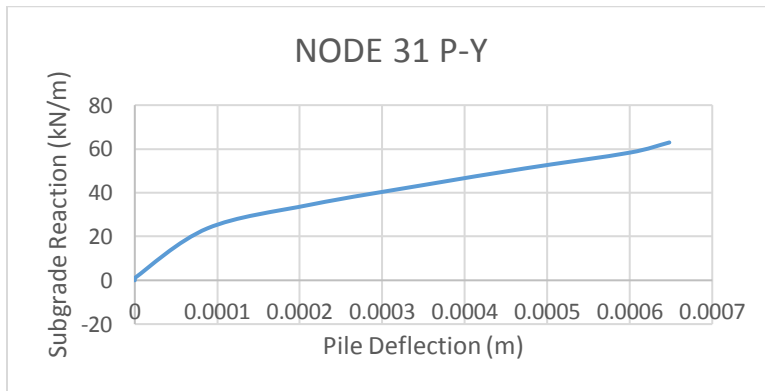
Node 29	P (kN)	y (m)	ΔP (kN)	Δy (m)	k (kN/m)
	0	0			
	0.217	0.000002	0.217	0.000002	108500
	1.904	0.000692	1.687	0.00069	2444.9275
	27.353	0.001658	25.449	0.000966	26344.72
	37.324	0.002951	9.971	0.001293	7711.5236
	46.351	0.004214	9.027	0.001263	7147.2684
	55.633	0.00562	9.282	0.001406	6601.707
	60.067	0.006067	4.434	0.000447	9919.4631



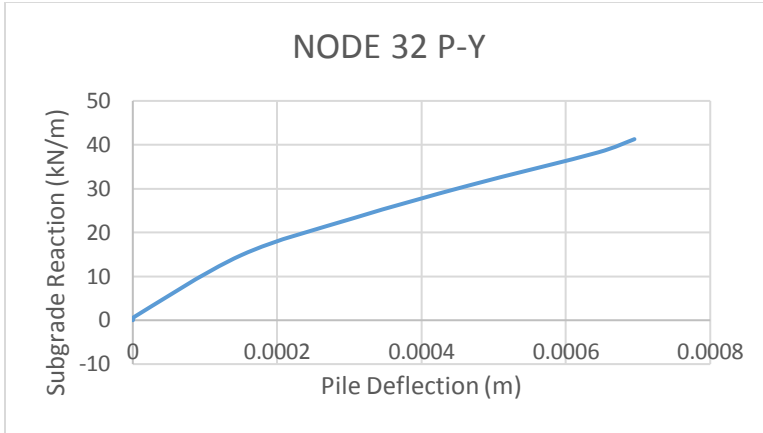
Node 30	P (kN)	y (m)	ΔP (kN)	Δy (m)	k (kN/m)
	0	0			
	8.509	0.000041	8.509	0.000041	207536.59
	11.805	0.0001	3.296	0.000059	55864.407
	16.953	0.000135	5.148	0.000035	147085.71
	35.917	0.000372	18.964	0.000237	80016.878
	52.497	0.000625	16.58	0.000253	65533.597
	69.952	0.000925	17.455	0.0003	58183.333
	75.527	0.000999	5.575	7.4E-05	75337.838



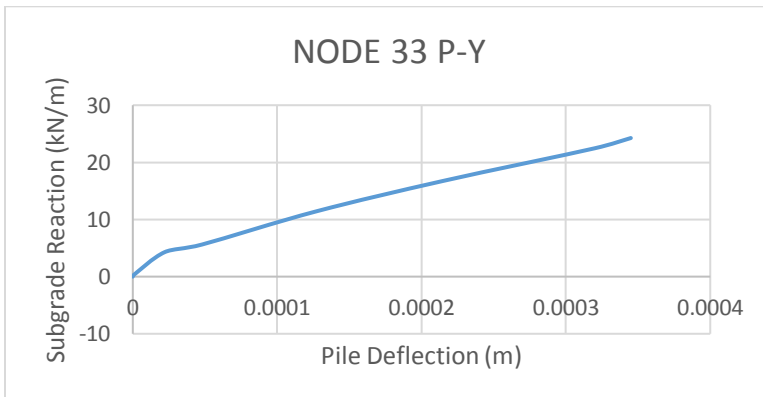
Node 31	P (kN)	y (m)	ΔP (kN)	Δy (m)	k (kN/m)
	0	0			
	1.343	0.000001	1.343	0.000001	1343000
	23.72	0.000088	22.377	0.000087	257206.9
	34.623	0.000214	10.903	0.000126	86531.746
	43.578	0.000351	8.955	0.000137	65364.964
	51.12	0.000473	7.542	0.000122	61819.672
	58.313	0.0006	7.193	0.000127	56637.795
	62.96	0.000648	4.647	4.8E-05	96812.5



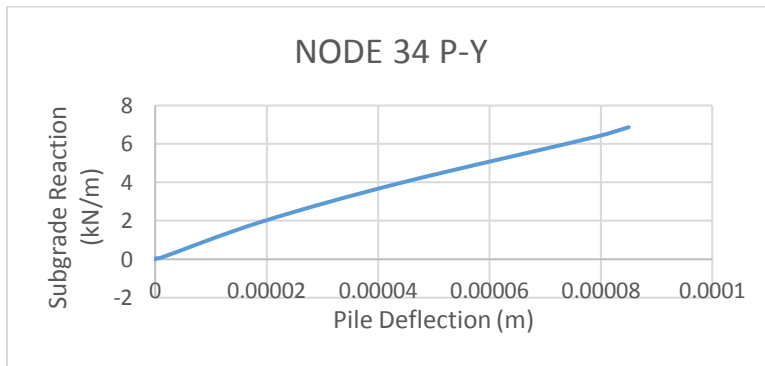
Node 32	P (kN)	y (m)	ΔP (kN)	Δy (m)	k (kN/m)
	0	0			
	0.182	0.000001	0.182	6.6E-07	275757.58
	0.651	0.000001	0.469	3.4E-07	1379411.8
	14.816	0.00015	14.165	0.0001493	94850.676
	23.324	0.000307	8.508	0.000157	54191.083
	30.697	0.000465	7.373	0.000158	46664.557
	38.229	0.000644	7.532	0.000179	42078.212
	41.276	0.000695	3.047	5.1E-05	59745.098



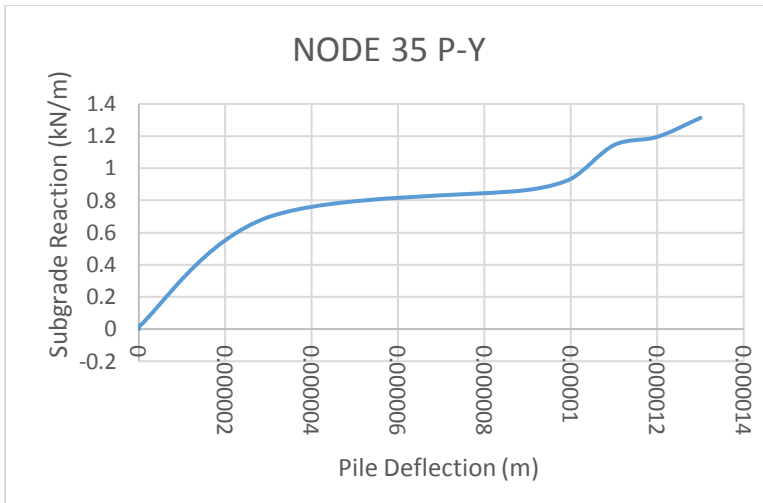
Node 33	P (kN)	y (m)	ΔP (kN)	Δy (m)	k (kN/m)
	0	0			
	0.173	0.0000001	0.173	0.0000001	1730000
	4.276	0.000022	4.103	0.000022	186500
	5.621	0.000048	1.345	0.000026	51730.769
	11.418	0.000127	5.797	0.000079	73379.747
	16.748	0.000215	5.33	0.000088	60568.182
	22.463	0.00032	5.715	0.000105	54428.571
	24.253	0.000345	1.79	0.000025	71600



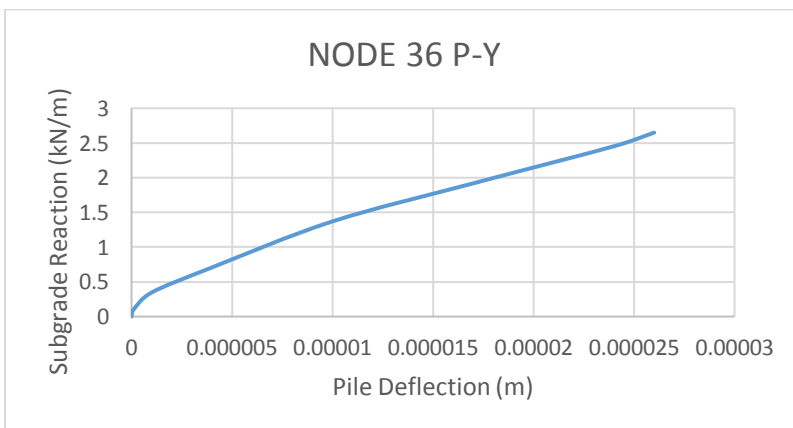
Node 34	P (kN)	y (m)	ΔP (kN)	Δy (m)	k (kN/m)
	0	0			
	0.032	0.00000001	0.032	1E-08	3200000
	0.056	0.00000001	0.024	9E-08	266666.67
	0.078	0.0000001	0.022	0.0000009	24444.444
	1.944	0.000019	1.866	0.000018	103666.67
	3.97	0.000044	2.026	0.000025	81040
	6.366	0.000079	2.396	0.000035	68457.143
	6.873	0.000085	0.507	6E-06	84500



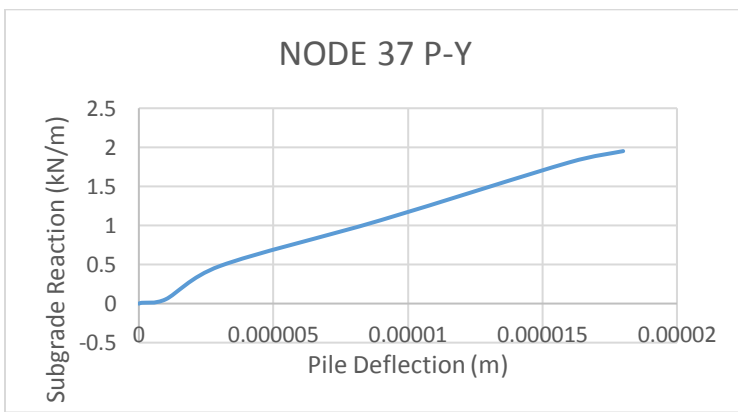
Node 35	P (kN)	y (m)	ΔP (kN)	Δy (m)	k (kN/m)
	0	0			
	0.017	0.00000001	0.017	1E-08	1700000
	0.696	0.000003	0.679	2.99E-06	227090.3
	0.865	0.000009	0.169	0.000006	28166.667
	0.934	0.00001	0.069	0.000001	69000
	1.144	0.000011	0.21	1E-06	210000
	1.195	0.000012	0.051	0.000001	51000
	1.313	0.000013	0.118	1E-06	118000



Node 36	P (kN)	y (m)	ΔP (kN)	Δy (m)	k (kN/m)
	0	0			
	0.1	0.0000001	0.1	0.0000001	1000000
	0.346	0.0000001	0.246	0.0000009	273333.33
	0.707	0.0000004	0.361	0.0000003	120333.33
	1.371	0.000001	0.664	0.0000006	110666.67
	1.919	0.0000017	0.548	0.0000007	78285.714
	2.453	0.000024	0.534	0.0000007	76285.714
	2.649	0.000026	0.196	0.0000002	98000



Node 37	P (kN)	y (m)	ΔP (kN)	Δy (m)	k (kN/m)
	0	0			
	0.001	0.00000001	0.001	1E-08	100000
	0.01	0.0000001	0.009	9E-08	100000
	0.055	0.000001	0.045	0.0000009	50000
	0.479	0.000003	0.424	0.000002	212000
	1.068	0.000009	0.589	0.000006	98166.667
	1.807	0.000016	0.739	0.000007	105571.43
	1.951	0.000018	0.144	0.000002	72000



APPENDIX J - STRAIN GAUGE CALIBRATION SHEETS

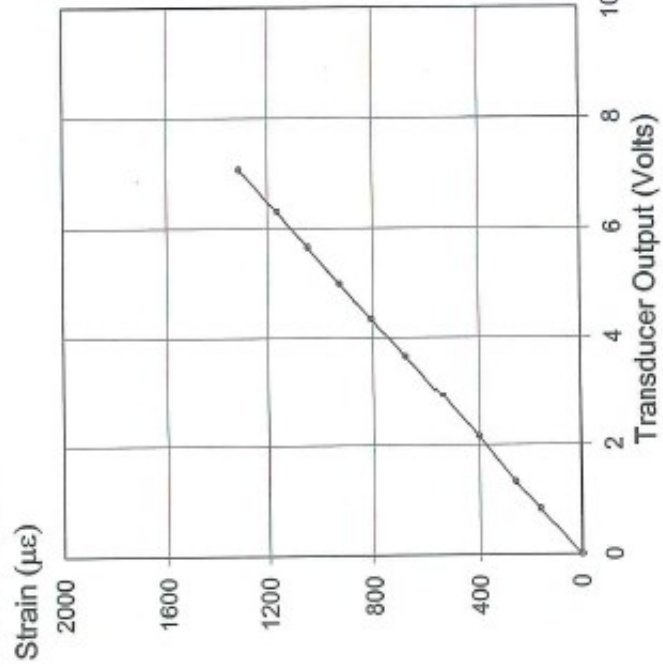


Pile Dynamics, Inc.

Transducer C556

PDA Cal Factor (5.0 V) 92.2µε/V

Applied Strain (µε)	Transducer Output (Volts)
0	0.00
164	0.84
259	1.31
402	2.16
543	2.92
677	3.65
806	4.33
926	4.98
1046	5.65
1167	6.30
1312	7.07



Shunt (60.4 KΩ) 2.5 V
 General Factor 320.1µε/mV/V

Calibrated by: 10-Apr-2009
 Calibrated on:

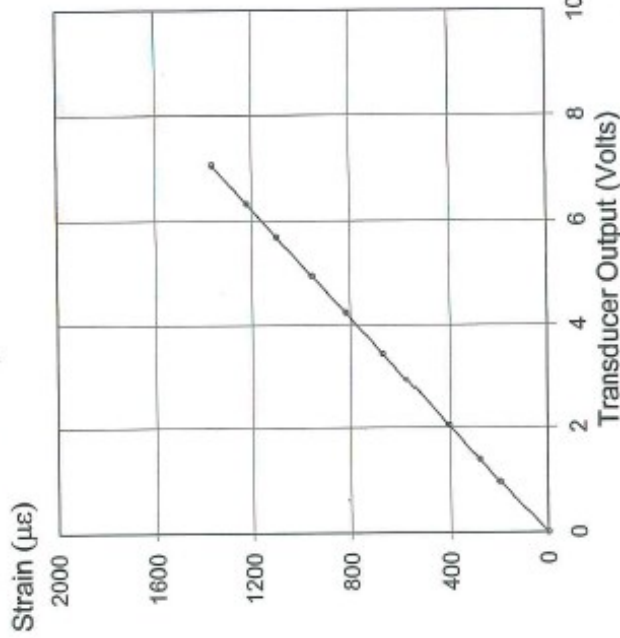
Traceable to N.I.S.T.
 Strain Transducer Calibrator System 2004 / revision 1.2



Pile Dynamics, Inc. Transducer C583

Pile Dynamics, Inc.

PDA Cal Factor (5.0 V) 96.0 $\mu\epsilon/V$



Applied Strain ($\mu\epsilon$)	Transducer Output (Volts)
0	0.00
199	0.95
280	1.38
407	2.04
571	2.93
668	3.44
820	4.23
956	4.94
1100	5.68
1222	6.32
1368	7.06

Shunt (60.4 K Ω) 2.5 V
General Factor 333.3 $\mu\epsilon/mV/V$

Traceable to N.I.S.T.

Calibrated by: 40-Apr-2009
Calibrated on:

Shah Transducer Calibrator System 2004 Version 1.2

